



Università degli Studi di Firenze
Dipartimento di Fisica
Dottorato di Ricerca in Fisica, XVI ciclo

Tesi di Dottorato

Atomic Fermi Gases in an Optical Lattice

Francesca Ferlino

Supervisore:
Prof. Massimo Inguscio

Coordinatore:
Prof. Alessandro Cuccoli

Contents

Introduction	3
1 Atomic Fermi gas	9
1.1 Outline	10
1.2 Trapped Fermi gas	11
1.2.1 Spatial and momentum distribution	13
1.2.2 Comparison with the Bose-Einstein condensate	14
1.3 The intriguing issue of cooling a Fermi gas	15
1.3.1 Experimental setup	17
1.3.2 Experimental procedure	20
1.4 Fermi-Bose mixture	26
1.4.1 Measurement of the interspecies scattering length	26
1.4.2 Mean field approach	30
1.4.3 Expansion of the Fermi gas	32
1.4.4 Collapse of the Fermi gas	35
1.4.5 On the route toward the BCS transition	39
2 Quantum gas in a periodic potential	41
2.1 A periodic potential for quantum gases	42
2.1.1 The optical lattice	42
2.2 One-Dimensional periodic potential	44
2.2.1 Useful definitions	44
2.2.2 Bloch theorem	45
2.2.3 Momentum eigenfunction and Wannier function	47
2.2.4 Energy band in one dimension	48
2.3 The Mathieu equation	50
2.4 Transport through the lattice	52
2.4.1 Semiclassical model and Bloch oscillation	53

2.4.2	Zener tunneling	56
2.4.3	Wannier-Stark states	57
3	Fermi gas in a vertical lattice	61
3.1	Outline	61
3.2	Production of an atomic Fermi gas in a vertical lattice	62
3.3	Bloch oscillations and Zener tunneling	64
3.3.1	Zener tunneling	66
3.4	Bloch oscillations of a Fermi gas	70
3.4.1	Bosons vs fermions: decoherence of Bloch oscillation	72
3.5	Interference between Wannier-Stark states	75
3.6	Atom interferometry with trapped Fermi gas	77
3.6.1	Scheme for an atom interferometer	78
3.6.2	Measurement of g	81
4	Localization in a combined periodic and harmonic potential	85
4.1	Outline	86
4.2	Periodic plus harmonic potential: A new problem	87
4.2.1	Localized vs delocalized states	89
4.2.2	Experimental setup	91
4.3	rf-Spectroscopy of localized states	92
4.3.1	Experimental technique	93
4.3.2	Localization and addressability	98
4.4	Insulating behavior of fermionic localized state	101
4.4.1	Semiclassical model	101
4.4.2	Center-of-mass dipolar oscillation	104
4.5	Delocalized states: Bose-Einstein condensate	107
5	Conduction of a Fermi gas in the combined potential	113
5.1	Outline	114
5.2	Transport of localized states assisted by collisions	114
5.2.1	Experimental procedure	114
5.2.2	Center-of-mass dipole oscillations	115
5.2.3	The Esaki and Tsu theory works here ?	117
5.2.4	Decay and localization	120
	Conclusions	121

A Calibration of the optical lattice

Introduction

Over the last decade, the field of quantum gas has been subjected to an exciting growth accompanied by a rapid increase of both experimental and theoretical research activities. This amazing development has been triggered by the first achievement of Bose-Einstein condensation in 1995¹. The firsts Bose-Einstein condensates have been first produced with a sample of ^{87}Rb [1], ^7Li [2], and ^{23}Na [3]. Further, other atomic species have been employed, such as ^1H [4], ^{85}Rb [5], metastable ^4He [6, 7], ^{41}K [8], ^{133}Cs [9] and ^{174}Yb [10]. Up to now, more than fifty groups worldwide are producing dilute-gas condensates, using different tricks and techniques. New prospects using other atomic species are also under examination [11, 12, 13]. This big interest is mainly due to the fact that a Bose-Einstein condensate (BEC) is a new state of matter characterized by a macroscopic occupation of a single quantum state. Indeed, when the de Broglie thermal-wavelength exceeds the mean spacing between atoms, 10^5 - 10^7 bosons arrange themselves in a single quantum state. This large occupation number together with the experimental ability to manipulate atomic gases opens the unique possibility to study, on a macroscopic scale, several quantum effects enclosing many branches of physics [14, 15, 16].

Nevertheless, the field of quantum gases is not exhausted here !

In 1999 another crucial goal has been reached with the first production of a degenerate Fermi gas of ^{40}K atoms [17]. Up to now, seven experimental groups have produced a Fermi gas well below the temperature of degeneracy exploiting evaporative cooling on two different spin-states of ^6Li [18, 19], or taking advantage from the sympathetic cooling technique using a ^6Li - ^7Li [20, 21], a ^6Li - ^{23}Na [22], and a ^{40}K - ^{87}Rb [23] mixture.

Fermions exhibit a somehow opposite quantum behavior with respect to bosons mainly due to their exchange properties. Indeed, indistinguishable particles are described by a many body wave-function which turns out to be symmetric under the exchange

¹The Nobel Prize in 2001 was awarded to Eric Cornell, Wolfgang Ketterle, and Carl Wieman for their work on BEC

of two bosonic particles and anti-symmetric for fermions. Furthermore, fermions attract much attention not only as natural antagonist of bosons but also for their peculiar characteristics. First of all, the anti-symmetry of fermionic particles leads to the well-known Pauli exclusion principle which introduces in the system a sort of interparticle repulsion. Indeed, fermions have to occupy one-by-one the quantum states and the multiple-occupation of one state is forbidden. In the energy space, the fermions are arranged in the so-called Fermi sphere whose radius, at $T = 0$, is fixed by the highest energy level reachable (Fermi energy). For instance, a white dwarf and neutron stars are mainly composed of fermions and the existence of a Fermi sphere with blocked dimension yields to a "quantum pressure" which stabilizes the stars against the collapse enhanced by strong gravitational forces.

In despite of the above discussion, fermions and bosons do not belong in two completely separate classes of particles. The link between them is quite subtle and lies in the possibility to produce a bosonic-like particle starting from two distinguishable fermions. This is the basic idea of the BCS theory of the superconductivity: two distinguishable electrons near the surface of the Fermi sphere are unstable against an attractive perturbation and can form a pair, the so-called Cooper pair. It look like quite natural to export the idea of Cooper pairs also to atomic Fermi gases. Recently many efforts have been focused in this direction. First of all, distinguishable fermions can be obtained from a mixture of fermions in two-spin states. Further, one can produce an interaction between particles by tuning the interstate scattering length via Feshbach resonances [24]. In the limit of strong repulsive interaction, the system is unstable with respect to the formation of molecules which can be eventually Bose condensed (BEC regime) [25, 26, 27, 28]. In presence of a strong attractive interaction, fermions could instead form Cooper pairs and the system behaves as an high T_C superconductor (BCS regime). Many experiments have been performed in the BCS-BEC crossover [29, 30, 31, 32, 33], and, until now, a clear and indisputable evidence of the achievement of the BCS regime has not yet been provided even if recent studies on collective excitations seem to indicate the accomplishment of this regime [34, 35]. Another promising scheme to achieve the BCS regime is to use a Fermi-Bose mixture in which bosons induce an effective attraction between the two fermionic spin states [36, 37]. Note that this method is the atomic analog of phonon-induced interaction which is the underlying mechanism of superconductivity.

The other *hot topic* of the quantum gases field concerns optical lattices. An optical lattice is a perfect periodic potential produced by a retroflected laser beam in a standing-wave configuration. In the last years, this periodic potential has been ex-

tensively exploited with Bose-Einstein condensates giving rise to spectacular effects at the border between different areas of physics. Experiments have explored effects of quantum phase coherence by observing, for instance, a macroscopic tunneling of condensed atoms through the lattice [38, 39, 40, 41] or a coherent emission of matter wave from a condensate loaded in a vertical lattice [42]. Furthermore, this system has also allowed the observation of phenomena ranging from the solid state physics, such as Bloch oscillations [43, 44], to the physics of high correlated system, with the evidence of a quantum phase transition from a superfluid to a Mott insulator [45], and to the field of gases of reduced dimensionality [46, 47].

In our experimental work, we have the unique possibility to combine together the Fermi gas and the optical lattice. Up to now, we are indeed the only experimental group producing such kind of system [48], and, as far as we know, several groups are now moving in this direction². The interest to bind together the field of Fermi gases with that of optical lattices is excited by different reasons. First of all, the tight resemblance between atomic fermions in an optical lattice and electrons in a ions lattice pushes toward the extension of solid state effects to atomic Fermi gases. Moreover, a Fermi gas in an optical lattice is a *perfect system* completely free from interactions. This feature opens the unique possibility to study single-particle coherence effects which are usually overwhelm by interaction [49, 50]. Indeed, in a spin-polarized Fermi gas interatomic collisions are suppressed by the Pauli principle and, a lattice, produced by laser light, is perfect in the sense that impurities or phononic excitations are absent. This ideal system turns out to be the most appropriate system to test the theory of transport in crystal in regimes not accessible neither in solids nor in bosonic gases [51]. Secondly, if a non-uniform extra potential is added to a Fermi gas in the lattice then is possible to detect phenomena of localization [52] which provides promising application in quantum computation devices [53]. Another potentiality of this system has been pointed out recently by several theoretical works: two-component Fermi gases or Fermi-Bose mixtures in a lattice exhibit a peculiar *exotic* phase diagram as a function of the interaction [54, 144, 145]. In addition, a tight 2D-lattice can also be exploited to investigate the physics of Mott-transition in a Fermi gas.

Finally, the optical lattice has recently been proposed as a tool to probe the fermionic superfluidity in a strong interacting two-components Fermi gas [57]. The detection of the BCS regime is indeed an open question whose resolution is of crucial importance.

²As far as we know, the group of Tilman Esslinger in Zurich and the one of Klaus Sengstock in Hamburg are now starting to work on Fermi gases in optical lattices.

The purpose of our experimental work, presented in this thesis, is to provide a testing ground for the basic behavior of a Fermi gas in an optical lattice. In this sense, our study on a non-interacting Fermi gas locates as the first step on the route towards a superfluid fermionic gas in an optical lattice.

Outline of the Thesis

This thesis report on our experimental investigation on a non-interacting Fermi gas in presence of an optical lattice. We find that the statistical distribution makes the properties of such system highly non trivial also in the limit of zero temperature. Indeed, on the one hand we will exploit the non-interaction of the system to observe phenomena of single-particle coherence, such as Bloch oscillation, on a long time scale, and on the other hand we use the broad energy distribution³ of fermions to study localization effects in presence of an additional non-uniform potential. We also study the transport of fermions from the non-interacting limit to the interacting one, exploring regimes not accessible in solid state.

Our work of this thesis is organized as follow:

The first Chapter is devoted to the description of our experimental setup. In particular, we produce a Fermi gas of ^{40}K atoms by using the technique of sympathetic cooling with ^{87}Rb bosonic atoms. The presence of the Bose gas, which can eventually condense, gives us a twofold possibility: we can whether study interaction effects between the two species or obtain a direct comparison between a Fermi and a Bose gas. We also report on some effects exhibited by our strong interacting Fermi-Bose mixture, such as the modification of the expansion and the collapse of the Fermi gas. In Chapter 2, we give a brief overview on the theory of a particle in a periodic potential, with particular attention to the transport properties. The third Chapter is devoted to the study of our Fermi gas trapped in a vertical lattice against the gravity. The force of gravity induces a motion of fermions resulting in a Bloch oscillation and/or in a Zener tunneling. Due to the non-interacting nature of the system, our measurements provide the first experimental observation of long-lived Bloch oscillations which are usually *killed* by interactions in common metals, or in semiconductors, or in Bose gases. Thanks to this peculiarity, we employ such oscillation to perform a time-resolved interferometric measurement of the force of gravity. We also discuss the superiority of fermions with respect to bosons in such kind of experiment. In Chap-

³We remind to the reader that the Fermi distribution is broad due to the Pauli principle which impose a single-occupation of energy levels.

ter 4, we address to the problem of a Fermi gas loaded in a combined parabolic and periodic potential. We observe that the parabolic potential destroys the translational invariance of the system leading to two different classes of states, named delocalized and localized states. In particular, delocalized fermions are the equivalent of Bloch particles whose dynamical evolution can be described in the framework of an effective mass theory. Localized fermions are instead related to Wannier-Stark states and behave as an insulator under an external driven potential. In Chapter 5, we show how the introduction of a collisional channel induces a transport on localized fermions. The interactions are introduced in the system by adding bosons. We then compare our findings with the Esaki and Tsu theory which usually applies for semiconductor superlattices.

Chapter 1

Atomic Fermi gas

Dove c'è sfizio non c'è perdenza...

A. B.

Over last decade, fundamental goal has been reached in the field of atomic physics. Above all, the achievement of Bose-Einstein condensation in neutral atoms [1, 2, 3, 4, 5, 6, 7, 8, 9, 10] has opened the exciting possibility to investigate quantum behavior on macroscopic scale. A Bose-Einstein condensate (BEC) is a new state of matter in which 10^5 - 10^7 particles, below a critical temperature, go to occupy the same quantum state. This "effective" attraction between bosons is a direct consequence of their statistic and it turns out that all the particles can be described by a single macroscopic wave-function. However in nature particles divide in two different classes and the natural *antagonists* of bosons are known as fermions. In 1999 another crucial goal has been reached with the production of a degenerate Fermi gas of ^{40}K atoms [17, 18, 20, 21, 22, 23]. This experimental result has attracted much attention in the community since fermions, near degeneracy, behave in a somehow opposite way with respect to bosons. First of all, while a phase transition separates the degenerate and the classical regime for a Bose gas, a system of identical fermions undergoes a smooth crossover between these two regimes. Secondly, Fermi particles experience an effective repulsion due to their statistics which obliges a single occupation of nearest neighbor quantum states.

In this Chapter we will show some of the fascinating consequences arising from the statistical nature of the Fermi gas.

1.1 Outline

The aim of this Chapter is to discuss the main features of a non-interacting trapped Fermi gas and to show how the behavior of the system is modified by the addition of a collisional channel. Indeed we can produce a Fermi-Bose mixture which exhibits a strong interspecies attraction leading to spectacular effects, such as the collapse of the Fermi gas.

We start to remind the properties of a trapped non-interacting Fermi gas (Sec. 1.2). We then describe our experimental procedure to produce a degenerate Fermi gas of ^{40}K atoms (Sec. 1.3). In particular, our procedure to bring fermions into degeneracy exploits the technique of sympathetic cooling in which a bosonic gas of ^{87}Rb atoms acts as a refrigerator. Our ^{40}K - ^{87}Rb Fermi-Bose mixture is an extremely rich system which gives us a twofold possibility: on the one hand, we can directly compare the behavior of atomic gases obeying to two different quantum statistics and, on the other hand, we can investigate interspecies interaction effects (Sec. 1.4). In particular, our Fermi-Bose mixture exhibits a large interspecies attraction which strongly affects both the density distribution and the dynamics of the system.

The main results reported in this Chapter on the Fermi-Bose mixture can be found in our recent publications:

- *Expansion of a Fermi gas interacting with a Bose-Einstein condensate*, F. Ferlaino, E. de Mirandes, G. Roati, G. Modugno, and M. Inguscio, Phys. Rev. Lett. **92**, 140405 (2004).
- *Magnetic Control of the Interaction in Ultracold K-Rb Mixtures* A. Simoni, F. Ferlaino, G. Roati, G. Modugno, and M. Inguscio, Phys. Rev. Lett. **90**, 163202 (2003).
- *Mean-field analysis of the stability of a K-Rb Fermi-Bose mixture*, M. Modugno, F. Ferlaino, F. Riboli, G. Roati, G. Modugno, and M. Inguscio, Phys. Rev. A **68**, 043626 (2003).
- *Collapse of a degenerate Fermi gas*, G. Modugno, G. Roati, F. Riboli, F. Ferlaino, R. Brecha, and M. Inguscio, Science **297**, 2240 (2002).
- *Dipolar oscillations in a quantum degenerate Fermi-Bose atomic mixture*, F. Ferlaino, R. Brecha, P. Hannaford, F. Riboli, G. Roati, G. Modugno, and M. Inguscio, J. Opt. B: Quantum Semiclass. Opt. **5**, S3 (2003).

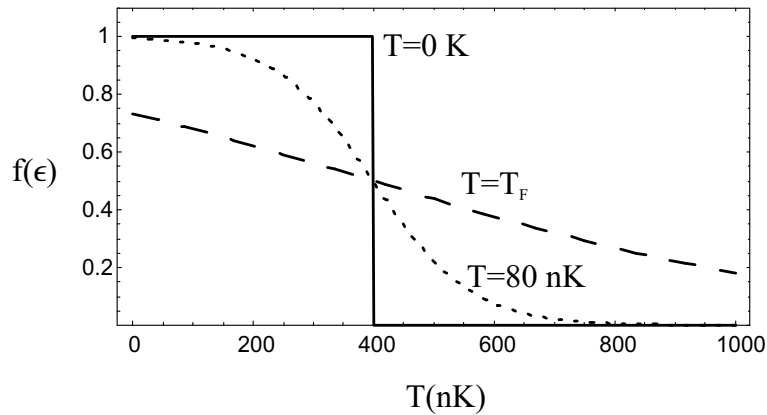


Figure 1.1: Fermi distribution $f(\epsilon)$ for different temperatures of the system: $T = 0K$ (solid line), $T = T_F$ (dashed line) and $T = 80nK$ (dotted line). The energy ϵ is expressed in units of $1/k_B$.

1.2 Trapped Fermi gas

While the bosonic degeneracy involves the formation of a Bose-Einstein condensate, the fermionic degeneracy leads to a single occupation of quantum states. At zero temperature, the occupation number of each fermionic quantum state is equal to one up to energies close to the Fermi energy E_F , and is zero for larger energies. The Fermi energy E_F corresponds to the higher energy level occupied at $T = 0K$, and sets the relevant energy scale of the system. This tight packing creates a Fermi sea of particles where a minimum size is maintained by the so-called Fermi pressure. Furthermore, additional particles can not penetrate into the Fermi sea and this gives rise to the Pauli blocking of collisions. It is interesting to note that all these features arise somehow from the properties of symmetry of the fermionic wave-function. In particular, a system composed by N identical fermions is described by a wave-function which is antisymmetric under the interchange of any pair of particle coordinates. On the contrary, a bosonic function is completely symmetric. This fundamental difference leads to different statistical mechanics which govern these two classes of particles. A Fermi gas obeys to the well-known Fermi-Dirac distribution

$$f(\mathbf{r}, \mathbf{p}) = \frac{1}{e^{\beta[H(\mathbf{r}, \mathbf{p}) - \mu]} + 1}, \quad (1.1)$$

where β is $1/k_B T$ with k_B the Boltzmann constant. The function $f(\mathbf{r}, \mathbf{p})$ is the occupation probability of a state of energy ϵ , where $H(\mathbf{r}, \mathbf{p})\psi(\mathbf{r}, \mathbf{p}) = \epsilon\psi(\mathbf{r}, \mathbf{p})$. The chemical potential μ fixes the atom number in the gas. Equation (1.1) includes the Pauli principle which forbids the multiple occupation of a single energy level. As

shown in Fig. 1.1, the zero-temperature Fermi distribution (1.1) is equal to one for energies lower than $E_F = \mu(T = 0K, N)$, and zero otherwise. The presence of a finite temperature smooths the step-wise transition from one to zero occupation numbers. In particular, a finite temperature a shell of amplitude $k_B T$ opens around E_F , and the unitary occupation is no more guaranteed. For such a distribution, only fermions with energies in a shell near the Fermi surface provide a response of the system to external perturbations. Thus, the ratio between the temperature T and the Fermi temperature, $T_F = E_F/k_B$, defines the degree of degeneration of our system. Note that the scenario is opposite in a Bose-condensed system where all the particles participate in the response [14].

We produce experimentally a Fermi gas which is confined by a harmonic trap with a cylindrical symmetry. The main quantities involved, such as temperature and atom number, depend also on the trapping potential. We now briefly remember to the reader the basic features of a harmonically trapped Fermi gas. A more detailed description can be found in [58, 59].

The Hamiltonian $H(\mathbf{r}, \mathbf{p})$ of a harmonically trapped Fermi gas is

$$H(\mathbf{r}, \mathbf{p}) = \frac{\mathbf{p}^2}{2m} + V_F(\mathbf{r}), \quad (1.2)$$

where m is the atomic mass of the fermion and $V_F(\mathbf{r})$ is the harmonic trap. Our harmonic potential exhibits a cylindrical symmetry along the z -axis, also named axial direction. The trapping frequencies are $(\omega_1, \omega_2, \omega_3) \equiv (\omega_r, \omega_r, \omega_z)$ with $\omega_{r,z}$ the radial and axial frequency, respectively. We introduce the aspect ratio of our trap $\lambda = \omega_z/\omega_r$ and V_F is given by

$$V_F(\mathbf{r}) = \frac{1}{2}m\omega_r^2(x^2 + y^2 + \lambda z^2). \quad (1.3)$$

The single particle levels are the familiar eigenvalues of the harmonic oscillator: $\epsilon_{n_x, n_y, n_z} = \hbar\omega_r(n_x + n_y + \lambda n_z)$ with n_x, n_y, n_z non-negative integers. If the thermal energy far exceeds the level spacing ($k_B T \gg \hbar\omega_r$), we can replace the discrete single-particle harmonic spectrum with a continuum one, whose density of energy states is

$$g(\epsilon) = \frac{\epsilon^2}{2\lambda(\hbar\omega_r)^3}. \quad (1.4)$$

The chemical potential μ is then given by the normalization condition for the total number of fermions N_F in the trap

$$N_F = \frac{1}{(2\pi\hbar)^3} \int \frac{g(\epsilon)d\epsilon}{e^{\beta(\epsilon-\mu)} + 1}. \quad (1.5)$$

Eq. (1.5) also fixes the Fermi energy E_F of the system [58]. Solving the integral, one indeed finds

$$E_F = \hbar\omega_r[6\lambda N_F]^{1/3}, \quad (1.6)$$

which sets the relevant energy scale of the system. From the Fermi energy we can define the typical size of a trapped degenerate gas

$$E_F = \frac{1}{2}m\omega_r^2 R_F^2 \rightarrow R_F = \sqrt{\frac{2E_F}{m\omega_r^2}} = a_{ho}(48N_F)^{1/6}, \quad (1.7)$$

where the harmonic oscillator length is $a_{ho} = \sqrt{\hbar/m\omega_{ho}}$ and $\omega_{ho} = (\omega_r^2\omega_z)^{1/3}$. From Eq. (1.7) follows that if the number of fermions $N_F \gg 1$, the size of the trapped Fermi cloud is much greater than a_{ho} : this is a consequence of the statistical "repulsion" imposed by the Pauli exclusion principle. This effective repulsion between fermions in the trap is known as Fermi pressure, and leads to a bigger size of the cloud with respect to the harmonic oscillator length a_{ho} . This is another important difference with respect to both a "classical" gas and a Bose condensed gas. Indeed decreasing the temperature, the size of a classical gas continuously shrinks accordingly to the classical Boltzmann distribution. The size of a non-interacting Bose-Einstein condensate is instead temperature-independent and at $T = 0$ K it is exactly equal to a_{r0} because they all occupy the lowest state of the harmonic oscillator. If one also introduces the two-body repulsive interaction between condensed atoms, the radius of the cloud also increases with N_B . In particular, the radius of the condensate R_B scales with N_B as $N^{1/5}$ which is slightly different from the behavior found for a Fermi gas, $R_F \propto N_F^{1/6}$ [58]. Despite to a similar dependence on the atom number, the dependence of $R_{B,F}$ from $N_{B,F}$ has a very different physical origin.

1.2.1 Spatial and momentum distribution

For a temperature different from zero, the density distribution of a degenerate Fermi gas has to be calculated numerically by integrating the distribution function (1.1) in the momentum space. At $T = 0$ K, one instead finds an analytic expression:

$$n(\mathbf{r}, T = 0) = \frac{8\lambda N}{\pi^2 R_F^3} \left[1 - \frac{\rho^2}{R_F^2} \right]^{3/2}, \quad (1.8)$$

where ρ is the effective distance $\rho = (x^2 + y^2 + \lambda^2 z^2)^{1/2}$ defined for a harmonic trap with a cylindrical symmetry. Another important quantity for our proposal is the momentum distribution of the cloud. Indeed, in the experiments, most of the information about the sample are obtained looking to the absorption signal of the

cloud, after the sudden release from the trap (see Sec. 1.3.2). When the confinement is switched off, the cloud performs a rapid and adiabatic expansion and we are able to measure the velocity distribution by imaging the atoms. The momentum distribution (Thomas-Fermi distribution) at zero temperature is

$$n(\mathbf{p}, T = 0) = \frac{1}{(2\pi)^3} \int d^3\mathbf{r} \Theta(p_F(\mathbf{r}) - p), \quad (1.9)$$

where $\Theta(p_F(\mathbf{r}) - p)$ is the unit step function and the Fermi momentum $p_F = \sqrt{2mE_F}$. The integral (1.9) gives [58]

$$n(\mathbf{p}, T = 0) = \frac{8N}{\pi^2 p_F^3} \left[1 - \frac{p^2}{p_F^2} \right]^{3/2}. \quad (1.10)$$

Despite the spatial anisotropy of the trap, the momentum distribution of the degenerate Fermi gas is isotropic i.e. the momentum distribution depends only on the magnitude of \mathbf{p} . As we will discuss in the next section, this is an important difference with respect to the case of a Bose gas.

1.2.2 Comparison with the Bose-Einstein condensate

A Bose gas shows a behavior somehow opposite with respect to the one exhibited by fermions. The difference between these two systems arises entirely from their different statistical nature. For lack of space, we will report just a brief discussion on some characteristic features of the Bose gas which immediately clarifies the difference between the two gases. Above all, trapped bosons undergo a phase transition as the critical temperature T_c is reached and all the atoms prefer to occupy macroscopically a single state. Furthermore, differently from a gas of identical fermions, the condensed bosons collide each other. Due to the low temperatures ($T \leq T_c \approx 100$ nK) and the diluteness of the cloud, the interparticle interaction can be described in a simple way. Indeed one can consider that each boson experiences a mean field potential produced by all the other particles on the gas [14, 15]. This approximation is somehow justified by the fact that, at low temperature, just two-body collisions survive. The interatomic potential can be written as a δ -function using the method of the pseudo-potentials,

$$V(\mathbf{r}' - \mathbf{r}) = g\delta(\mathbf{r}' - \mathbf{r}). \quad (1.11)$$

The coupling constant g , at the first order of the perturbation, takes the form

$$g_B = \frac{4\pi\hbar^2 a_B}{m}, \quad (1.12)$$

where a_B is the boson-boson s -wave scattering length. We just mention here that this interaction introduces in the system a sort of *rigidity* which yields to the spectacular phenomena of superfluidity observed in Bose-Einstein condensate [14].

For a large atom number N_B , the interaction energy is notably larger than the kinetic energy. In this limit, one can neglect the latter contribution to the energy and the system is known to be in the Thomas-Fermi regime. At $T = 0$ K, the density distribution of a trapped condensate has an inverted-parabola shape

$$n_B(\mathbf{r}) = \frac{R_B^2}{2g} \left[1 - \frac{\rho^2}{R_B^2} \right], \quad (1.13)$$

where R_B is the maximum radius of the cloud

$$R_B = \left(\frac{15\lambda g N_B}{4\pi} \right)^{1/5}. \quad (1.14)$$

The typical energy scale of a Bose gas is the zero-temperature chemical potential μ which scales with the atom number more rapidly than the Fermi energy ($\mu \propto N_B^{2/5}$ while $E_F \propto N_F^{1/3}$). Another important difference is connected to the spatial and momentum distribution of the two clouds. Even if the two gases exhibit a similar spatial distribution, their momentum distributions differ in a profound way. The momentum distribution of both a thermal cloud and a Fermi gas turns out to be isotropic. On the contrary, in a condensate, $n_B(\mathbf{p})$ is anisotropic in a asymmetric trap due to the non-linearity of the interparticle interaction ¹. Furthermore, the widths of the momentum distribution scale in the opposite way: p_F increases with N_F , while the typical momentum for a condensed atom decrease with particle number, since $p_B \sim 1/R_B$ due to the Heisenberg uncertainty principle.

1.3 The intriguing issue of cooling a Fermi gas

We experimentally produce a Fermi gas of ^{40}K atoms well below T_F using the technique of sympathetic cooling with ^{87}Rb atoms [23].

In this section, we give a rapid overview on the experimental technique used to produce our atomic Fermi gas. The reader can find a more detailed description in the PhD thesis of Giacomo Roati [59].

Since the first achievement of Bose-Einstein condensation, the standard technique to cool an atomic gas below the temperature of degeneracy consists of a pre-cooling

¹As we will show in Sec.1.4.2, the different momentum distribution of the two clouds leads also to a completely different expansion evolution.

phase based on laser cooling which carries the system at $T \approx 100 \mu\text{K}$ and of an evaporative cooling phase [60]. The initial cooling phase for both alkali bosons and fermions proceeds via laser cooling and magneto-optical trapping (MOT). The subsequent cooling phase has instead to be different for the two species. Bosons can indeed exploit techniques based on re-thermalization, while fermions can not collide down to μK [61]. In particular, bosons are transferred from the MOT into a magnetic trap, where a forced evaporative cooling is applied to bring the gas into degeneracy. The evaporation of bosons is performed usually by using a radio-frequency signal which remove selectively the hottest atoms from the trap. The key requirement for the usefulness of this technique is clearly the existence of a large elastic collisional rate between atoms which allows for an efficient thermalization of the gas. In general, the elastic cross-section depends on the temperature. At very low temperature, the only significant contribution to the collisional rate is given by the s-wave scattering amplitude which is temperature-independent. The other contributes (p-wave, d-wave, ecc...) are proportional to the temperature and thus suppressed down to $100 \mu\text{K}$.

The situation is even more complicated for identical fermions because interatomic collisions are completely suppressed in such a system. As a consequence, the evaporative cooling fails for spin-polarized fermions and another cooling procedure have to be found. One can circumvent this problem using some form of mutual or sympathetic cooling between two types of distinguishable particles, either two spin states of the same atomic species or of two kind of atoms. In the first scheme, fermions are simultaneously trapped in two different spin states and evaporative cooling is then performed on both components [17, 21]. Thermalization is now assured by s-wave collisions between these two spin states². The other scheme exploits the idea of to mix fermions with a gas of bosons which can be efficiently cooled using the usual evaporative cooling. The Fermi gas decrease its temperature by colliding with bosons which act like a refrigerator. This latter technique is known as *sympathetic cooling* and has been carried out with success at ENS (Paris) [20], at Rice (Texas) [18], at MIT [22], and in our experiment [23].

In our experiment, we indeed adopt the sympathetic cooling scheme mixing together two different atomic species, the fermionic ^{40}K and the bosonic ^{87}Rb . In the next two subsections we will give a brief overview on our experimental apparatus and on the main steps to produce the ^{40}K - ^{87}Rb mixture. The reader can find a more detailed description in [59].

²Fermions loaded in two spin state are no more indistinguishable and can collide.

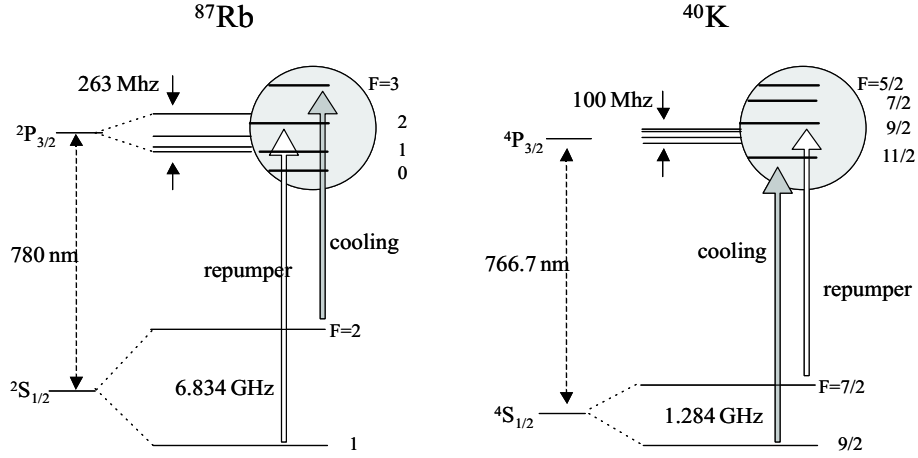


Figure 1.2: Hyperfine structure of ^{87}Rb and ^{40}K . The light grey indicates the transition used to cool the atoms while the white one is the repumper transition.

1.3.1 Experimental setup

- ^{40}K and ^{87}Rb atoms:

Our Fermi-Bose mixture is composed by two stable isotopes of different alkali atoms. The Fermi gas is composed of ^{40}K atoms while we employ ^{87}Rb atoms for the Bose gas. The choice of these atomic species is suggested by several reasons. First of all, alkali atoms are well suited for cooling methods based both on laser light and thermalization processes because of their internal energy-level structure and their low probability of three-body collisions which could produce losses of atoms from the trap. Furthermore the energy levels of such atoms are easy to handle since their optical transitions can be excited by the available laser sources. Finally, Potassium atoms have in nature two bosonic isotopes ^{41}K and ^{39}K (nuclear spin $I = 3/2$) and one fermionic, ^{40}K (nuclear spin $I = 4$). Since Potassium combined with Rubidium gives the unique possibility to study both a Bose-Bose mixture [8] and a Fermi-Bose mixture [23]. Rubidium atom is instead present in nature in two bosonic isotopes: ^{85}Rb and ^{87}Rb . The former is characterized by an interparticle attraction with a scattering length $a = -10a_0$, where a_0 is the Bohr radius. A negative scattering length carries out instability in the system which could lead to the collapse of the system [14]. Nevertheless it is possible to produce a stable condensed gas of ^{85}Rb atoms tuning the scattering length by applying an homogeneous magnetic field which shifts the atomic levels (Feshbach resonances) [63, 64]. The other bosonic isotope, ^{87}Rb , has, on the contrary, a positive scattering length $a = 99a_0$ [65] which guarantees

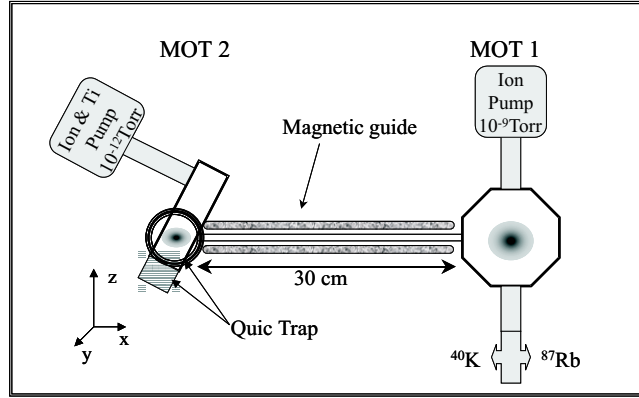


Figure 1.3: Scheme of our experimental setup: atoms of both species are cooled and trapped in the first MOT and then transferred in the second MOT, where they are magnetically trapped.

a stability with respect to the Bose-Einstein condensation. We remind that ^{87}Rb has been the first atomic species brought to the condensation in 1995 [1].

- Hyperfine structure of ^{40}K and ^{87}Rb :

In Fig. 1.2 we report the internal level structure of ^{40}K compared with the one of ^{87}Rb . The internal states are labelled with the quantum number F which identify the total angular momentum of the atoms³. Despite of the relatively small separation between the excited states ($\Gamma = 1$ GHz) of ^{40}K , we are able to reach Sub-Doppler temperatures using laser cooling method with the D_2 line ($S_{1/2} \rightarrow P_{3/2}$). Furthermore, ^{40}K exhibits a peculiar hyperfine structure with both the excited states and the ground states inverted. This complete inversion is caused by its large nuclear spin ($I = 4$) that points in the opposite direction with respect to the nuclear magnetic moment. As a consequence, the ground state of ^{40}K has a large angular momentum, $f = 9/2$; this implies the existence of many magnetically trapped Zeeman levels ($m_F = 9/2; 7/2; 5/2; 3/2; 1/2$). In Fig. 1.2, we also report the two optical wavelength (known as cooling and repumper light) used for the laser cooling of the two species.

- The cells:

³The total angular momentum is $F = J + I$, with J the total electronic momentum and I the nuclear one.

The heart of our experimental apparatus is composed by two cells which are joint by a transfer tube surrounded by a magnetic guide, as is shown in Fig. 1.3. Each cell is furnished with optical windows for the access of the different laser beams and connected to a vacuum pump. The pumps are necessary to obtain a lifetime of the mixture much longer than the characteristic time of collisions between the trapped mixture and the background gas which determines the main loss process of our system. The atoms are initially captured in the first cell where a ion pump maintains a pressure of 10^{-9} Torr. The atoms are then transferred into the second cell where the pressure is fixed at 10^{-12} Torr by another ion pump. The transfer tube is 30 cm long tube with radius of 4 mm and maintains a differential pressure between the two cells.

- Laser sources:

The aim of our experiment is to cool simultaneously a Bose and a Fermi gas until the degeneracy is reached. The production of a mixture introduce a higher complexity in our apparatus with respect to the standard single specie set-up since the two gas exhibit different optical and magnetic characteristic. In particular, the optical transitions needed to cool the two gases are notably far one from the other, and we have to handle with different laser sources. As reported in Fig. 1.2, the cooling optical transitions for ^{87}Rb as a wavelength of 780 nm, while the one for ^{40}K is at 766.7 nm. In the case of Rubidium, the splitting of the hyperfine levels in the ground state is so large ($\Delta\nu = 6.85$ GHz) that we are forced to use two diode lasers at 780 nm, one operating on the repumper and the other on the cooling transition. Both diode lasers, home-made grating stabilized external cavity lasers, are locked to different atomic reference signals of ^{87}Rb . The cooling light is splitted in two part: one part goes to generate the frequency resonant with the $F = 2 \rightarrow F' = 2$ transition needed for the optical pumping of Rubidium, while the second one gives the frequency of the MOTs, red detuned respect to the $F = 2 \rightarrow F' = 3$ transition (the typical detuning is $\Delta \simeq -3\Gamma$). Furthermore, a part of this latter beam is also used for the push beam⁴ and/or for the imaging beam which is resonant with the $F = 2 \rightarrow F' = 3$ transition. The repumper light (see Fig. 1.2) is instead produced by the other diode laser. This laser light is resonant with the $F = 1 \rightarrow F' = 2$ transition, and is needed for the optical pumping sequence. The MOTs cooling and repumping lights, with typical ratio between the two powers 3:1.

All the laser lights needed to manipulate Potassium atoms are instead obtained by a

⁴The push beam is needed to transfer atoms from the first to the second MOT, and has to be slightly on the red of the $F = 2 \rightarrow F' = 3$ transition

single laser source combined with acousto-optic modulators (AOM). Indeed, differently from Rubidium, the hyperfine splitting of the Potassium ground state is only 1.8 GHz so that we are able to produce all the frequencies we need thanks to an home-made Ti:Sa, pumped by a Nd:Yag (Millennia X, Spectra Physics). The beam exiting from the Ti:Sa laser is splitted in two parts, one for the cooling and the other for the repumping, with a controllable ratio typically of the order of 4:1. The cooling part is then divided in other two beams, one for the MOT and the other for the imaging, push beam and the optical pumping. The cooling frequency for the MOTs is red shifted respect to the closed transition $F = 9/2 \rightarrow F' = 11/2$. The light for the imaging, is instead resonant with $F = 9/2 \rightarrow F' = 11/2$, while the one for the push beam must be slightly blue shifted respect to $F = 9/2 \rightarrow F' = 11/2$. Finally, the optical pumping light is resonant with $F = 9/2 \rightarrow F' = 9/2$. We generate the frequency for the repumper with three different AOMs that produce the light resonant with the $F = 7/2 \rightarrow F' = 9/2$ transition.

Our four laser beams (cooling-repumper for Rb and cooling-repumper for K) are injected simultaneously in a semiconductor tapered amplifier (MOPA) which provides the necessary power for the two magneto-optical traps (MOTs). The beams for Potassium and for Rubidium have opposite polarization. This gives us the possibility to choose the ratio between their powers using a halfwave plate displaced before the MOPA.

1.3.2 Experimental procedure

The aim of our experiment is to cool ^{40}K atoms until the degeneracy is reached ($T < T_F$). To achieve this regime, we first cool and trap ^{87}Rb and ^{40}K atoms in a standard double magneto-optical trap. We then load the cold sample ($\sim 50 \mu\text{K}$) in a magnetic trap where a selective evaporative cooling is performed on Rubidium atoms. At this point, the Potassium component is sympathetically cooled down to the degenerate regime. Figure 1.4 shows a schematic representation of the main phases of our experimental procedure and a brief discussion is reported below.

- 1° step: Loading ^{87}Rb atoms in the second MOT

At first, the background vapor of ^{87}Rb atoms in the first cell is loaded into the first MOT. The first MOT is produced by combining a quadrupole magnetic field with two pairs of retroflected beams along the x - y directions and two independent beams along the z -axis, as shown in Fig. 1.4(a). The laser light is composed by a superpo-

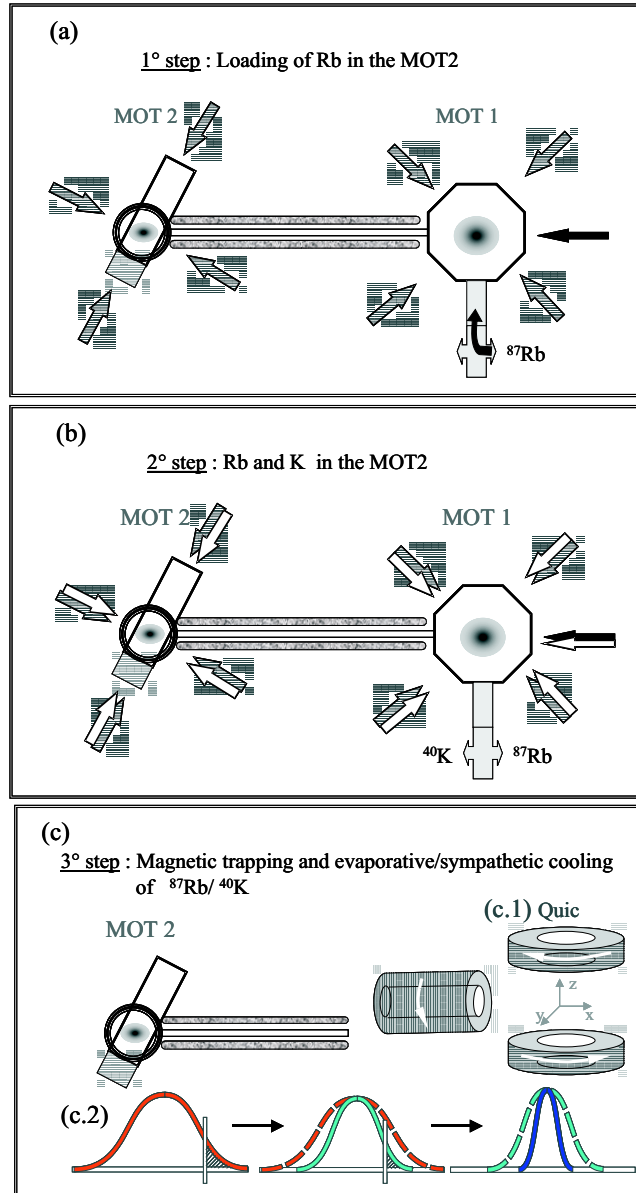


Figure 1.4: Sketch of the experimental sequence. Our procedure consists basically of 3 steps: (a) Transfer of bosons (^{87}Rb) from the first to the second cell using a continuous push beam. (b) transfer of fermions (^{40}K) by a pulsed push beam. Both species are now magneto-optically trapped (MOT 2) in the second cell. (c) Loading of the mixture in a magnetic trap using a QUIC configuration of the coils (c.1). In this magnetic trap, we perform a radio-frequency evaporative cooling of Rb atoms, which thermalize reaching lower temperature (c.2).

sition of red detuned ($\omega_L < \omega_0$) cooling and repumper beams. The quadrupole field⁵ splits the atomic levels in many position-dependent Zeeman sub-levels. The atoms occupying a sub-level resonant with the laser light ($\omega_{m_F} \simeq \omega_L$) experience a braking force ($F = -\gamma v$) produced by the radiation field which slows down its motion. In the meanwhile, the atoms are transferred from the first to the second cell where they are again trapped in the second MOT. The transfer is achieved using a continuous pushing beam acting on the red of the $F = 2 \rightarrow F' = 3$ transition. In about 25 s we are able to transfer and then to recapture in the second MOT about 10^9 Rb atoms at a temperature of $50 \mu\text{K}$.

- 2° step: ^{87}Rb and ^{40}K atoms in the second MOT

After the first 25 s during which just the Rb atoms are loaded in the second MOT, we rotate the mechanical halfwave plate to inject into the MOPA also the laser beams at the Potassium frequency. In this stage the ratio between the K and Rb light is about 10:1. Potassium atoms, initially loaded in the first MOT, are transferred into the second MOT thanks to a pulsed push beam, as reported in Fig. 1.4(b). We pulse the push beam every 200 ms, taking care the quadrupole field of the first MOT is switched off during each shot. At the end of this procedure (10 s) also 10^5 atoms of ^{40}K coexist with 10^9 Rb atoms in the second MOT.

- 3° step: Magnetic trapping and evaporative/sympathetic cooling

While in the MOT phase the mixture are trapped and cooled at the meantime, in this stage we trap the two gases using a magnetic field and we cool the ^{87}Rb atoms using the usual technique of evaporative cooling [15]. The K atoms are instead sympathetically cooled because of the collisions with the Rb gas.

MAGNETIC TRAPPING: We trap the atoms in a conservative potential produced by magnetic fields. The magnetic potential splits the hyperfine levels in Zeeman sub-levels

$$E(\vec{r}) = E_0 + m_F g_F \mu_B B(\vec{r}), \quad (1.15)$$

where E_0 is the energy of the unperturbed level, m_F labels the Zeeman level, g_F is the Lande' factor, μ_B is the Bohr magneton, and $B(\vec{r})$ the applied magnetic field. Just the atoms occupying a Zeeman sub-level with $m_F g_F > 0$ can be magnetically trapped because their energy $E(\vec{r})$ increases with $B(\vec{r})$ (Wing theorem) [60]. These

⁵This magnetic field is realized using two coils in anti-Helmholtz configuration.

states are named *low-field seekers*. In our case we trap both Rb and K atoms in their doubly polarized states, in which the nuclear and electronic spin components have the largest possible values along the direction of the magnetic field. In particular, ^{87}Rb atoms are in the $|2, 2\rangle$ state, while ^{40}K atoms in $|F = 9/2, m_F = 9/2\rangle$. Note that the sample have to be completely polarized before transferring it into the magnetic potential to avoid large losses of atoms (interstate collisions). This can be done by using an optical pumping light which is selective on the Zeeman sub-level.

To realize the magnetic trap, we use three coils in the quadrupole Ioffe-Pritchard configuration (QUIC) consisting of two coils which generate a radial quadrupole field and a third one (pinch coil) orthogonal to the quadrupole axis which produce a harmonic confinement (see Fig. 1.4(c.1)). The effective magnetic confinement experienced by the atoms depends on the first ($\partial B/\partial z = B'$) and second derivative ($\partial^2 B/\partial z^2 = B''$) of the magnetic field

$$U(z, r) \propto \left[B_0 + \frac{1}{2} B'' z^2 + \frac{B'^2}{2B_0} r^2 \right], \quad (1.16)$$

where B_0 is the bias field. Atoms experience a cylindrical harmonic potential with different frequencies along the axial and radial directions. The frequency along the axial pinch direction (weak axis of the trap) given by

$$\omega_z \propto \sqrt{\frac{B''}{m}} \text{ while in the radial direction } \omega_r \propto \sqrt{\frac{B'^2}{mB_0}}. \quad (1.17)$$

The trap frequencies measured for the ^{87}Rb cloud are $\omega_z \simeq 2\pi \times 16.3$ Hz and $\omega_r \simeq 2\pi \times 197$ Hz and the ones for ^{40}K atoms are $\omega_z \simeq 2\pi \times 24$ Hz and $\omega_r \simeq 2\pi \times 317$ Hz. Difference in the trapping frequencies experienced by the two species has to be ascribe to their different masses, indeed the ratio between the frequency scales as $\sqrt{m_{\text{Rb}}/m_{\text{K}}}$. We can typically transfer from the MOT to the QUIC trap about 10^5 atoms of ^{40}K and 5×10^8 of ^{87}Rb at a temperature of $100 \mu\text{K}$.

EVAPORATIVE AND SYMPATHETIC COOLING: Once the mixture is trapped in the magnetic potential, we perform an evaporative cooling only on the Rb component. The basic idea of this technique is to selectively remove the hottest atoms from a trapped states to untrapped ones with a radio-frequency knife. This signal couples indeed trapped Zeeman levels to untrapped ones⁶ We continuously remove atoms with energy larger than the average energy while the remaining atoms equilibrates at a lower mean temperature through elastic collisions, as schematized in Fig. 1.4(c.2).

⁶The Zeeman splitting between the Rb levels is of the order of tens of MHz for the typical magnetic field applied (1 Gauss).

One can stop the evaporation when we reach the Bose-Einstein condensation of the Rb cloud to have a degenerate Fermi-Bose mixture or to continue until all the bosonic atoms are removed to obtain a pure Fermi gas. We typically achieve the condensation of ^{87}Rb at $T = 80\text{nk}$ with $N_{\text{Rb}} \sim 10^5$. During all the evaporation ramp the Potassium atoms thermalize with the colder Rb gas through elastic collisions and 2×10^4 atoms reach the degenerate regime.

During the evaporation of bosons, the Bose and Fermi gases are in thermal equilibrium each others. We have found the same temperature for both gases by fitting their momentum profile with a Boltzmann distribution ($T \gtrsim T_c, T_F$)⁷. We have also checked the thermal equilibrium during all the evaporation phase by measuring T as a function of the radio-frequency signal applied. As we will discuss in Sec. 1.4.1, the efficiency of the thermalization is also confirmed by the high interspecies scattering length measured. Note that the thermal capacity of the Bose gas decreases with the temperature as $(T/T_c)^3$ and in the deep degenerate regime ($T \ll T_c$), the thermal capacity of bosons becomes smaller than the one of the Fermi gas. In this condition, bosons can no more be considered as a thermal bath for the fermions and the evaporative cooling is then stopped.

At the end of our procedure we obtain a Fermi gas of ^{40}K coexisting with a Bose-Einstein condensate of ^{87}Rb well below the temperature of degeneracy, i.e. $T < T_F, T_C$. The minimum temperature reached in our apparatus is $0.2T_F$. For our experimental parameters, the Fermi temperature is $T_F=250\text{ nK}$ and the critical temperature $T_c=110\text{ nK}$ for a sample composed by 10^4 fermions and 2×10^4 bosons. These atom numbers correspond to peak-densities of the order of $n \simeq 10^{14}\text{ cm}^{-3}$ for Rb and $n \simeq 5 \times 10^{12}\text{ cm}^{-3}$ for K.

- 4° step: Imaging the mixture

We observe the density distribution of the two clouds using the standard absorption imaging technique. We switch off the magnetic trap and we let the mixture expand for a suitable time to avoid problems related to the high density of the samples. We then shine the mixture with a two-colors resonant probe beams delayed by an appropriate time to have two spatially separate absorption images which are captured by a CCD camera. From the analysis of these images, we can extract fundamental information on the system such as the atom numbers of each specie, the temperature and the momentum distribution. The laser intensity revealed by the camera and the density

⁷Note that in the degenerate regime the two gases have a distribution which is nearly temperature independent.

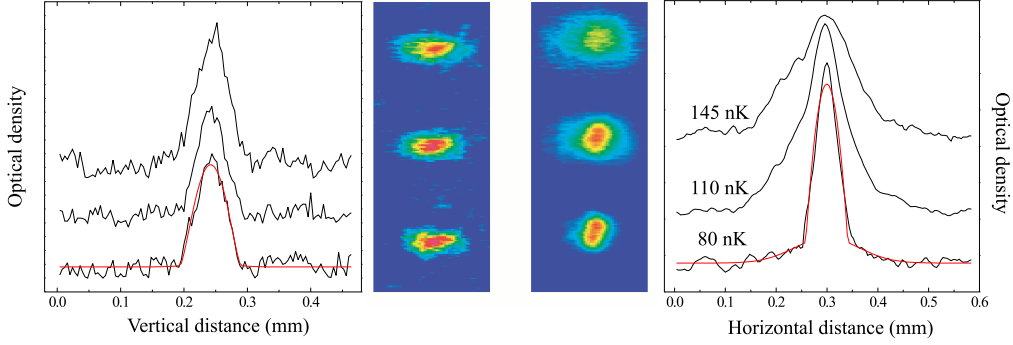


Figure 1.5: Simultaneous onset of Fermi degeneracy for ^{40}K (left) and of Bose-Einstein condensation for ^{87}Rb (right). The absorption images are taken for three decreasing temperatures, after 4.5 ms of expansion for K and 17.5 ms for Rb, and the sections show the profile of the momentum distributions [23].

of each specie are connected by the following relation

$$I_T(x, z) = I_0(x, z) \exp\left[-\sigma \int dy n(x, y, z)\right], \quad (1.18)$$

where n is the atomic density, σ the cross section of absorption and integration is made along the beam direction. The quantity $\sigma \left[\int dy n(x, y, z)\right]$ is the optical density (OP) of the system which is directly measured in the experiment. Assuming that the thermal contact between the two components is efficient also in the highly degenerate mixture, the temperature is determined by fitting the thermal tails of the Bose gas.

In Fig.1.5, we show a series of absorption images of the mixture for three different stages of the evaporation ramp taken after a ballistic expansion. As the temperature is decreased below T_c , we observe the appearance of a narrow peak in the momentum distribution of the Bose gas which is the signature of the condensation. When instead the Fermi gas reaches the degeneracy we observe that, lowering the temperature, its width remains almost constant due to the Fermi pressure which is a direct consequence of their statistics. We fit the two clouds with a Thomas-Fermi distribution [58, 14]. For instance, typical sizes of the trapped Fermi gas are $R_a = 52\mu\text{m}$ and $R_r = 5.1\mu\text{m}$ in axial and radial direction, respectively. The BEC is completely immersed in the Fermi sea due to its smaller dimension.

1.4 Fermi-Bose mixture

The production of a Fermi-Bose mixture solves on the one hand the problem to cool down a Fermi gas and on the other hand opens the exciting possibility to investigate interspecies interaction phenomena. The first goal of such kind of studies is to determine the interspecies scattering length which affects the behavior of the system in several phenomena.

1.4.1 Measurement of the interspecies scattering length

We now report on our effort to characterize the dominant collisional mechanisms between fermions and bosons. For the μK temperatures common in ultracold atom traps, interactions are dominated by two-body *s*-wave scattering⁸. As mentioned earlier, the two-body collisions between spin-polarized fermions are completely suppressed down to μK -temperature, due to the Pauli principle. Fermions coexisting with a Bose gas can instead collide with bosons and the interspecies scattering length a_{BF} is the relevant quantity governing collisional mechanisms. Note that the knowledge of a_{BF} is not only crucial to determine the efficiency of sympathetic cooling but also necessary to predict the regimes of stability and the phase separation/overlap of the mixtures. In addition, a_{BF} is needed to determine the occurrence of Feshbach resonances, which allows to tune the zero-field scattering length a_{BF} by applying a homogeneous magnetic field [37].

We have measured the value of a_{BF} by studying the center-of-mass motion of both gases when a dipolar mode is excited [66] of the mixture. We induce a dipolar motion by displacing the minima of the magnetic potential. From the damping of the coupled oscillations we estimate the interspecies scattering length a_{BF} . This procedure has been originally used for a Bose-Einstein condensate (BEC) loaded in two different hyperfine levels [67] and then extended to a gas of fermions in two spin-states [68] and to a mixture composed of different atoms [69]. The basic idea is that, while in a pure harmonic potential, single gases undergo undamped collective oscillations, two gases experiencing different trap frequency can exhibit a damped out-of-phase motion. From the damping rate we can extract quantitative information about the scattering processes.

To perform these measurements we magnetically trap ^{87}Rb atoms in the $|2, 2\rangle$ state and ^{40}K atoms in $|F = 9/2, m_F = 9/2\rangle$. These doubly polarized states have the

⁸For typical collisions, $kR \ll 1$, where $\hbar k$ is the relative momentum and R is the range of the interatomic potential.

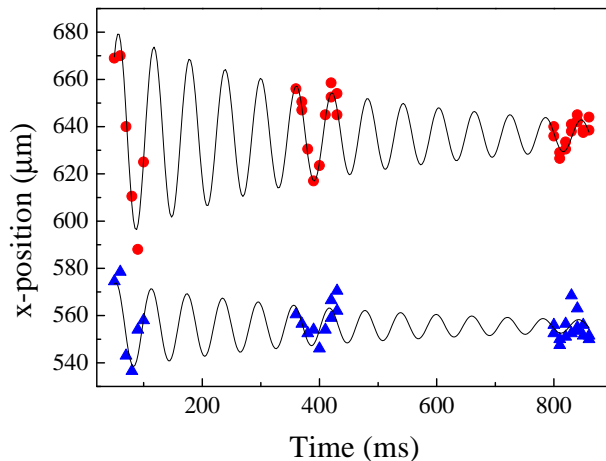


Figure 1.6: Coupled dipolar oscillations of 8×10^3 non-degenerate K (triangles) and 8×10^4 uncondensed Rb (circles) atoms along the axial direction at $T=300$ nK. The two samples oscillate at the same frequency with a collisional rate $\Gamma_{coll}=190 \text{ s}^{-1}$ typical of a hydrodynamic regime. The solid lines are the best fit to the model presented in the text.

maximum coupling with the magnetic field and the two species experience the same trapping potential. The axial and radial harmonic frequencies are $\omega_a = 2\pi \times 24 \text{ s}^{-1}$ and $\omega_r = 2\pi \times 317 \text{ s}^{-1}$ for K, while those for Rb are a factor $(M_{Rb}/M_K)^{1/2} \approx 1.47$ smaller. This different trapping frequencies allows one to induce a relative motion between the two components.

Dipolar oscillations are excited by a sudden displacement of the trap minimum in the axial direction z . This is easily done by changing the ratio of currents in the trap coils which corresponds to modify the value of the bias field B_0 (see Eq. (1.16)). With an appropriate choice of the amplitude and timing of such displacement we can excite a quasi-pure dipolar oscillation⁹, with no apparent higher-order (shape) oscillations. The amplitude of those oscillations is also chosen small enough to preserve the overlap of the two clouds even in the degenerate regime.

We perform the measurement using a non-degenerate K-Rb mixture at temperature $T = 300 - 500$ nK for which the collisional rate can be directly related to the elastic cross-section. As shown in Fig. 1.6, due to the interspecies collisions, both K and Rb oscillations are damped, and the K motion is also frequency-shifted. To describe the coupled center-of-mass motion of the two cloud, we use a classical model for two

⁹The typical mean relative velocity of K and Rb samples during the subsequent oscillations is $\sqrt{\langle v^2 \rangle} = 5 \text{ } \mu\text{m/ms}$.

harmonic oscillators coupled through a viscous damping. The coupled equations of motion are

$$\begin{aligned}\ddot{z}_{Rb} &= -\omega_{Rb}^2 z_{Rb} - \frac{4}{3} \frac{M_K}{M} \frac{N_K}{N} \Gamma_{coll} (\dot{z}_{Rb} - \dot{z}_K) \\ \ddot{z}_K &= -\omega_K^2 z_K + \frac{4}{3} \frac{M_{Rb}}{M} \frac{N_{Rb}}{N} \Gamma_{coll} (\dot{z}_{Rb} - \dot{z}_K),\end{aligned}\quad (1.19)$$

where M is the total mass $m_K + m_{Rb}$, N the total number of atoms $N_K + N_{Rb}$, and Γ_{coll} is the rate of K-Rb two-body elastic collisions. This model well describes coupled dipolar motion of the two clouds, whereas all the microscopic damping mechanisms are described by the quantity Γ_{coll} . Assuming two Boltzmann distributions for the gases, the collisional rate is related to the elastic cross-section

$$\Gamma_{coll} = \bar{n} \sigma v_{th}, \quad (1.20)$$

where $v_{th} = \sqrt{8k_B T / \pi M}$ is the rms relative thermal velocity and the mean density in the overall region is $\bar{n} = (\frac{1}{N_K} + \frac{1}{N_{Rb}}) \int n_K n_{Rb} d^3x$. Finally, the collision cross-section σ depends on the interspecies s-wave scattering length as

$$\sigma = 4\pi a^2. \quad (1.21)$$

From Eq. (1.19), one find that the system has two normal modes, whose frequencies ω and damping times τ vary with the collisional rate Γ_{coll} . We solve numerically Eq. (1.19) for the typical ratio of atom numbers, $r = N_{Rb}/N_K = 7.5$. At low collisional rate, in the so-called collisionless regime ($\omega_{Rb}\tau, \omega_K\tau \ll 1$), the two samples are predicted to oscillate at their bare frequencies ($\omega_K \approx 2\pi \times 24 \text{ s}^{-1}$, $\omega_{Rb} \approx 2\pi \times 16.3 \text{ s}^{-1}$), and the ratio of the two damping times scale as the inverse ratio of the total mass of each sample. As the collisional rate increases, the damping time of the two normal modes decreases and their frequencies are shifted towards an intermediate value. Here each sample oscillates at a combination of both normal modes. Finally, at very high collisional rate ($\omega\tau > 1$) the system enters in the hydrodynamic regime. Here there is a mode at this intermediate frequency with low damping and a second overdamped mode whose frequency rapidly decreases with increasing Γ_{coll} . The latter corresponds to our experimental situation (see Fig. 1.6): the two samples oscillate at the same frequency, almost in phase and with a long damping time. Note that, the collisional rate Γ_{coll} depends strongly on the relative phase gained by K and Rb atoms during their motion. This dependence helps us to provide an accurate determination of the experimental Γ_{coll} and then of s-wave scattering length a_{BF} , since the phase of the oscillations can be determined with relatively high accuracy. As already reported

in our previous work [70], one can extract the value of the collision cross-section and hence of a_{BF} fitting the experimental data for the dipole oscillations with the solution of Eq. (1.19). We have repeated this procedure by varying the temperature in the range $T=300-500$ nK, the total number of atoms in the range $N=10^4-5 \times 10^5$, and the ratio r from 2.5 to 7.5. From the above measurement, we find a large s-wave scattering length between the Fermi and Bose gas

$$|a_{BF}| = 410_{-80}^{+80} a_0. \quad (1.22)$$

This value is in good agreement with the one reported in our previous work [69] which was found from the measured ^{41}K - ^{87}Rb scattering length with a re-scaling of mass. This result gives a signature of the strong interspecies interaction between the two gases¹⁰. The value (1.22) is obtained by a weighted average of the different measurements performed with different atom numbers and temperature. The uncertainty is dominated by a 40% a priori uncertainty in the number density. Note that such large scattering length found also seems to indicate the attractive nature of the interspecies interactions, since a positive one would be compatible only with a much smaller magnitude. However, one can not extract the sign of a_{BF} by studying the dipolar oscillations because of the square dependence of a_{BF} from the collisional cross-section. Another method to measure directly the scattering length is based on the study of rethermalization mechanism performed on a thermal Fermi-Bose mixture [23]. The idea is to drive out the system from the initial equilibrium by modulating the trapping potential at twice the radial oscillation frequency of just the Rubidium atoms ($\nu \sim 420$ Hz). After this phase of selective heating, one can study the subsequent heating of the Potassium, mediated by the elastic collisions with the Rubidium component and extract the scattering length. In principle this method provides also information on the sign of the interaction by measuring the thermalization rate as a function of the temperature of the mixture. This procedure has been followed in the case of ^{41}K - ^{87}Rb [69]. In the case of ^{40}K - ^{87}Rb this method falls down because, due to the large value of a_{BF} , the system is in the Wigner regime, i.e. the collisional cross-section will not depend on the temperature. As we will see in the next sections, the system exhibits phenomena which are peculiar only of a binary mixture with attractive interspecies interaction.

¹⁰For comparison, note that the s-wave scattering length between bosons of the ^{87}Rb cloud is $|a_B| = 99a_0$.

1.4.2 Mean field approach

Atomic ultracold gases are also a well-suited system from a theoretical point of view. Indeed, due to the diluteness of these atomic gases, the interparticle interactions are relatively easy to handle, as already discussed in Sec. 1.2.2. In a Bose-Einstein condensate, the collisions between bosons are fully taken into account by a mean field potential which depends on the s-wave scattering length a_{BB} (zero-order perturbation). Considering this potential, the condensate is described by the well known Gross-Pitaevskii equation (GPE) [14, 15], which is Schrödinger equation with an extra non-linear term relative to the mean field potential. We now consider a Bose-Einstein condensate coexisting with a Fermi gas. The interspecies interaction can again be described by a mean field potential proportional to the fermions density and to the interspecies s-wave scattering length a_{BF} . One has thus to add the Fermi-Bose potential to the GPE

$$\left[-\frac{\hbar^2}{2m_B}\nabla^2 + V_B(\mathbf{r}) + g_{BB}n_B(\mathbf{r}) + g_{FB}n_F(\mathbf{r}) \right] \phi(\mathbf{r}) = \mu_B\phi(\mathbf{r}), \quad (1.23)$$

where $n_B(\mathbf{r})$ is the bosons density, $\phi(\mathbf{r})$ is the condensate wave function. The boson-boson and boson-fermion interactions are proportional to the coupling constants $g_{BB} = 4\pi\hbar^2 a_{BB}/m_B$ and $g_{BF} = 2\pi\hbar^2 a_{BF}/m_R$, where $m_{B,F}$ are the atomic masses while $m_R = m_B m_F / (m_B + m_F)$ is the reduced mass. As already shown, for our Rubidium-Potassium mixture, the values of the scattering lengths are $a_{BB} = 99 a_0$ and $a_{BF} = -410 \pm 80 a_0$.

Similarly, also the Thomas-Fermi equation describing the Fermi gas have to include the interspecies mean field term [71, 72]

$$n_F(\mathbf{r}) = \frac{\sqrt{2m_F^3}}{3\pi^2} [\mu_F - V_F(\mathbf{r}) - g_{FB}n_B(\mathbf{r})]^{3/2}, \quad (1.24)$$

where μ_F is the chemical potential, n_F the Fermi-cloud density and $V_{B,F}$ the harmonic trapping potential for the two species.

From Eq. (1.23-1.24), it turns immediately out that the density distribution of both gases are modified due to their mutual interaction. The study of such modification will provide a clear indication and a test for the mean field approach. We have numerically solved the two coupled equations (1.23) and (1.24) for our typical number of atoms, our nominal trap frequencies and for $a_{BF} = -410a_0$ [73]. Our result is reported in Fig. 1.7 where we show the new ground state of the trapped mixture. The atom number considered here are 10^4 and 3×10^4 , for Potassium and Rubidium respectively. The dotted curves show the calculated density profiles along the direction

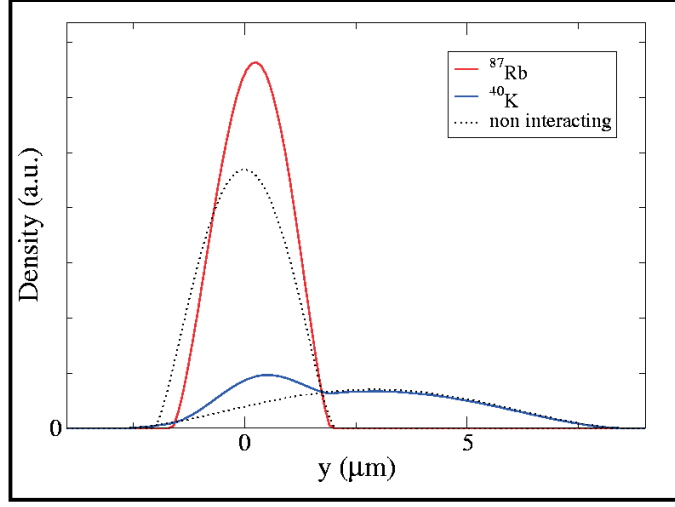


Figure 1.7: Density profile of the Bose-Einstein condensate and of the Fermi gas in trap. The dotted lines correspond to the non-interacting case ($a_{BF} = 0$). The higher density profile is the one of the condensate. The effect of the strong interspecies attraction ($a_{BF} = -410a_0$) is an increase of the density of both species in the overlap region (continuous lines). The curves are the result of the mean-field calculations.

of the gravity of both the clouds in non-interacting case ($a_{BF} = 0$). Also in this case the two distributions are not concentric due to a gravitational sag between the two clouds, which affects both the horizontal and vertical directions, due to a small misalignment of the magnetic trap with respect to the direction of the gravity¹¹ [74]. The peak-density of the Fermi gas is much lower than the one of the condensate. Indeed, the Fermi pressure stabilizes the fermionic system to a much larger shape and consequently lower density respect to the BEC. If we now switch on the attractive interaction $a_{BF} = -410 a_0$, the situation notably changes, as clearly appear from the continuous lines in Fig. (1.7). From the attractive nature of the interspecies interaction follows the absence of any phase-separation between the two clouds: they still keep good spatial superposition, despite of the gravitational sag, and in particular, with the condensate completely immersed in the Fermi "sea".

Furthermore, we observe a large increase of the density of both the species in the overlap region. This increase is evident for both the components, but even larger in the case of Potassium since the effective influence of the interaction depends from the density of the other specie, and the mean density of a Bose-Einstein condensate

¹¹We can consider the relative gravitational sag between the two clouds and thus the Fermi cloud will experience a trapping potential $V_F(\mathbf{x}) = \frac{1}{2}m_F [\omega_{F\perp}^2(x^2 + (y - y_0)^2) + \omega_{Fz}^2(z - z_0)^2]$. The values of the displacement between the two potential centers are $y_0 = 3.6 \mu\text{m}$ and $z_0 = 20 \mu\text{m}$.

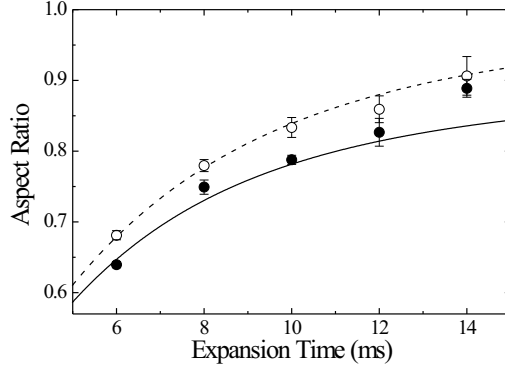


Figure 1.8: Modification of the expansion of a K Fermi gas due to the interaction with a Rb BEC. The radial-to-axial aspect ratio of a cloud of 4×10^4 fermions evolves more slowly in presence of 3.5×10^4 condensed bosons (solid circles) than in presence of a similar number of uncondensed bosons (open circles). Each data point is the average of five or six measurements. The dashed line is the calculated expansion of a pure Fermi gas, while the solid line is the prediction for an interacting Fermi gas.

($n \simeq 10^{14}$) is typically two orders of magnitude larger than the one of a Fermi gas ($n \simeq 10^{12}$).

The deformed ground state of the system is predicted to affect also the dynamics of the mixture leading to a modification of the frequencies of collective excitations [75, 76] and of the expansion of the two clouds from the trap [77]. We have actually observed a modification of the expansion of both the condensate [23] and the Fermi gas [78].

1.4.3 Expansion of the Fermi gas

The study of the expansion of an ultracold gases is one of the major tools to study the interactions between atoms. As we switch off the confinement, the atoms freely expand and the interaction energy starts to be converted into kinetic energy. From the knowledge of the expansion velocity, one can trace back to the interaction field. For instance, the anisotropic expansion exhibited by a condensate gave the first direct evidence of the role of the boson-boson interaction [1, 2, 3]. Recently, a large anisotropic expansion has also been observed in a two-component Fermi gases at Feshbach resonances [79, 80, 81] which has revealed the high collisional rate of the mixture [82, 83]. Similarly, in order to observe the effect of their large mean-field interaction, we have studied in detail the expansion of our Fermi-Bose mixture by

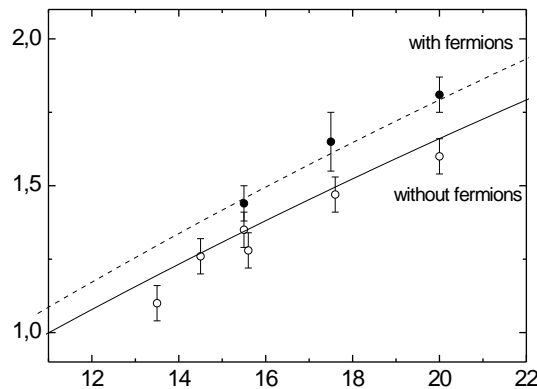


Figure 1.9: Modification of the expansion of a Rb condensate due to the interaction with a K Fermi gas. The radial-to-axial aspect ratio increases more rapidly with time for condensates created with K (solid circles) than for pure condensates (open circles).

suddenly switching off the magnetic confinement [23, 78]. The expansion of a non-interacting Fermi gas exhibits an isotropic expansion and, despite to the anisotropic magnetic confinement, the cloud tends to a symmetric shape with $R_a = R_z$, similarly to a classical gas. When we switch on the interactions between the Fermi and Bose gas, the situation notably changes. The first quantity which gives important information on the interspecies interaction is the radial-to-axial aspect ratio of the cloud, defined as R_r/R_a . In Fig. 1.8 and Fig. 1.9, we report the evolution of the aspect ratio of both the Fermi gas and the BEC. It is evident from the data point that the Fermi gas exhibits an aspect ratio always smaller than the one measured for a Fermi gas coexisting with a dilute thermal cloud of bosons [78] (see Fig. 1.8), while the condensate, on the contrary, inverts its aspect ratio more rapidly in presence of the Fermi gas [23] (see Fig. 1.9). This opposite behavior is somehow surprising because both gases are subjected to a similar interspecies interaction. The reason of such difference has to be found on the different atomic densities and on the different weight of interaction energy respect to the other energy (boson-boson interaction for the condensate and the kinetic energy for the fermions). On the one hand, the expansion of bosons reveals the expected enhancement of density in trap (see Fig. 1.7) which corresponds to a effective tighter confinement which tends to speed up the evolution of the aspect ratio during the expansion. On the other hand, the behavior of the Fermi gas gives evidence that the mutual attraction felt by the two species in the first moment of the expansion also plays a crucial role in the subsequent dynamics. Indeed, during the early stage of the expansion, each of the two gases experiences a

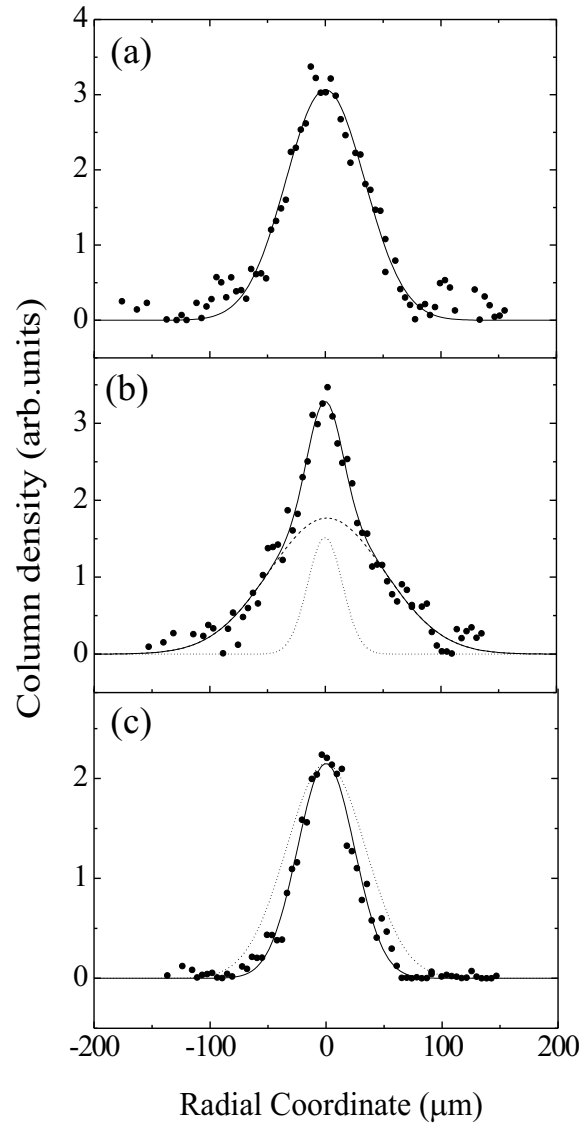


Figure 1.10: Radial momentum distribution of the Fermi gas, detected after 12 ms of expansion, for different atom number in the mixture. For $N_F = 2 \times 10^4$, (a) we observe that below $N_B = 6 \times 10^4$ the distribution is slightly affected by interspecies potential, while (b) above $N_B = 6 \times 10^4$ a bimodal structure appears. (c) After the collapse, the remaining 1.2×10^4 fermions coexisting with 7.4×10^4 bosons exhibit a narrower distribution than the non-interacting gas (dotted line).

time-dependent trapping potential produced by the other species. In this phase the negative interaction energy is converted into kinetic energy which, in general, can be unevenly distributed between the two samples. Indeed, the Fermi gas is taking a large part of the interaction energy, which results in a largely reduced kinetic energy in the radial direction, and therefore in the slower evolution of the aspect ratio¹², as shown in Fig. 1.8. This interpretation is also confirmed by the observed dependence of the expansion of the Fermi gas on the atom numbers in the mixture [78]. In particular, the aspect ratio decreases by increasing the effective overlap region between the two species. We can increase density in the overlap region by increasing N_B at constant N_F . In this case, we observe the appearance of a double distribution in the radial profile of fermions with a narrow peak surrounded by a broader distribution, as illustrated in Fig. 1.10. We attribute the narrow distribution to the fermions trapped into the condensate while the broader distribution is occupied by the more energetic atoms outside the overlap volume which can expand freely. Note that we are able to observe the bimodal distribution only in the radial direction, confirming that the interaction energy between the two clouds is exchanged mainly in the more tightly confined direction. From the observed behavior of the expanding Fermi gas, we can conclude that the momentum distribution reflects somehow the spatial distribution in the trap.

1.4.4 Collapse of the Fermi gas

The modified expansion of the Fermi gas can be completely described in the framework of the mean-field approximation [76, 82]. Although the atom numbers in the mixture are increased above some critical value, the situation changes dramatically. We have observed instabilities in the system which are driven by the interspecies attraction. As we will discuss in this section, such instabilities can not more be described using a mean field approach.

In general, both the non-interacting Fermi gas and the Bose-Einstein condensate are stable systems. The stability of the fermionic gas is indeed assured essentially by the Fermi pressure which arranges the fermions in the trap in a relatively large spatial distribution compared to the one of a Bose-Einstein condensate. Note that this

¹²The theoretical curve has been obtained by a numerical simulation provided by X.J. Liu for our experimental parameters. The numerical calculation are performed with $a_{BF} = -330a_0$ instead of $a_{BF} = -410a_0$, which is the value that better fits also the expansion of bosons, as discussed in Ref. [77].

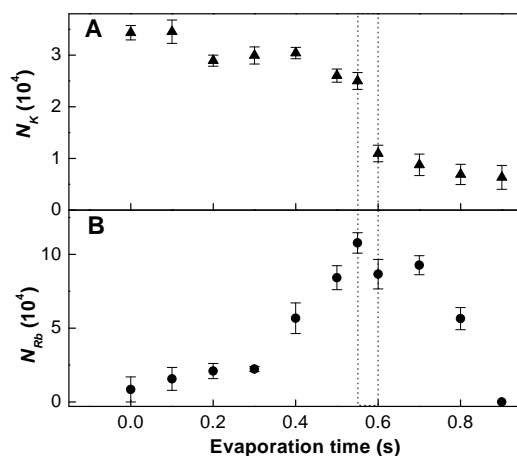


Figure 1.11: Evolution of the number of Potassium atoms N_K (A) during the final stage of the evaporation of condensed Rubidium atoms (B). When the number of condensed atoms N_{Rb} is increased above 10^5 (highlighted region), we observe a sudden decrease of N_K .

pressure acts as a repulsive force on the fermions and it is a general property of any degenerate Fermi system, also present in white dwarfs and neutron stars. The stability of a Bose-Einstein condensate is instead guaranteed by the positive sign of the interspecies scattering length, which corresponds to a net repulsive interaction between the atoms. In the case of a Fermi-Bose mixture, the stability of the system depends essentially by the interspecies mean field $U_{B,F} = g_{BF} n_{F,B}$. As we have already discussed, such interaction tends to squeeze the spatial distribution in trap of both species increasing the peak-density. The potentials which ensure the mixture stability, i.e. the kinetic energy for the Fermi gas and the boson-boson interaction for the BEC, have instead a repulsive nature. Since these latter dominate with respect to the interspecies attraction, the mixture is stable with a lifetime of the system of about a second. When instead the numbers of atoms are increased above a critical value, the repulsive energies of both gases cannot balance the attractions U_F, U_B , and the system can lower indefinitely its energy by increasing further both fermion and boson densities [70, 73]. Indeed, the onset of instability is characterized by an indefinite growth of central densities which triggers the simultaneous collapse of the two species. We have experimental observed the collapse of the Fermi gas as a suddenly drop of the fermions atom numbers to less than half its original value, as shown in Fig. 1.11. As long as the condensate is forming, we observe inelastic losses of K atoms on the same time scale of the evaporation. When the condensed atoms reach a critical threshold (at 0.6 s of the evaporation ramp), the number of K atoms suddenly

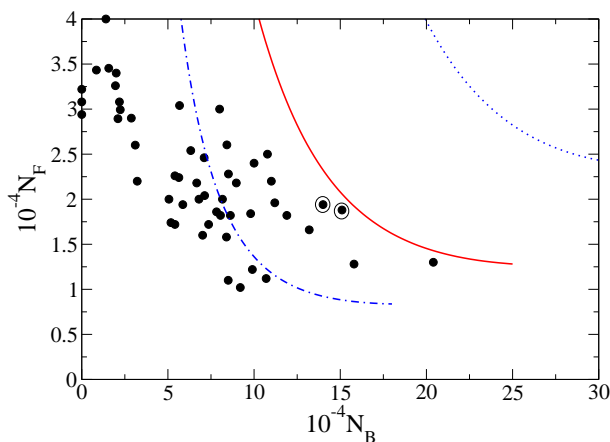


Figure 1.12: Region of stability of the Fermi-Bose mixture, as a function of the number of atoms. The black dots are the experimental points; lines are the theoretical prediction for the boundary between the stable (left) and collapse (right) regions, for three values of the inter-particle scattering length: $a_{BF} = -380 a_0$ (dotted line), $a_{BF} = -395 a_0$ (continuous line), $a_{BF} = -410 a_0$ (dashed-dotted line). The marked dots are found very close to the instability (see text).

drops to a lower value with a duration much shorter than the time scale of the other loss mechanisms observed. Indeed, when we try to span the time interval between 0.55 and 0.6 s, the small shot-to-shot fluctuations of the atom numbers results in either a large ($N_K = 2 \times 10^4$) or a small ($N_K < 10^4$) Fermi gas, i.e. we are not able to follow the dynamics during the collapse which seems to happens on a time $t \ll 50$ ms. Note that the theory predicts the simultaneous collapse of both species. However in the experiment, we have observed only a marginally change in the atom number of the condensate. Indeed, in correspondence of the collapse of the Fermi gas, the depletion of the condensate is only of the order of 2×10^4 atoms. We ascribe this behavior to the 3-body K-Rb losses which alt the collapse of the mixture reducing the number of atoms below the critical values [70]. It is possible to determine experimentally the critical values of the atom numbers at the onset of the collapse [70]. We have found the threshold to be at $N_K \simeq 2 \times 10^4$ and $N_{Rb} \simeq 10^5$. These values are compatible with the ones predicted by the mean-field theory with $a_{BF} = -410 a_0$ [72, 73]. Due to the strong dependence of the critical atom number with scattering length, the onset of the collapse also provide an alternative way to determine a_{BF} using a mean-field model. Accordingly to the study reported in Refs. [72, 84], we can study numerically found the *stable* ground state of the mixture. In our model, the signature of the instability is the failure of the convergence procedure during the

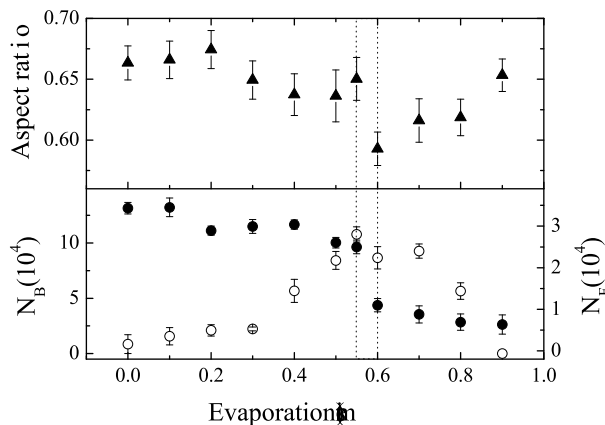


Figure 1.13: Evolution of the aspect ratio of the Fermi gas (solid triangles) and of the number of bosons (empty circles) and fermions (solid circles) at the collapse [70]. During the final stage of the bosons evaporation, the aspect ratio decreases, and suddenly drops to a much lower value after the collapse (highlighted region). The aspect ratio is measured at 5 ms of expansion and the error bars are the standard deviation of different measurements.

iterative evolution toward the ground state of the system [73]. To compare the predictions of the mean-field model to the experimental findings on the instability, we have built a stability diagram, shown in Fig. 1.12. Here we report in the plane $N_B - N_F$ the condensate and fermion atom numbers that we were able to measure in the experiment for *stable* samples, and compare them with the calculated critical line for instability for different a_{BF} around the nominal value. Note that the position of the critical line depends quite strongly on the value of a_{BF} . In the experiment we have observed the collapse of the Fermi gas for number pairs close to the two marked data points.

Finally, we have studied the aspect ratio of the Fermi gas at the occurrence of the collapse. We have observed that, after the collapse, the aspect ratio of the remaining fermions results up to 30% lower than the one expected for a pure Fermi gas and of the same order of the one measured for a stable mixture with comparable atom numbers, as reported in Fig. 1.13. Indeed, increasing N_B we first observe a small decrease of the aspect ratio followed by a jump to a lower value just in correspondence to the collapse. The aspect ratio then slowly tends to the unperturbed value as the BEC is completely evaporated. This indicates that after the collapse the system has reached a new equilibrium distribution in the same time scale of the collapse in which most of the fermions are immersed in the condensate feeling a large interspecies interaction during the expansion from the trap. This observation is somehow surprising, since

one could expect that during the collapse exactly the fermions in the high density region within the condensate are lost through inelastic processes while the remaining fermions are mostly located in the outer region. This would correspond either to a faster expansion with a larger aspect ratio, or to an oscillating Fermi gas strongly out of the equilibrium which we do not observe in the experiment.

1.4.5 On the route toward the BCS transition

As already mentioned, Fermi gases are attracting more and more interest in the community of quantum gases. This interest lies in the possibility to achieve, in such fermionic systems, a superfluid regime similar Cooper pairs in superconductor metals. The underlying physics of the usual superconductor metals is well described by the Bardeen-Cooper-Schrieffer (BCS) theory: two distinguishable electrons near the surface of the Fermi sphere are unstable against an attractive perturbation and can form a pair, the so-called Cooper pair. The same instability is expected to take place in a dilute gas of fermions at very low temperatures, typically much lower than the Fermi temperature of the system [85]. At these ultralow temperatures, collisions are strongly suppressed and the pairing can be achieved only through s-wave interaction. Since in the case of identical fermions this scattering process is inhibited, we have to consider a system composed by two different fermionic species, as, for example, the case of fermions in two different Zeeman levels. Note that the critical temperature T_{BCS} expected for Cooper pairing is typically of the order of some fraction of the Fermi temperature for the system, which is hardly achievable experimentally. Nevertheless, T_{BCS} is expected to increase exponentially by increasing the interstates s-wave scattering length a . The now well-tested method to tune the scattering length is based on the Feshbach resonances technique which consists to apply an homogeneous magnetic field which shifting the Zeeman levels [24, 86]. With this technique, one can range from negative to positive scattering length, where different physical phenomena are expected. In the limit of strong repulsive interaction, the system is unstable with respect to the formation of molecules. These molecules have been recently observed both in the normal phase and Bose condensed (BEC regime) [25, 26, 27, 28]. In the other limit i.e. in presence of a strong attractive interaction, one expect that fermions near to E_F could instead form Cooper pairs. In this case, the system behaves as an high T_C superconductor (BCS regime). Many experiments have been performed in the BCS-BEC crossover [29, 30, 31, 32, 33], and, until now, a clear and indisputable evidence of the achievement of the BCS regime has not yet been provided even if recent studies on collective excitations seem to indicate the

accomplishment of this regime [34, 35].

Another promising scheme to achieve the BCS regime is to use a Fermi-Bose mixture in which bosons induce an effective attraction between the two fermionic spin states [36, 37]. Indeed, a large boson-fermion interaction affects not only the stability of the system [70], as we have presented above, but it also play a relevant role in the mechanisms of Cooper pairing [36] by introducing an effective attractive interaction between the fermions. This is the atomic analog of phonon-induced interaction which is the underlying mechanism of superconductivity, where the coupling between two electrons is provided by the exchange of lattice phonons. Our mixture composed by ^{40}K - ^{87}Rb atoms seems particularly interesting from this point of view, due to their large fermion-boson scattering length (see Sec. 1.4.1). By using the results of [36], one can estimate the ^{40}K - ^{40}K effective interaction (a_{FBF}). At zero field, we know that the ^{40}K - ^{87}Rb scattering is $a_{BF} = -410 a_0$, the Rb-Rb is $a_{BB} = -100, a_0$. For these values, we find that the boson-induced scattering length a_{FBF} at zero-field is $\sim -1700 a_0$ [70, 37]. This value is very large compared to the "bare" repulsive interaction between Potassium atoms $a_{FF} = 174 a_0$. From the value a_{FBF} , we obtain that the critical temperature for the BCS-transition turns out to be $T_{BCS} = 0.1T_F$, which is a temperature experimentally achievable.

Chapter 2

Quantum gas in a periodic potential

Il particello...

H. O.

Recently, a great attention has been devoted to understand the general properties of a quantum gas in a periodic potential. The problem of an electron moving in a periodic potential has been exhaustively investigated in solid state physics to describe systems such as conductors or semiconductors [87]. The presence of a periodic potential strongly modifies the free-particle energy spectrum and gives the well known energy bands. The energy bands arise merely from the periodicity of the potential and the generality of this result suggests that such kind of phenomenology should also be present in ultracold atomic gases subjected to a periodic potential. For instance, the atomic gases has been successfully exploited to observe some typical solid-state phenomena such as the Wannier-stark ladders [88] and its dynamical consequence, the Bloch oscillation [89], the Zener tunneling [90] and the Rabi oscillation between Bloch bands [91].

In this Chapter we will give an overview on the basic phenomenology exhibited by a single particle into a periodic potential. The aim is to remind to the reader the single-particle behavior in order to supply the basis to understand the behavior of an atomic gas observed in our experiment and reported in the subsequent Chapters. The starting point of this Chapter is to describe the standard way to produce a periodic potential for an atomic gas (Sec.2.1). We then remind the well-known Bloch theorem for a particle in a periodic potential, and we analyze some general features of the eigenfunctions and eigenvalues of the Mathieu equation. Particular attention will be given

to the Wannier eigenfunctions and to the energy dispersion which exhibits a band structure (Sec. 2.2). In the case of a sinusoidal potential, the Schrödinger equation for our problem is known as the Mathieu equation (Sec. 2.3) which is not analytical solvable in the general case, while numerical solutions are well-known. Finally, we report on an overview of the dynamics of a particle into the lattice when subjected to an external static force (Sec. 2.4). The most spectacular phenomena is the so-called *Bloch oscillation* which corresponds to an oscillating motion of a particle when a static external force is applied.

2.1 A periodic potential for quantum gases

In the last years, ultracold atoms in an optical lattice have been the subject of intensive and rich research activities providing a straight link between two different areas of physics which are usually separated. On the one hand, cold atoms trapped by laser beams fall in the domain of atomic physics and quantum optics. On the other hand, the periodicity of the optical potential provides a strong connection with solid-state physics. Furthermore, typical solid-state effects can be investigated in such systems with the advantage that the optical lattice behaves like "perfect periodic potential". The usual imperfections of traditional crystalline materials such as impurities, missed ions or thermal vibrations (phonons) have no equivalent in the optical lattice.

In this section, we report the basic ideas for the production of a periodic potential for atomic gases using laser beams.

2.1.1 The optical lattice

The optical lattice is produced by two laser beams propagating along the z -axis in opposite direction, with a time-independent frequency ω and phase difference φ :

$$\begin{aligned}\mathbf{E}_{\rightarrow} &= \hat{\kappa}_L E_1 \cos(k_L z - \omega t) \\ \mathbf{E}_{\leftarrow} &= \hat{\kappa}_L E_2 \cos(k_L z + \omega t + \varphi),\end{aligned}\quad (2.1)$$

where $k_L = 2\pi/\lambda$ is the wave number and λ is the wavelength of the laser light.

The total intensity is given by

$$I(z, \varphi) = 2\epsilon_0 c |\mathbf{E}_{\rightarrow} + \mathbf{E}_{\leftarrow}|^2 = 2\epsilon_0 c [E_1^2 + E_2^2 + 2E_1 E_2 \cos(2kz + \varphi)]. \quad (2.2)$$

The interference term gives the spatial modulation to the intensity with nodes separated by $d = \lambda/2$. The atoms subjected to a laser field experience the dipole potential

$$U_{opt} = -\frac{1}{2} \langle \mathbf{p} \cdot \mathbf{E} \rangle, \quad (2.3)$$

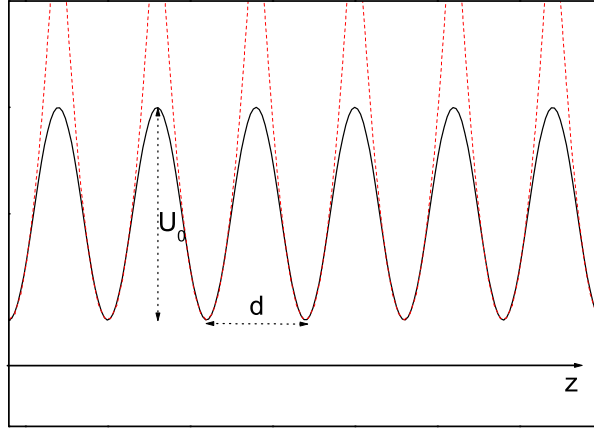


Figure 2.1: Sketch of the periodic potential experienced by the atoms. The dashed curves represent the harmonic potential in each lattice site with frequency $\omega = \hbar k_L \sqrt{s}$.

where $\mathbf{p} = \alpha \mathbf{E}$ is the electric dipole induced by the light and α is the complex polarizability. If we consider an atom as a simple oscillator subjected to a classical radiation field, Eq. (2.3) takes the form [92]

$$U_{opt} = \frac{3\pi c^2 \Gamma}{2\omega_0^3 \delta} I(z) \quad (2.4)$$

where ω_0 is the frequency of an atomic transition, Γ the spontaneous decay rate of the excited level and $\delta = \omega - \omega_0$ the laser detuning.

Another important quantity is the photon scattering rate Γ_{sc} which account for the heating of the systems:

$$\Gamma_{sc} = \frac{3\pi c^2}{2\hbar\omega_0^3} \left(\frac{\Gamma}{\delta}\right)^2 I(z). \quad (2.5)$$

Note that if the laser frequency is smaller than ω_0 (red detuning $\delta < 0$), then U_{opt} is negative and the potential minima have the maximum intensity while, above the resonance (blue detuning $\delta > 0$), the potential minima correspond to minima of intensity. Furthermore, the dipole potential scales as I/δ , whereas the scattering rate scales as I/δ^2 . The optical potential is therefore chosen with large detuning and high intensity to keep the scattering rate as low as possible for a given potential depth.

Combining Eq. (2.2) and (2.4), we finally get the periodic potential experienced by the atoms

$$U_{opt} = \frac{U_0}{2} \left[1 - \cos\left(\frac{2\pi z}{d}\right) \right]. \quad (2.6)$$

The potential depth U_0 is usually expressed in units of the single-photon recoil energy $U_0 = sE_r$ where

$$E_r = \frac{\hbar^2 k_L^2}{2m}, \quad (2.7)$$

with m the mass of the atomic species considered. In Fig. 2.1, we report a schematic representation of the optical lattice. The procedure used to calibrate such potential is reported in Appendix A.

2.2 One-Dimensional periodic potential

We now discuss some general features arising from the periodicity of the potential. In particular we will report on the Bloch theorem and on its main consequences.

2.2.1 Useful definitions

We start introducing some definitions which could be useful for the subsequent discussion.

1. **The Bravais lattice:** A fundamental concept in the description of any crystalline structure of lattice sites is the Bravais lattice which can be viewed in terms of an infinite array of discrete points with a regular arrangement and a fixed orientation. A one-dimensional Bravais lattice consists of all points with position $Z = md$, with $m \in \mathbb{N}$.
2. **The reciprocal lattice:** Consider a set of points Z constituting a Bravais lattice, and a plane wave, e^{ikz} . For general k , such plane wave will not have, of course, the periodicity of the Bravais lattice, but for certain special choices of k it will. The set of all wave vectors K that yield plane wave with the periodicity of a given Bravais lattice is known as its reciprocal lattice. Analytically, K satisfies the following relation:

$$e^{iK(z+Z)} = e^{iKz}, \quad (2.8)$$

for any z , and for all Z in the Bravais lattice. From the condition (2.8), we find $K = l\frac{2\pi}{d}$, where $l \in \mathbb{N}$.

3. **The first Brillouin zone:** The first Brillouin zone is a primitive cell of the reciprocal lattice which fills all the z -axis without overlapping when it is translated through the lattice. The Brillouin zone centered on $k = 0$, extends from $-k_B$ to k_B , where $k_B = \frac{\pi}{d}$ is usually known as Bragg momentum.

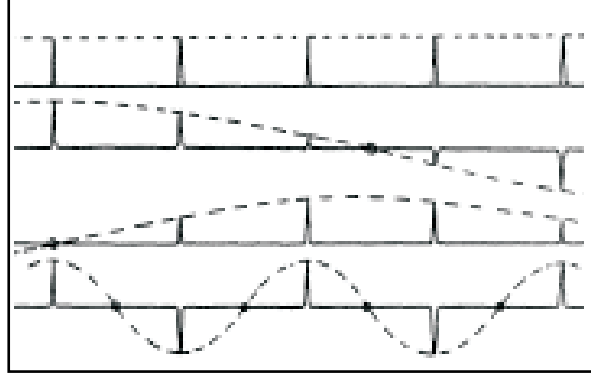


Figure 2.2: Wave functions along the periodic potential associated to different energy levels. The dashed lines are the modulating sine curves.

2.2.2 Bloch theorem

The one dimensional single-particle Hamiltonian for an atom in a periodic potential is given by:

$$\begin{cases} H_{opt} = \frac{p_z^2}{2m} + V_{opt}(z) \\ V_{opt}(z \pm md) = V_{opt}(z) \quad \forall m \in \mathbb{N} \end{cases} \quad (2.9)$$

The Hamiltonian is periodic in space, with period given by the inter-well distance d . The problem is completely solved if we find the stationary states ψ which satisfy the Schrödinger equation

$$H_{opt}\psi = E\psi. \quad (2.10)$$

As a general consequence of the periodicity of V_{opt} , the stationary solutions obey to the Bloch theorem :

Bloch theorem: the eigenstates ψ of the Hamiltonian (2.9) can be expressed as the product of a plane wave and a function with the periodicity of the lattice:

$$\psi_{n,k}(z) = e^{ikz} u_{n,k}(z) \quad (2.11)$$

where $u_{n,k}(z \pm md) = u_{n,k}(z) \quad \forall m \in \mathbb{N}$ and n is a positive integer. The Bloch theorem demonstrates that if the potential shows a periodicity then the eigenfunctions have also to exhibit a similar periodicity. There are several important and non trivial consequences arising from this theorem.

1. Bloch theorem introduce a wave vector k . With appropriate boundary condition on the wave function $\psi_{n,k}$ ¹, one can demonstrate that the vector k must

¹We can choose the Born-von Karman boundary condition: $\psi_n(z + Nd) = \psi_n(z)$, where N is

be real and represents a good quantum number for the problem. The quantity $\hbar k$ is known as the *quasimomentum* of a particle in a periodic potential which is not proportional to the particle momentum p . This is a crucial point that immediately shows the difference with respect to the free-particle case. The wave function $\psi_{n,k}$ is not an eigenstate of the momentum operator $(\hbar/i)\nabla$:

$$\frac{\hbar}{i}\nabla\psi_{n,k}(z) = \hbar k\psi_{n,k} + e^{ikz}\frac{\hbar}{i}\nabla u_{n,k}(z). \quad (2.12)$$

The k vector determines the behavior of the wave function under translation and, as we will discuss in the next section, the different meaning of k and p/\hbar involves that the system does not have completely translational invariance in the presence of a nonconstant potential.

2. Any vector of the reciprocal lattice $\tilde{k} = k + l\frac{2\pi}{d}$, with $l \in \mathbb{N}$, gives the same value of the wave function because $e^{i(k\pm l\frac{2\pi}{d})md} = e^{ikmd}$. This means that the wave vector k can always be confined in the first Brillouin zone.
3. For a given k , the Schrödinger equation (2.10) allows for an infinite family of solution with discretely spaced eigenvalues (n is a positive integer). This gives rise to the well-known band structure of the energy levels. The different eigenvalues and its corresponding eigenfunctions are labelled by the band index n . In an infinite periodic potential, each energy level $\varepsilon_n(k)$ is a continuous function of the quasimomentum k .
4. The energy dispersion $\varepsilon_n(k)$ also shows properties of periodicity

$$\varepsilon_n(k \pm l\frac{2\pi}{d}) = \varepsilon_n(k). \quad (2.13)$$

As a consequence, the full set of energy levels can be described with k restricted to the Brillouin zone without losing generality.

5. As shown in Fig. 2.2, the exponential function of the (2.11) gives a sinusoidal modulation to $\psi_{n,k}$. Note that the nodes of $\psi_{n,k}$ can occur for two different reasons: on account of those present in $u_{n,k}$ and on account of those introduced by the exponential function.

the total number of primitive cells. We find $k = \frac{m\pi}{Nd}$, with $-N \leq m \leq N$ and $m \in \mathbb{N}$. Imposing this condition, we have $2N + 1$ possible values of k .

2.2.3 Momentum eigenfunction and Wannier function

The Bloch theorem gives general properties of the eigenfunctions of Eq. 2.10. The complete knowledge of $\psi_{n,k}(z)$ can be obtained just by using a numerical approach (see. Sec. 2.3). Nevertheless we can extract some of the general properties of $\psi_{n,k}(z)$ without any computational method. From the Bloch theorem (Eq. 2.11), we know that $u_{n,k}(z)$ satisfies the following condition:

$$u_{n,k}(z \pm md) = u_{n,k}(z) \forall m \in \mathbb{N}. \quad (2.14)$$

Thus, we can express the function in term of its Fourier transform in the k -space:

$$u_{n,k_0}(z) = \sum_{k_i} f_n(k_0 + k_i) e^{\frac{i}{\hbar}(k_0+k_i)z}, \quad (2.15)$$

where the Fourier coefficients $f_n(k_0 + k_i)$ are also periodic in the reciprocal space. Note that we have different wave functions associated with the various energy bands, indicated by the label n on the u - and f -function but for each energy band, there is a single function $f(k)$ which gives complete information on all the spatial wave functions of this band. One can demonstrate that the momentum function $f(k)$ is the solution of the Schrödinger equation $Hf(k) = Ef(k)$, where the operator H is to be found from the ordinary Hamiltonian by replacing the coordinate z by $-(\hbar/2\pi i)(\partial/\partial z)$ [93].

The momentum eigenfunctions $f_n(k)$ are normalized and exists an orthogonality relation between the f -functions associated to different bands:

$$\sum_{k_i} f_m(k_0 + k_i) f_n(k_0 + k_i) = \delta_{m,n}. \quad (2.16)$$

We can easily pass from the space-eigenfunctions $u_{n,k}(z)$ to the momentum ones $v_n(k)$ using the following inverse relation to Eq. (2.15):

$$f_n(k) = \frac{1}{\Omega} \int dz u_{n,k} e^{-\frac{i}{\hbar}kz}, \quad (2.17)$$

where the integration is to be taken over a unitary cell of volume Ω , and k equals one of the vectors $k_0 + k_i$. The momentum eigenstates allows us to introduce a new function of great importance $a_n(z - z_i)$, known as the *Wannier function* [94]. As we will discuss in Chap. 4, these functions are of great utility when the translational invariance of the optical lattice is destroyed by some additional potential or impurities. Indeed, a change on the invariance properties of the system is always accompanied by the appearance of a localization. The eigenfunction relative to this

problem are usually built up from the Wannier functions (see Sec. 2.4.3). Indeed, the function $a_n(z - z_i)$ is localized in the neighborhood of the i th lattice site, in the n th band. The Wannier functions can be directly obtained by the coefficients of the Fourier-transform $f_n(k)$. Using the formula (2.15), we can also write $u_{n,k}$ in term of $a_n(z - z_i)$:

$$u_{n,k}(z) = \sqrt{\Omega} \sum_{z_i} e^{\frac{i}{\hbar} k z_i} a_n(z - z_i). \quad (2.18)$$

Equation (2.18) means that a particle in a periodic potential can be described by a combination of localized functions $a_n(z - z_i)$ in each cell, multiplied by an appropriate factor. Analogously, the Wannier function is a linear combinations of all the Bloch waves of a given band

$$a_n(z - z_i) = \frac{\sqrt{\Omega}}{\hbar^3} \int dk e^{-\frac{i}{\hbar} k z_i} u_{n,k}(z). \quad (2.19)$$

More in general, the Wannier functions obey to the following theorem [95]:

For each band exists one and only one Wannier function $a_n(z - z_i)$ which has all four of the following properties:

1. $a_n(z - z_i)$ is real.
2. $a_n(z - z_i)$ is either symmetric or antisymmetric about either $z = 0$ or $z = d/2$.
3. $a_n(z - z_i)$ is a short range function, i.e. it falls off exponentially in the z -space.
4. $a_n(z - z_i)$ and $u_{n,k}(z)$ can be expressed in term of one another.

We can conclude that the sets of Bloch and Wannier functions are two equivalent basis in the z -space. In Ref.[96], it is shown that the more practical way to find a Wannier function is to find the momentum eigenfunction $f_n(k)$ and then its Fourier transform.

2.2.4 Energy band in one dimension

The Bloch theorem tells us that the energy spectrum of a particle in a periodic potential exhibits a band structure ($\varepsilon_n(k)$ with $n \in \mathbb{N}$). The n th band is separated by the $(n+1)$ th band by an energy gap $\Delta\varepsilon_n(k)$ which depends on the band and on the quasimomentum. For low s , the band gap start to open in the neighborhood of the Bragg quasimomentum k_B and of $k = 0$. Due to the periodicity of $\varepsilon_n(k)$ in the reciprocal lattice (see Eq. (2.13)), we can solve numerically the Mathieu equation restricting our attention to the first Brillouin zone (*reduced-zone scheme*) without losing generality. The typical band spectrum, in units of the recoil energy E_r , is reported in Fig. 2.3 for different values of the lattice depth. As shown in Fig. 2.3(a), for a shallow lattice

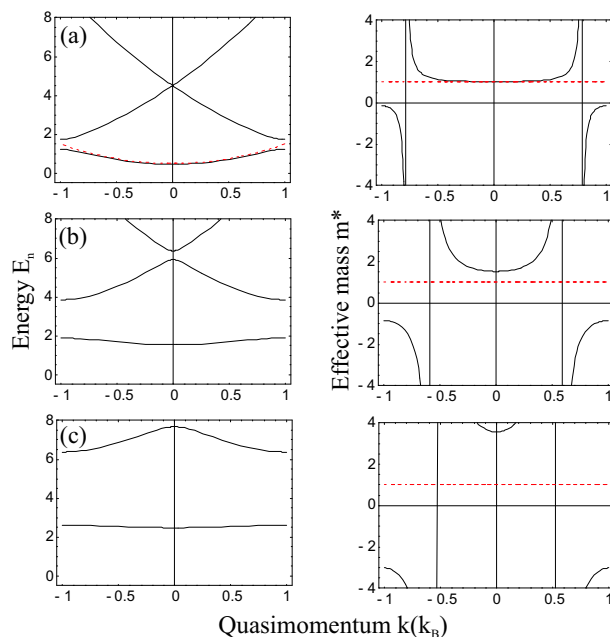


Figure 2.3: Energy dispersion $E_n(k)$ and effective mass m^* in units of E_r , for atoms in a lattice with (a) $U_0 = E_r$, (b) $U_0 = 4E_r$, and (c) $U_0 = 8E_r$.

the energy dispersion has a behavior similar to the free-electron parabola and a distortion arises only at the edge of the Brillouin zone. As we increase s , the first band becomes more and more flat straying from the free-particle case. The energy gap and the zero-point energy increases (Fig. 2.3(b-c)).

A useful quantity derived by the bands structure is the *effective mass* m^* , which is defined through the curvature of the lowest energy band ($n = 0$)

$$\frac{1}{m^*(k)} = \frac{1}{\hbar^2} \frac{\partial^2 \varepsilon(k)}{\partial k^2}. \quad (2.20)$$

Under appropriate conditions, a particle in the lattice behaves like a free particle but with its inertial properties changed by the presence of the periodic potential ($m \rightarrow m^*$). For small lattice depth the effective mass m^* approaches the bare value (Fig. 2.3(a)). Increasing the height of the periodic potential, m^* is strongly enhanced with respect to m (Fig. 2.3(b-c)) and particles with different quasimomentum will have different effective masses.

2.3 The Mathieu equation

A part from the Bloch theorem and its consequences, the numerical approach to solve the problem of a particle in an one-dimensional periodic potential is well-known. For the specific case of a sinusoidal potential, the Schrödinger equation is known as the Mathieu equation whose solutions have been extensively studied by the mathematicians [97]. The Mathieu equation

$$-\frac{\hbar^2}{2m} \frac{d^2\psi(z)}{dz^2} + \frac{U_0}{2} \left[1 - \cos\left(\frac{2\pi z}{d}\right) \right] \psi(z) = E\psi(z) \quad (2.21)$$

is numerically solvable for any U_0 . Furthermore, an analytic solution can be found in two limiting cases where approximate methods can be used providing useful information on the problem. The former is called *tight binding or atomic approximation* and it is used in the limit of a deep optical potential. In this case, the one-site wave function hardly overlap with the ones in the neighbor sites and consequently the tunneling probability through the lattice sites is small. The opposite limit is known as *weak binding or free-electron approximation* appropriate for shallow lattice: the atoms move so fast that their wave function is not far from a plane wave. In several physical situations however the atoms are described by a wave function of the type intermediate between the range of validity of these two approximations. For these cases, one has to solve numerically Eq. (2.21). An instructive way to get the physical meaning of these two approximations is to study the behavior of the energy spectrum as a function of the lattice height $U_0 = sE_r$. We write the Schrödinger equation (2.21) in term of dimensionless variables, to simplify the notation:

$$w = \frac{\pi z}{d}, \quad \epsilon = \frac{E}{E_r}. \quad (2.22)$$

In terms of these quantities, we can express (2.21) in the alternative forms

$$-\frac{d^2\psi(w)}{dw^2} + \frac{s}{2} [1 - \cos(2w)] \psi(z) = \sqrt{s\epsilon} \psi(w). \quad (2.23)$$

In Fig. 2.4 we show the widths of the energy bands ϵ of the one dimensional problem as a function of the lattice height s . For large enough values of s , the band become indefinitely narrow and the wave function in each lattice site do not overlap appreciably. The energy levels approach the harmonic oscillator limit with value ($\epsilon_n = 2n + 1$). In fact, for large s each lattice well can be approximated with an harmonic potential (see Fig. 2.1) of frequency ω defined by

$$sE_r \frac{\pi}{d} = \frac{1}{2} m \omega^2. \quad (2.24)$$

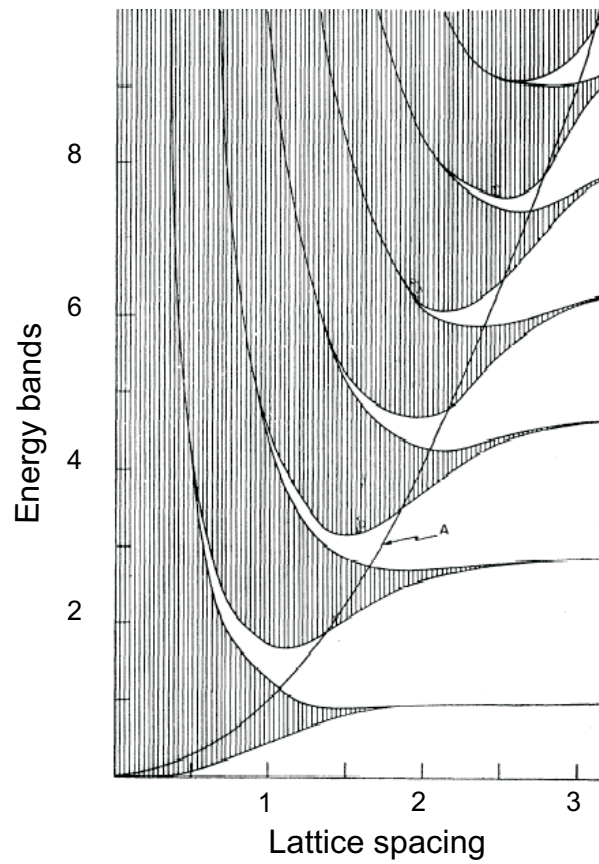


Figure 2.4: Energy band $\epsilon = E/E_r$ as a function of $s^{1/4}$ for the one dimensional Mathieu problem. The curve A represents the height of the potential barrier between the lattice sites.

As the lattice depth increases, the energy levels decrease before the broadening into bands becomes appreciable. If we write the potential as a power-law expansion then the quadric term gives the parabolic potential while the higher order of the expansion act like a perturbation to the harmonic oscillator problem. This terms are responsible for the decrease of the energy levels. As the lattice becomes more and more shallow, the energy levels begin to broaden into bigger bands and the energy gap disappears as s goes to zero.

2.4 Transport through the lattice

So far we have studied the stationary solutions of the single-particle Schrödinger equation (2.21). We now address our attention on the motion of a particle into the lattice under an external force of strength F . The evolution of such particle can be described using either a semiclassical model or a quantum-mechanical approach. In general, we know that a particle in the n th band with quasimomentum k moves in the k -space with the mean velocity [87]

$$v_n(k) = \frac{1}{\hbar} \frac{\partial \varepsilon_n(k)}{\partial k}. \quad (2.25)$$

The energy levels $\varepsilon_n(k)$ are stationary solutions of the Schrödinger equation in presence of the full periodic potential. Eq. (2.25) tells us that, in absence of external force, a particle with energy $\varepsilon_n(k)$ moves forever without any degradation of its mean velocity, if the initial mean velocity is different from zero (i.e. $k \neq 0$ and $k \neq \pm \frac{2\pi}{d}$). The collisions with a perfect lattice are not able to degrade the velocity of the particle, because the interaction with the periodic array has been fully taken into account *ab initio* in the Schrödinger equation solved by Bloch wave functions. Thus, the conductivity of the system is infinite.

In nature, electrons in crystals never behave like a perfect conductor. Metals indeed have always an electrical resistance because no real solid is a perfect crystal. In such systems, the periodic potential is produced by the ions and there are always impurities, missing ions or other imperfections that can scatter electrons even at very low temperature. In addition, also in absence of imperfections, the conductivity remains finite because of the thermal vibrations of the ions i.e. the phonons, which produce temperature-dependent distortions to the periodic potential which are able to scatter the electrons. As we will see in the next chapters, the situation is different when we deal with an atomic gas in a periodic potential produced by light. First of all, the optical lattice behaves like a perfect periodic potential where dissipative mechanisms due

to missing ions or phonons are not present. Further, the collisional properties of the atoms in the gas strongly depend on the statistical nature of such gas. For instance, an atomic Bose gas exhibits only s -wave collisions while collisions between fermions are forbidden by the Pauli principle. Note that a Fermi gas in a optical lattice satisfies all the requirements to be a perfect conductor (see Chap.3).

2.4.1 Semiclassical model and Bloch oscillation

We start to describe the simpler and more intuitive model to study the dynamics of a particle in presence of an external force. This model is known as *semiclassical model*. Clearly, the main goal of this approach is to bind the band structure defined in quasimomentum space with the transport in real space. This model is semiclassical in the sense that the external potential applied so varies slowly over the dimensions of the atomic wave packet that can be treated classically, while the periodic potential obeys to the quantum mechanic. Note that this model does not take into account possible collisional mechanism and its predictions are based on the complete knowledge of the band structure. Given the function $\varepsilon_n(k)$, the semiclassical model associates with each particle a position z , a wave vector k and a band index n . In presence of an external force F , the position, the wave vector and the band index evolve according to the following rules:

1. The band index n is a constant of the motion. This is a first approximation of the model implying that interband transitions are forbidden.
2. The time evolution of the position is described by the equation of motion

$$\dot{z} = v_n(k) = \frac{1}{\hbar} \frac{\partial \varepsilon_n(k)}{\partial k}. \quad (2.26)$$

This is the relevant equation of the semiclassical model which connect the motion in z -space with the evolution in k -space. In particular, if the particle is described as a wave packet of Bloch functions centered at k then $v_n(k)$ play the role of the group velocity of the wave packet.

The behavior of $v_{n=0}(k)$, is shown in Fig. 2.5. The velocity is linear in k just near the band minimum, it reaches a maximum value as the boundary of the Brillouin zone is approached, and then drops back down, going to zero at the zone edge. Note that the region of linearity decrease increasing U_0 and $v_0(k)$ becomes more and more flat, according to the intuitive idea that the higher is the inter-well potential the slower is the motion through the lattice. In the limit

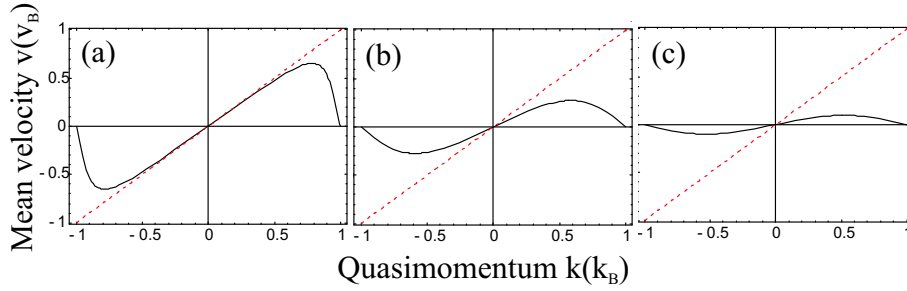


Figure 2.5: Mean velocity $v_0(k)$ in the fundamental band for different value of the lattice height (a) U_0 , (b) $U_0 = 4$, and (c) $U_0 = 8$.

$U_0 \rightarrow \infty$, the particles are completely localized in a lattice site and $v_0(k) = 0$ everywhere.

3. The model provides also the equation of motion for the wave vector k

$$\dot{k} = \frac{1}{\hbar} F(z, t). \quad (2.27)$$

Eq. (2.27) has formally the same structure as the one for free particles. However, in the latter case, the rate of change of the momentum is given by the total force acting on the particle, while for a particle in the lattice, \dot{k} depends only on the field applied externally and not on the periodic field.

Under these assumptions, the semiclassical model well describe the system response to a homogeneous and static external potential $U = Fz$ (i.e. a DC electric field for metals). In particular, an external static force F yield an oscillatory rather than uniform motion of the particles known as *Bloch oscillation*. Bloch oscillation represents the major result of the semiclassical theory.

We now derive the oscillating behavior of the particle in the framework of the semiclassical theory. The stationary Schrödinger equation (2.21) in presence of a static external force F , becomes

$$-\frac{\hbar^2}{2m} \frac{d^2 u(z)}{dz^2} + \frac{U_0}{2} \left[1 - \cos\left(\frac{2\pi z}{d}\right) \right] u(z) + Fz u(z) = E u(z). \quad (2.28)$$

We can study the evolution of the system described by Eq. (2.28) using the semiclassical model if the applied force is weak enough to not induce interband transitions i.e. one assumes that the external force behaves as a perturbation to the system which does not modify much the eigenfunctions and eigenvalues of the Hamiltonian (2.21). According to Eq. (2.27), the evolution of the quasimomentum is

$$k(t) = k(0) + \frac{Ft}{\hbar}. \quad (2.29)$$

Due to the periodicity of the systems, the quasimomentum $k(t)$ changes linearly with time until it reaches the boundary of the Bloch band (k_B) where it is Bragg reflected. The quasimomentum $k(t)$ is thus periodic in time with period $T_B = \frac{2\pi\hbar}{|F|d}$. This period, known as Bloch period corresponds to the time required to the quasimomentum to scan a full Brillouin zone. Note that also the mean velocity (2.29) exhibits an oscillatory behavior in time

$$v_n(k(t)) = v_n(k(0) + \frac{Ft}{\hbar}) \quad (2.30)$$

. This result is in striking contrast with the free-particle case, where v is proportional to k and grows linearly in time. As a consequence of Eq. (2.29), a particle prepared in a well-defined quasimomentum in the n th band will also oscillate in the z -space with an amplitude $\frac{\delta_n}{2|F|}$, where δ_n is the energy width of the n th band.

Using the tight binding approximation is possible to derive explicitly the equations of motion. In the limit of deep lattice the lowest energy band $\varepsilon(k)$ can be approximated with a simple cosine function, i.e.

$$\varepsilon(k, t) = -\frac{\delta}{2} \cos(k(t)d), \quad (2.31)$$

where δ is the width of the first band.

The cosine dispersion of the first band yields

$$v(t) = \frac{1}{\hbar} \frac{\partial \varepsilon(k)}{\partial k} = \frac{\delta d}{2\hbar} \sin(k(0)d - \omega_B t), \quad (2.32)$$

where

$$\omega_B = \frac{Fd}{\hbar} \quad (2.33)$$

is the so-called Bloch frequency. Under a static force, a particle oscillates in the real space

$$x(t) = \frac{\delta}{2F} \cos(k(0)d - \omega_B t) \quad (2.34)$$

with amplitude proportional to $1/F$. We can conclude that the linear growth of $k(t)$ and the periodicity of $\varepsilon(k)$ transform the static stimulus F into an oscillating response.

We remind that the semiclassical model does not include collisions and consequently all dissipative mechanisms that could degrade $v(k)$ and \dot{k} are absent. For instance, in metals the scattering time of the electrons with lattice defects is remarkably shorter than the time needed to k for scanning the Brillouin zone (τ_B), and the Bloch oscillations have never been observed. Recently the Bloch oscillations have been observed with electrons in semi-conductor superlattices [98], cold atoms in optical lattices [99], and light in photonic structures [100].

2.4.2 Zener tunneling

The semiclassical model well describes the dynamics of a particle into a tilted lattice, provided that interband transitions are negligible. If this is not the case then as soon as a particle reaches the edge of the Brillouin zone during its Bloch oscillation has a finite probability to be transmitted to higher bands. This phenomena is known as Zener tunneling which is a quite relevant effect when one works with an atomic gas in shallow lattice. For a fixed force acting on atoms, the interband tunneling rate depends on the lattice height. Tuning s we can indeed completely suppress the tunneling or to deplete the lattice in one Bloch period.

It could be useful to summarize now the procedure to derive the rate of Zener tunneling. In general, at each band cycle, the particles can go to occupy the higher band with a transmission rate R

$$R = \frac{\omega_B}{2\pi} |T|^2, \quad (2.35)$$

where $|T|^2$ is the transmission amplitude. In the general case this amplitude can be derived just within a numerical approach nevertheless, under appropriate approximation, it is also possible to derive an analytical expression. Since the transmission probability is maximum at the lower energy gap ΔE , we will focus at the edge of the Brillouin zone ($q = q_B$). We first require that the potential drop Fd per lattice site be small compared to the lattice depth U_{opt} . If this is not the case, the initially occupied band will be emptied on a time scale comparable to the Bloch period $T_B = 2\pi/\omega_B$, so the concept of the Bloch oscillation becomes questionable.

For sake of clarity, we rewrite the eigenvalue equation already reported in Chap. 2

$$\left(-\frac{\hbar^2}{2m} \frac{d^2}{dx^2} + V_{pot}(x) \right) \varphi(x) = (E - Fx) \varphi(x). \quad (2.36)$$

In order to derive the transmission amplitude, we have to construct approximate eigenstates $\varphi(x)$ of the biased lattice by gluing together the unperturbed Bloch states corresponding to the *local energies* $E - Fx$. This procedure, that we don't want to discuss in detail here [101], corresponds to construct a function of local wavenumber $k_n(E - Fx)$ which determines $\varphi(x)$. The individual functions $k_n(E - Fx)$ then have to be analytically connected through the band-gaps to yield one overall function $k(x)$ defined for all x . The new eigenstates, which are Bloch waves with slowly varying wavenumber, can be written as

$$\varphi(x) = \exp\left(i \int_{x_0}^x dx' k(x')\right) \tilde{u}_{k(x)}(x), \quad (2.37)$$

where x_0 is some arbitrary reference point, and $\tilde{u}_{k(x)}(x)$ is the Bloch function associated with $k(x)$.

Once the function $k(x)$ is known within a gap, we can calculate the transition amplitude from the following equation

$$|T|^2 \approx \exp\left(-2 \int dx |Imk(x)|\right), \quad (2.38)$$

where the integral is made over the gap region. At the end of this procedure we finally find an analytic expression for the transmission amplitude. In presence of the force of gravity $F = mg$, one finds

$$|T|^2 = \exp\left(-\frac{\Delta E^2 \lambda}{8\hbar^2 g}\right), \quad (2.39)$$

where ΔE is the energy gap between the ground state band and the continuum at the edge of the Brillouin zone.

2.4.3 Wannier-Stark states

In the semiclassical model, the motion of particles in the periodic potential under an external static force is investigated looking at the energy dispersion relation and no information about the eigenstates of the system is given. The static force is treated as a perturbation and the key approximation of the model lies in the substitution of the quasimomentum with the momentum of the particle. Nevertheless, also for small F , the potential Fz diverges as $|z| \rightarrow \infty$ and we can not consider Fz as a small perturbation in the usual sense: we have to deal with a *singular* perturbation. The singularity of the perturbation manifests itself in the fact that it changes the nature of the unperturbed spectrum of the Hamiltonian H_{opt} . As far as $F \rightarrow 0$, the energy spectrum is continuous. In particular, this means that the eigenstates associated are not square integrable functions, i.e. the Bloch eigenfunctions are delocalized along the whole infinite periodic potential. In a pure periodic potential, the translational invariance lets each energy level of each local lattice well to be degenerate with all other level. As a result, the eigenfunctions of a periodic system form bands of delocalized state which extend over the entire lattice. As an external force is applied, the system is no more invariant with respect to a simple translation in the z -space and the degeneracy of the energy levels is somehow removed. If T_d is the translation operator ($z \rightarrow z + d$) and H_F the biased Hamiltonian

$$H_F = H_{opt} + Fz, \quad (2.40)$$

we find that the commutation relation is not zero

$$[H_F, T_d] = F d T_d. \quad (2.41)$$

However, Wannier has demonstrated that also in the presence of a static force, the system preserves a periodicity in the following sense [102]:

Wannier Theorem: If a solution of the one-electron Schrödinger equation in a periodic potential and a static force exists for some energy E , then the wave function $\psi_E(z)$ satisfies

$$\psi_E(z) = \psi_{E+Fd}(z + d). \quad (2.42)$$

Thus, the system is invariant for a appropriate combined translation in the energy and z -space. In the one-band model, the existence and the uniqueness of E is guaranteed. Eq. (2.42) leads to the so-called *Wannier-Stark ladders*: under the influence of an external potential Fz , each unperturbed energy band split into a sequence of resonances equally spaced in energy

$$E_{n,j}(k) = \varepsilon_n(k) + jFd, \quad (2.43)$$

with $j \in \mathbb{N}$.

The single-particle states associated to the ladder structure are localized functions, known as the *Wannier-Stark functions*. We have to emphasize that the existence of these Wannier-Stark ladders is quite a subtle problem which has been debated over a period of almost three decades [103]. If one neglects the transition between different zero-field bands, it is possible to show that the stationary problem with the Hamiltonian (2.40) admits for Wannier-Stark ladders as eigenvalues and the corresponding eigenfunctions are the localized Wannier-Stark states. The real controversial point is whether the Wannier-Stark ladders survive with the inclusion of the interband transition². The doubt is well founded since a particle moving in the lowest band experiences a periodically varying energy separation from the first excited band and comes closest to it at the edges of the Brillouin zone where it could perform Zener tunneling. Indeed, when the particle knocks at the higher band (once per Bloch cycle) is partially transmitted with a transmission amplitude T , already reported in Eq. (2.39). As we will show in Sec. 3.3.1, this problem is particularly relevant in atomic Fermi gases. For instance, if the Fermi energy E_F lies in the band gap, several fermions occupy states close to the band-edge and could tunnel in higher bands. From a mathematical point of view, the bands are thus not exactly decoupled, and the Wannier-Stark ladders have to be understood as well-defined *resonances* i.e. long-lived states of the system, rather than eigenvalue of the Hamiltonian H_F .

The Wannier-Stark state $\psi(k)$ are immediately found solving the Schrödinger equation in the quasimomentum space within the one-band approximation (we skip the

²The survival of the ladder structure has been questioned in several works [104].

band index n):

$$\left[\varepsilon(k) + iF \frac{d}{dk} \right] \psi(k) = E(k) \psi(k), \quad (2.44)$$

where $\varepsilon(k)$ is the eigenvalue of the Hamiltonian H_{opt} corresponding to the fundamental band. Solving Eq. (2.44) for the eigenstates which are periodic in the k -space, with period $2\pi/d$, one directly found the quantized Wannier-Stark ladders:

$$E_j = \int_{-b/2}^{b/2} \varepsilon(k) dk + jFd \quad (2.45)$$

To derive explicitly the eigenfunction and the eigenvalues of the problem we need to know the unperturbed energy dispersion of the first band, $\varepsilon(k)$. In the tight binding regime, $\varepsilon(k)$ is a cosine function of the quasimomentum (Eq. (2.31)) and the Schrödinger equation can be written

$$\left[-\frac{\delta}{2} \cos(kd) + iF \frac{d}{dk} \right] \psi(k) = E(k) \psi(k). \quad (2.46)$$

The Wannier-Stark state $\psi_j(k)$ are found by integration the Schrödinger equation which is a first-order differential equation

$$\psi_j(k) = \sqrt{\frac{d}{2\pi}} e^{-i[jkd + \gamma \sin(kd)]}, \quad (2.47)$$

with $j \in \mathbb{N}$ and $\gamma = \delta/2dF$. We note that the equation of motion for $k(t)$ (Eq. (2.29)) can also be derived applying the time evolution operator to the Wannier-Stark function (2.47) [105].

We want just to mention here that is possible to derive the Wannier-Stark function in the z -space by a linear combination of Wannier state $a(z - z_i)$ (see Sec. 2.2.3) with the Bessel function $J_{i-j}(\gamma)$ as coefficients

$$\psi_j(z - z_j) = \sum_i J_{i-j}(\gamma) a(z - z_i). \quad (2.48)$$

From the properties of the Bessel function, we know that $J_{i-j}(\gamma)$ is mainly localized in the interval $|i - j| < \gamma$ and consequently the Wannier-Stark states extend over an interval $L = \delta/F$. Outside this interval, the Bessel functions decay as $J_i(\gamma) \sim \gamma^i$. In Chapter 3, we will show that a fermion in a tilted lattice belongs in a superposition of Wannier-Stark states whose extension set the degree of localization of the particle. We just recall that the Wannier-Stark functions have already been used in solid state physics to discuss spatial localization of particles. For instance, these functions have been chosen to describe the localization due to attractive impurities that bind an

electron or magnetic phenomena with localized magnetic moment, and, in general, they are useful to derive the motion of particles when the semiclassical theory of the transport of Bloch particles breaks down.

Chapter 3

Fermi gas in a vertical lattice

*Attenta agli obiettivi. Tra un obiettivo
ed un altro ci passa la vita.*

C. T.

As discussed in Chap.2, an external static stimulus yields to a periodic motion of a particle through the first energy band, known as Bloch oscillation. This prediction arises from a theory of single-particle in which the lattice is considered to be *perfect* and no dissipative mechanisms are present. The scenario can change notably when we deal with real physical systems such as metals. For instance, Bloch oscillations are never been observed in usual metals because of the high collisional rate of electrons with phonons or crystal impurities. Indeed, in such system the scattering time τ is much shorter with respect to the Bloch period T_B and an electron moving in a band is back-scattered without reaching the edge of the Brillouin zone. In the field of dilute ultracold atomic gases the typical scattering times involved are much larger with respect to the ones encountered in solids. In particular the collisional time turns out to be longer than the Bloch period T_B ($\tau \gtrsim T_B$) and phenomena as Bloch oscillation and Zener tunneling can be observed. So far this kind of study has been performed in a gas of thermal atoms [99] and a Bose-Einstein condensate [42]. However, collisions are still present in both systems reducing the observation time of these effects.

3.1 Outline

In this Chapter, we report our experimental observation of Bloch oscillation (Sec. 3.4) and Zener tunneling (Sec. 3.3) in a Fermi gas trapped in a vertical optical lattice under the influence of gravity (Sec. 3.2). The interest of such extension lies in the fact that

a Fermi gas in an optical lattice is the first system completely free from interactions which can be produced experimentally [48]. Indeed, in addition to the suppression of collisions between fermions, an optical lattice is a perfect periodic potential in which lattice phonons or impurities are absent. As a consequence, a Fermi gas in a lattice performs a Bloch oscillation under the influence of the gravity which could, in principle, persist forever. In our experimental apparatus, we are able to observe Bloch oscillation of fermions on a time scale which is one order of magnitude bigger than the one found for an interacting Bose-Einstein condensate (Sec. 3.4). Indeed, interaction between atoms dramatically affects an interferometric measurement, giving rise to a shift or decay of the signal. The comparison between the behavior of these two systems proves the superiority of non-interacting fermions with respect to condensed bosons, which is somehow a counterintuitive result. Furthermore, from a quantum mechanical point of view, Bloch oscillation arises from the single-particle interference between the eigenstates of the tilted lattice (Sec. 3.5) and this equivalence offers us the possibility to exploit the long-lived Bloch oscillations as an interferometric scheme to measure forces with microscopic spatial resolution. In particular, we adopt this scheme to get a sensitive determination of the acceleration of gravity (Sec. 3.6). The main results reported in this Chapter can be found in our recent publication:

- *"Atom interferometry with trapped Fermi gases", G. Roati, E. de Mirandes, F. Ferlaino, H. Ott, G. Modugno, and M. Inguscio, accepted in Phys. Rev. Lett., cond-mat 0402328 (2004).*

3.2 Production of an atomic Fermi gas in a vertical lattice

We now describe our procedure to load a degenerate Fermi gas in an optical lattice vertically aligned. We employ a fermionic sample of ^{40}K atoms which are brought to quantum degeneracy ($T < T_F$) using the technique of sympathetic cooling, already described in Sec. 1.3. In particular, during the last stage of cooling, the Fermi gas is held together with a Bose gas of ^{87}Rb in a cigar-shaped harmonic trap. We then perform an evaporative cooling on bosons which also leads to a cooling of fermions via interspecies elastic collisions. To produce a pure Fermi gas, we completely remove bosons from the trap by means of a rf-knife which transfers the bosons in untrapped Zeeman sublevels. At the end of this procedure, we obtain a pure Fermi gas of about 3×10^4 atoms spin-polarized in the $F=9/2$, $m_F=9/2$ state. Typical temperature reached is $T=0.3 T_F$, where $T_F=330$ nK is the Fermi temperature. We then switch on adiabatically an optical lattice which is aligned along the vertical direc-

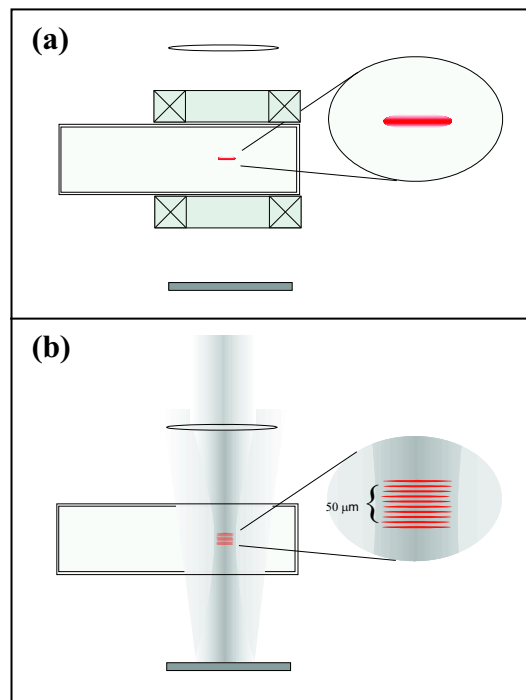


Figure 3.1: Schematic setup of the experiment. (a) Initially the atomic cloud is magnetically trapped in the second cell and exhibits a cigar shape typical of a cylindrical harmonic confinement. (b) We then superimpose a counter-propagating red-detuned laser beam along the vertical direction. Atoms arrange themselves in a regular lattice of pancake-like atomic subensembles.

tion (axial), as schematized in Fig. 3.1. Our one-dimensional lattice is created by a retroreflected laser beam in standing-wave configuration. The incoming beam and the reflected one interfere each other giving rise to a spatial modulation of the laser intensity with nodes separated by $d = \lambda/2$. The vertical lattice experienced by the atoms is then

$$U_{opt}(z) = \frac{U_0}{2} \left[1 - \cos \left(\frac{2\pi z}{d} \right) \right]. \quad (3.1)$$

The radial confinement is instead provided by the gaussian profile of the laser beams in this direction. The atoms are thus subjected to the following total potential

$$U_L(z, r) = U_{opt}(z) e^{-\frac{r^2}{w^2}}, \quad (3.2)$$

where w is the beam waist of the laser beam.

Using different intensities for the two beams we obtain a radial trap depth of about $10 E_R$, with a typical trapping frequency of $2\pi \times 30 \text{ s}^{-1}$.

We choose a laser wavelength far detuned to the red of the optical atomic transitions ($\lambda=873 \text{ nm}$) to avoid photon scattering which leads to a heating of the sample. In a red-detuned lattice, atoms are axially confined in the antinodes of the standing-wave, resulting in a regular one-dimensional lattice of pancake-like atomic subensembles. We adjust the depth of the potential in the range $U=1-4 E_R$, where E_R is the recoil energy

$$E_R = h^2/2m\lambda^2. \quad (3.3)$$

For our parameters, the recoil energy $E_R = k_B \times 310 \text{ nK}$. Note that E_R turns to be similar to the Fermi energy, which is the other fundamental energy scale of our system. Since $E_R \simeq E_F$, the atoms are loaded mostly in the first Bloch band of the lattice. From an experimental point of view, the calibration of the lattice constitutes an important and ticklish question since most of the measurable quantities depend on the lattice depth. A precise tool to measure the effective optical potential is provided by Bragg diffraction of atoms from a grating of laser light. This calibration procedure is described in Appendix A.

3.3 Bloch oscillations and Zener tunneling

As already mentioned in Sec. 2.4, when subjected to a static external force, a particle can cycle through the first band experiencing a periodically varying energy separation from the first excited band. The energy separation has its minima at the edge of the Brillouin zone ($q_B = 2\pi/\lambda$). At q_B , the particle has a finite probability to be Bragg

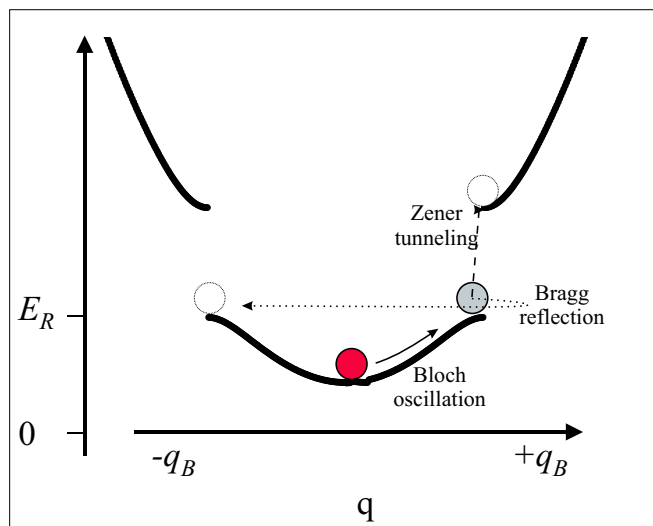


Figure 3.2: Scheme of the typical single-particle dynamics in a tilted lattice. A particle performing Bloch oscillation in the lowest band can be either Bragg reflected or transmitted via Zener tunneling when the edge of the Brillouin zone is approached.

reflected and a finite one to be transmitted in the second band, as we have schematized in Fig. 3.2. When reflected, the particle continues to scan periodically the first Brillouin zone giving rise to an oscillation in both the quasi-momentum and the position space at the Bloch frequency $\omega_B = mg\lambda/2\hbar$. Particle performing interband transition, goes instead to occupy the first excited band and hardly feels the periodic potential. As a consequence, it escapes from the lattice and can freely expand. Dealing with a gas of particles, we will observe a finite fraction of atoms which oscillates in the fundamental band and a fraction which performs interband transition. This transition to higher bands is known as Zener tunneling and has already been observed using a Bose-Einstein condensate by Kasevich group [42] while Bloch oscillations have been detected in a gas of thermal atoms by Salomon and coworkers [99]. It is important to stress that Bloch oscillations and Zener tunneling arise from the single-particle coherence in the lattice, the extension to a cloud of atoms obliges also to introduce inter-particle interaction effects which could in principle affect the observability of such phenomena. For instance, condensed atoms arrange themselves in a narrow distribution in the quasi-momentum space and the single-particle picture seems to be preserved. Nevertheless bosons interact each other during the motion into the band and the observed behavior can substantially stray from the single-particle one described in Chap. 2. One of the purposes of our experiment is to understand how

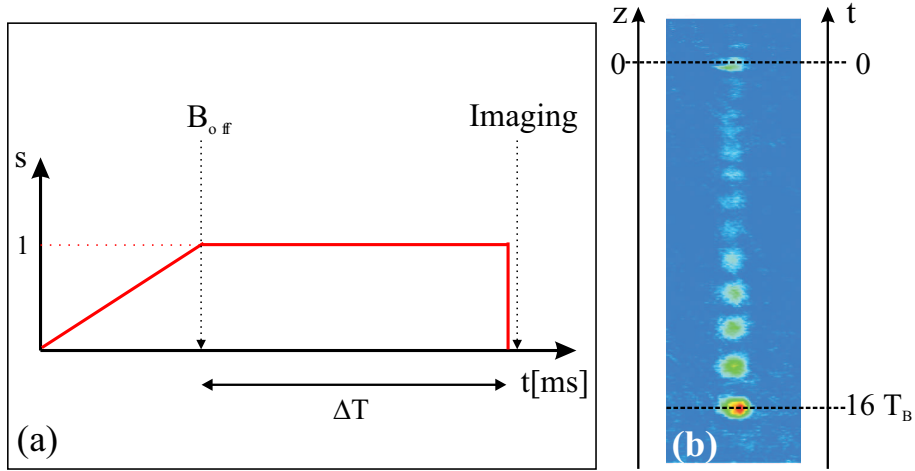


Figure 3.3: Zener tunneling of a Bose-Einstein condensate induced by the gravity. (a) Scheme of the experimental procedure to load the atoms into the vertical lattice. (b) Absorption image of the condensate after 18 ms of expansion at $s = 1$. Bosons performing interband transition escape from the confining lattice and evolve following a ballistic expansion. Notice that, after 18 ms of expansion, atoms trapped into the lattice are still present (atoms in $z=0$).

the interactions affect the dynamics of particles loaded into the optical lattice. Our experiment allows us to tune the interaction between particles since we can produce independently a Bose-Einstein condensate, a gas of identical fermions or a mixture of these two species. In brief, exploiting the versatility of our apparatus, we have the unique possibility to range from an interacting gas (Bose-Einstein condensate or Bose-Fermi mixture) to an ideal gas (Fermi gas) and thus to investigate transport phenomena reaching collisional regime which are not accessible in solid state physics.

3.3.1 Zener tunneling

Particles trapped in the first band start to scan periodically the band with a Bloch frequency ω_B as soon as a linear force is applied. The dynamical behavior of the system can be described both in semiclassical approximation and using a quantum mechanical description based on Wannier-Stark function (see Sec.2.4.1-2.4.3, respectively). However, if the band gap ΔE is smaller compared to the external potential applied we are in the Zener tunneling regime: atoms can "jump" into higher bands. In this case, the two single-band descriptions are no more valid. Indeed, one needs to take into account both particles in the higher band and the depletion of the initial level. In Sec. 2.4.2, we have shown that the population of the first band decreases exponen-

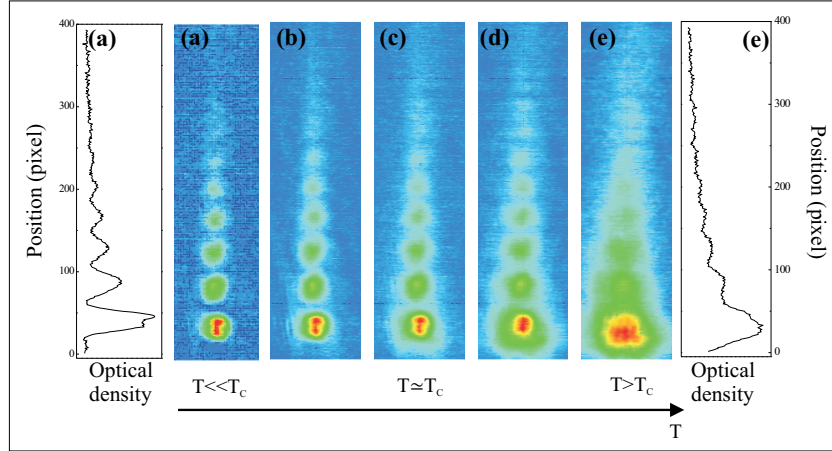


Figure 3.4: Zener tunneling of a Bose time for increasing temperatures. (a) At $T \ll T_c$, the atoms are Bose condensed providing highest visibility the effect of the different matter-pulses. (b-e) If we increase the temperature up to $T \gg T_c$ the train of pulses is still present although the contrast tends to zero with the temperature. (e) For $T \gg T_c$ the different pulse are no more well-distinguishable.

tially with time. In the semiclassical picture, particles scanning the lower band can be partially transmitted into higher band as the edge of the Brillouin zone is reached. In this sense, the atomic gas acts as a matter laser, emitting one pulse of matter per Bloch period.

To investigate the Zener tunneling regime, we choose a lattice depth which satisfy the condition $\Delta E \lesssim dm g$, where $d = \lambda/2$ and m the mass. The experimental procedure is schematized in Fig. 3.3(a). We adiabatically ramp up the vertical lattice (over 50 ms) while the magnetic confinement is switched off. Note that the adiabatic switching on of the lattice assures that atoms populate the bottom of the fundamental band with a well defined quasi-momentum k . The atoms are therefore trapped in a pure vertical periodic potential and experience a constant force provided by the gravity. The particles start to oscillate in the lower band at the Bloch frequency ω_B and we detect the fraction of atoms escaping from the lattice as soon as the Bragg quasi-momentum is reached. In Fig. 3.3, we report the observation of Zener tunneling of a Bose gas well below the critical temperature T_C . Each atom-pulse corresponds to bosons escaping from the lattice at one Bloch cycle. Indeed, the excited energy levels consist of a continuum of bands: excited particles are no more trapped by the lattice and thus start to expand ballistically. It seems clear that Zener tunneling gives an alternative evidence of Bloch oscillations in term of out-coupled atoms arranged as atom-pulses. Since the gas is loaded into the minimum of the first band, i.e. the atomic distribution

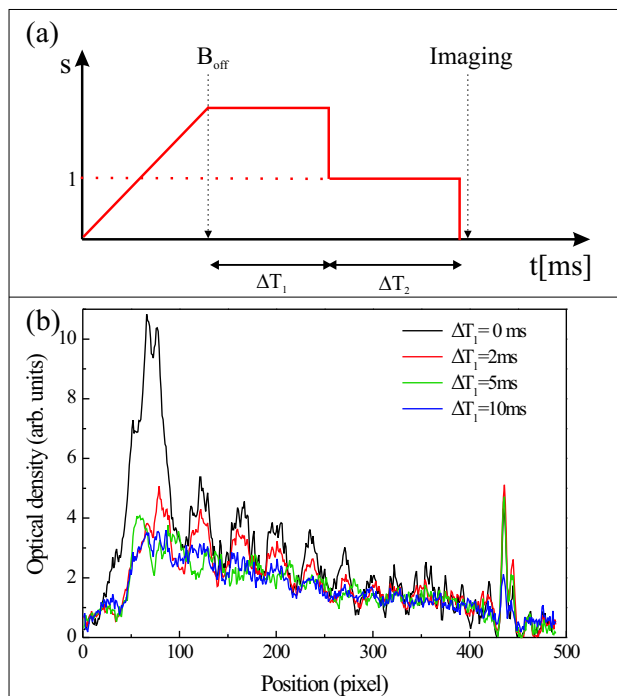


Figure 3.5: Study of the Zener tunneling of a BEC as a function of the interatomic-interaction time in the lattice. (a) Scheme of the experimental procedure. (b) Optical density of the train of pulses for different holding time Δ_1 .

is centered around the zero quasi-momentum, one can exploit Zener tunneling to estimate the Bloch period T_B which correspond to the delay time between two pulses¹. Note that for $s = 1$, we are able to produce a train of about 15-16 pulses before the initially trapped population was depleted. The observation time is then limited affecting the accuracy on T_B . As we will discuss in Sec. 3.4, in the case of fermions, a better estimate of the period is obtained to studying directly Bloch oscillations of trapped particles in the time-domain.

Note that the size of each pulse gives a signature of the mean field interaction between bosons (see Fig. 3.3). Although the distribution of the trapped sample is very narrow in quasi-momentum, during the first stage of the expansion the boson-boson interaction is rapidly converted into kinetic energy giving rise to a larger momentum distribution of the expanding pulses. Note that an increase of temperature, on the one hand leads to a small mean field interaction between the atoms but on the other the

¹By measuring the spatial separation between two subsequent atom-pulses, we can directly obtain the period of the Bloch oscillation in trap

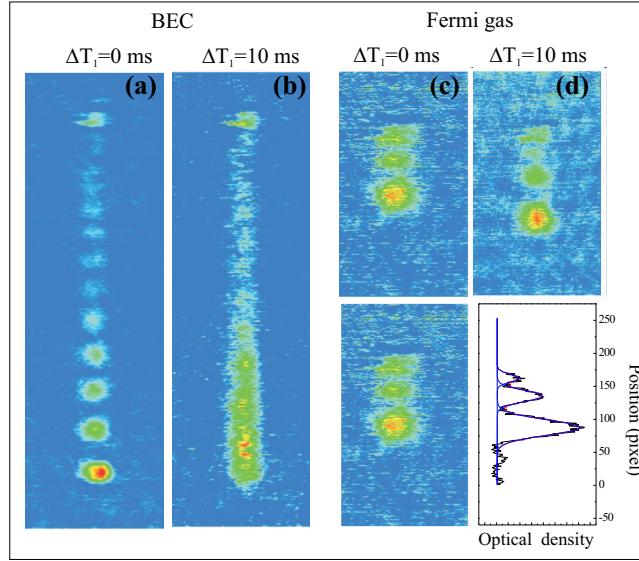


Figure 3.6: Atoms performing Zener tunneling for different holding time in the vertical lattice. The measurements are performed on a bosonic sample at $T < T_C$ (a)-(b), and using a Fermi gas at $T > T_F$ (c)-(d).

number of quasi-momentum states occupied in the band increases. In Fig. 3.4, we study the behavior of atoms performing Zener tunneling as a function of the temperature. We find that atom-pulses continue to be detectable also a temperature higher than T_C . However the contrast of the signal decreases increasing T since the spread of the momentum distribution of atoms in trap Δq is approaching $2q_B$. As $\Delta q > 2q_B$, the bosons flow continuously out of the lattice and the pulses are no more observable. Note that the survival of Bloch oscillations also for $T > T_C$ demonstrates that such phenomena arise just from single-particle coherence and no macroscopic coherence is required. Condensate properties are needed only to get a better visibility of the effect. Our observation removes the ambiguity introduced in [42] by the twofold interpretation given in term of both Bloch and Josephson a.c. oscillations.

Another important point is related to the boson-boson interaction which could somehow deteriorate the brightness of our atomic source. To investigate the role of the interactions, we have repeated the measurement reported in Fig. 3.3(a), letting now the condensed atoms to interact for a longer time (ΔT_1). The experimental procedure is shown in Fig. 3.5(a). We now rise up the optical lattice to a value larger than before to suppress Zener tunneling. We leave the atoms in such deep potential for a time ΔT_1 . During this time, bosons can cycle through the band and collide each other. We then decrease the lattice depth to a sufficiently low value to have a high probability of in-

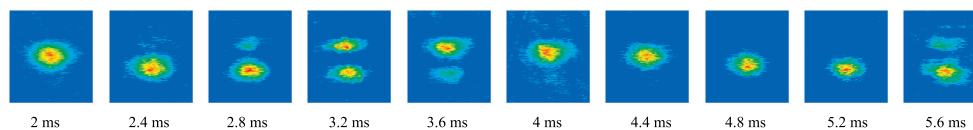


Figure 3.7: Evolution of the interference pattern of the Fermi gas for increasing holding times in the vertical lattice. The spatial distribution of the cloud detected after 8 ms of free expansion reflects the momentum distribution in the trap at the time of release.

terband transition ($s = 1$). We observe the atoms escaping by suddenly switching off the lattice, and we take an absorption image after 8 ms. In Fig. 3.5(b), we report the optical density of the matter-pulse train for different interaction times ($\Delta T_1 = 0 - 10$ ms). We find that the visibility of the pulses washes out rapidly increasing ΔT_1 . This corresponds to a decoherence of Bloch oscillations. The decay is even more clear looking at the absorption image of Fig. 3.6(a)-(b). After just 10 ms, the output signal consists of a continuum overflow of atoms from the lattice (Fig. 3.6(b)) and the pulsed behavior (Fig. 3.6(a)) is completely destroyed. This seems to indicate that, during this 10 ms, boson-boson collisions change the momentum of particles giving rise to a spread of the distribution in trap which corresponds to a band nearly filled. In other words, the mean field interaction between bosons modifies the chemical potential of atoms in each lattice site by an amount which depends on the position breaking the translation symmetry of the system and leading to a dephased output. Note that the decay of Bloch oscillations are not accompanied to an heating to the system. In fact, the radial size of the atom distribution of Fig. 3.6(b) is comparable to the one of atom pulse in Fig. 3.6(a).

As shown in Fig. 3.6(c-d), the behavior is completely different if we deal with fermions. Due their non-interacting nature, fermions are completely insensitive to the time spent in the lattice. Indeed, after 10 ms, we find the same space-resolved matter pulses of $\Delta T_1 = 0$ ms. As we will see in the next section, this result suggests a longer survival of the Bloch oscillations in trap.

3.4 Bloch oscillations of a Fermi gas

This section is devoted to the study of a Fermi gas in a tilted potential when the Landau-Zener tunneling is negligible and one can use the single-band approximation. Under this condition, we have observed time-resolved Bloch oscillations of the Fermi gas.

We start with a brief description of the procedure adopted in our experiment. The

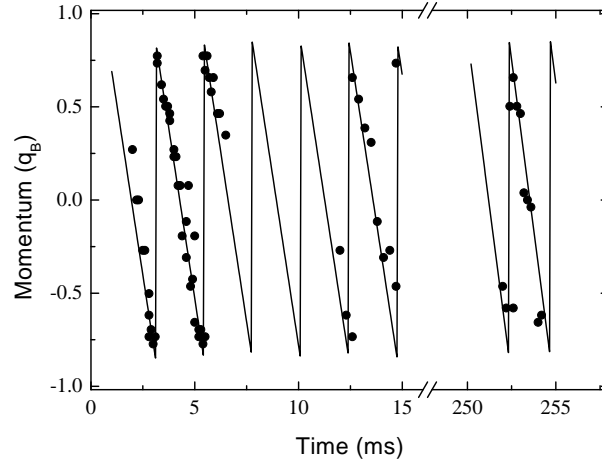


Figure 3.8: Bloch oscillation of the Fermi gas driven by gravity: the peak of the momentum distribution of the sample scans periodically the first Brillouin zone of the lattice. More than 100 oscillations can be followed with large contrast.

fermions are trapped in the vertical lattice against the gravity. The lattice power is risen up adiabatically in 50 ms. We then let the fermions to evolve in such potential for a variable holding time. The lattice depth is then lowered to zero in about $50 \mu\text{s}$, a time scale longer than the oscillation period of the atoms in each lattice well. The adiabatic release allows to study the evolution of the momentum in the first Brillouin zone. Finally, we probe the cloud by absorption imaging after a 8-ms ballistic expansion, which maps the initial momentum distribution into a position distribution. Fig. 3.7 shows the time-evolution in q space detected in the experiment which corresponds to the Bloch oscillations of the Fermi gas. Indeed, we can clearly see the vertical motion of the peak of the distribution which is initially centered in $q=0$ at $t=2$ ms. It gradually disappears as it reaches the lower edge of the Brillouin zone at $t=2.8$ ms, while a second peak builds up at the upper edge and then scans the whole Brillouin zone as the first one. This behavior is completely in agreement with the semiclassical idea of an atomic cloud that moves uniformly in q space under the influence of the gravity and is gradually Bragg reflected each time it reaches the band edge. Indeed, the periodicity of the effect amounts to about 2.3 ms, in agreement with the expected $T_B=2h/mg\lambda$. Note that we use a tighter lattice with respect to the one used for the previous measurements to avoid Zener tunneling to higher band. This also allows us to keep the atoms oscillating in the lattice for a very long times. If we follow the vertical position of the peak of the distribution in Fig. 3.7, we get the periodic motion shown in Fig. 3.8, which has the peculiar sawtooth shape expected

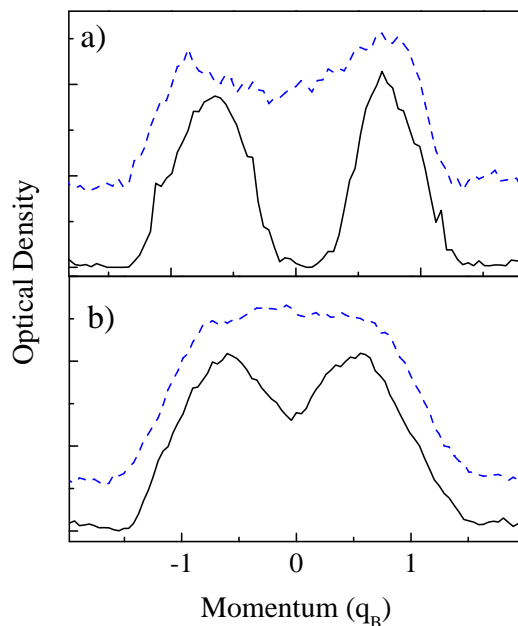


Figure 3.9: a) Momentum distribution of fermions at two different holding times in the lattice: 1 ms (continuous line) and 252 ms (dashed line). b) Momentum distribution of bosons at 0.6 ms (continuous line) and 3.8 ms (dashed line). The much faster broadening for bosons is due to the presence of interactions.

for Bloch oscillations. We can follow the oscillations for more than 250 ms, that correspond to about 110 Bloch periods, and only at later times the contrast is degraded by a broadening of the momentum distribution. This is to our knowledge the longest lived Bloch oscillator observed so far in all kinds of physical systems.

Note that for our parameters ($E_F \approx E_R$) the initial halfwidth of the wavepacket is $\delta q \approx 0.75q_B$, which fulfills the requirement of a momentum distribution narrower than the first Brillouin zone of the lattice to observe the interference. During Bloch oscillations the distribution broadens steadily and eventually fills completely the first Brillouin zone. The reduction of contrast is illustrated in Fig. 3.9a.

3.4.1 Bosons vs fermions: decoherence of Bloch oscillation

The long-lived Bloch oscillation observed with a Fermi gas is somehow a surprising result because, due to the Fermi statistic, the atoms occupy several quasi-momentum state and their large distribution could in principle affect the visibility of such oscillations. One can thus expect to get a benefit from the brightness of a BEC source in the observation such kind of effects. However, the coherence properties of a condensate

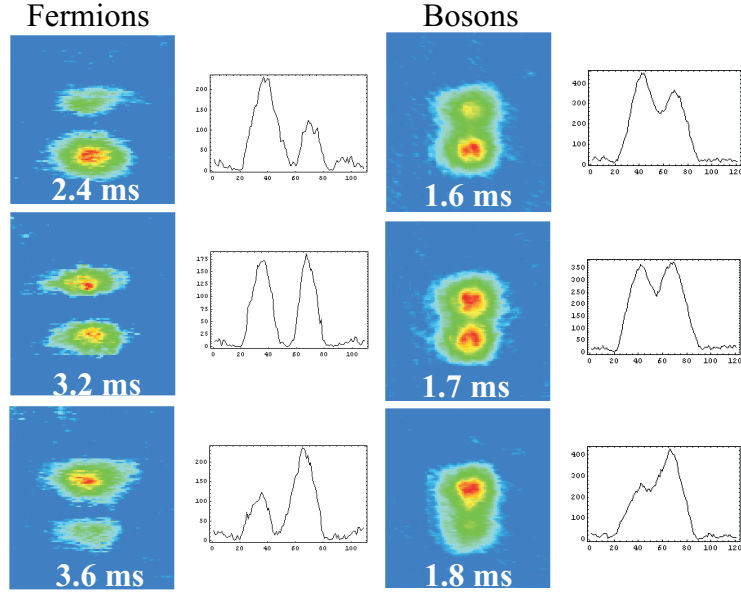


Figure 3.10: Comparison between the momentum distribution of fermions and bosons at different holding time in the lattice. We also report the respective optical density of the interference peaks.

have not to deceive the reader. Despite to their narrow distribution in momentum space, condensed atoms interact each other. The interparticle potential introduces a decoherence time which can affect the single-particle phenomena under investigation. As we have already discussed in Sec. 3.3.1, the pulsed behavior of bosons performing Zener tunneling is completely destroyed as soon as we let the atoms to interact for a longer time. It is therefore interesting to compare the behavior of fermions and bosons which perform Bloch oscillation in trap. As already noticed, the versatility of our apparatus allow us to simply repeat the experiment with a BEC of rubidium atoms. We use a sample of typically 5×10^4 atoms, at temperatures $T < 0.6 T_c$. The condensed bosons are transferred into the lattice with the same procedure used for the Fermi gas and described in Sec. 3.4. The lattice depth is in the range $2-4 E_R$, where the recoil energy for rubidium parameters is $E_R = k_B \times 150$ nK. As expected, the general phenomenology that we observe is analogous to that found for fermions: bosons perform a Bloch oscillation with a period which is now $T_B \approx 1.2$ ms i.e. nearly half of the one measured for fermions in accordance to the different mass of the two atomic species. Nevertheless two striking differences appear, as shown in Fig. 3.9b-3.10. First of all, at very short times the width of the momentum distribution of the BEC is comparable to q_B and therefore even larger than one exhibits by fermions. This

result may seem in contrast with the expectation of a much narrower momentum distribution for the BEC. In reality, we detect the atomic cloud at fixed time after the release from the lattice. During the early stage of the expansion, the boson-boson interaction energy is rapidly converted into kinetic energy giving rise to a faster expansion with respect to the case of non interacting particle. As a consequence the momentum distribution detected after a time-of-flight ($t_{exp} = 8$ ms) is much larger than the one detectable in trap. Furthermore, the evolution of bosons is also affected by interparticle interactions whereas they are trapped in the lattice. On the one hand, interactions spread the atomic distribution in trap, and on the other hand can carry the condensate in regions of instability. Indeed, as soon as the external force drives the system far from the "parabolic" region of the band, non-linear effects could arise eventually destroying the visibility of Bloch oscillations. Note that we have observed a similar degradation of the signal in the Zener tunneling experiments performed on a condensate. Such kind of phenomena has already been observed in presence of gravity [106] and in combination with magnetic traps [127]. In our experiment, we detect the decay of Bloch oscillation as a very rapid broadening of the momentum distribution, which tends to wash out the visibility of the incoming and reflected peak. As shown in Fig. 3.9, in a lattice with depth $U=2E_R$, the momentum distribution fills completely the Brillouin zone after typically 4 ms. We have checked that the decay time for the contrast gets shorter with an increasing lattice depth and radial confinement, as expected because of the larger density of the sample and thus an higher interatomic interaction. The longest decay time measured for condensed bosons is of about 10 ms, with a lattice depth of $1.5E_R$ and an almost absent radial confinement. For this low lattice height we can no more neglect the Zener tunnelling which reduce the lifetime of trapped atoms to a timescale comparable to the decay time of the contrast.

We have also repeated the experiment with a cold but uncondensed cloud of bosons at $T \approx 250$ nK. Due to the low density of bosonic thermal samples, the interatomic interaction are reduced with respect to the case of BEC. We again observe a steady broadening of the distribution. In this case the contrast degrades on a longer timescale of about 10 ms, which is still much shorter than the one observed for fermion. This comparison proves the superiority of noninteracting fermions with respect to bosons to observe single-particle effects.

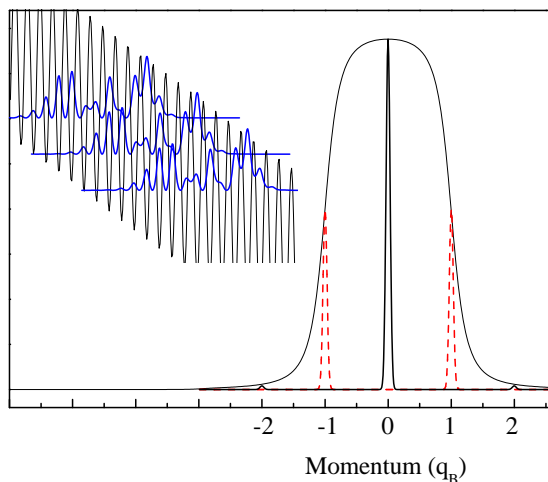


Figure 3.11: Momentum distribution of a coherent superposition of Wannier-Stark states. Although the single state fills completely the first Brillouin zone (thin line), the interference of several states gives narrow momentum peaks. Shown are the cases of a phase difference between successive states of $\Delta\phi=0$ (continuous line) and $\Delta\phi=\pi$ (dashed line). The inset shows the square of Wannier-Stark wavefunctions calculated for ^{40}K atoms in a lattice with $U=2E_R$ subjected to gravity (for clarity, the states shown are separated by four lattice sites).

3.5 Interference between Wannier-Stark states

In Chap. 2 we have shown that a particle in a lattice tilted by a homogeneous potential $U = Fz$ can be described by using both a semiclassical picture and the quantum mechanical formalism based on Wannier-Stark states. As we know, in the semiclassical approach, a particle evolves in the tilted potential performing a Bloch oscillation in momentum space (see Sec. 3.4-2.4.1). In the quantum mechanical approach, the particle is instead described by a superposition of Wannier-Stark states. This superposition yields to interference peaks in the quasi-momentum space. In this section, we will show that the evolution of such interference peak are the analogous of Bloch oscillations. We now start to remind to the reader which kind of eigenfunctions and eigenvalues solve the tilted-lattice problem. Under the influence of an external static force F , the system maintains properties of invariance with respect to an appropriate translation in both energy and z -space (see Sec. 2.4). One finds that each energy band splits into a sequence of equally spaced resonances, known as Wannier-Stark ladders which directly depends on the applied force. In the case of a gravitational force [94], the ladders are equally spaced by

$$\Delta E = mg \frac{\lambda}{2}. \quad (3.4)$$

The corresponding single-particle states are the Wannier-Stark functions which are localized in both momentum and z -space. Note that these functions differ in a profound way from the unperturbed Bloch states which describe particles delocalized in the whole lattice. The spatial extension of a Wannier-Stark state gives the degree of localization with respect to the lattice height considered. For instance, we find that, for $s = 2$, a Wannier-Stark state extends over about ten lattice sites.

In single-band approximation, Wannier-Stark states are eigenfunctions of the tilted potential and a particle loaded in such potential finds itself in a coherent superposition of Ψ^{WS} functions. As reported in the inset of Fig. 3.11, the gravitational potential tilts the lattice leading to a constant energy difference between atoms loaded in different lattice sites (see Eq. (3.4)). As a consequence, two wave-functions centered in neighbor sites evolve in time with a phase difference $\Delta\phi = \Delta Et/\hbar$:

$$\Psi_n^{WS}(z, t) + \Psi_{n+1}^{WS}(z, t) = \Psi_n^{WS}(z, 0) + \Psi_{n+1}^{WS}(z, 0)e^{i\frac{\Delta Et}{\hbar}}. \quad (3.5)$$

A particle, prepared in a linear combination of $\Psi^{WS}(z, t)$, exhibits therefore an interference pattern in momentum space which is periodic in time, with a period $T_B = \hbar/\Delta E$. In Fig. 3.11 we compare the momentum distribution of a single Wannier-Stark state with a superposition of those states. In the former case, the momentum distribution fills completely the first Brillouin zone while a superposition of Wannier-Stark states yields to an interference pattern with narrow equally spaced momentum peaks. In particular, if the force applied is the gravity, the peaks move in momentum space with constant velocity, accordingly to $\dot{q} = mg$. This motion corresponds to the semiclassical Bloch oscillation. The peaks spacing is the inverse of the spatial period of the lattice, and can be written as $2q_B$, where $q_B = \hbar/\lambda$ is the Bragg momentum. Therefore only one or two peaks appear at the same time in the first Brillouin zone of the lattice $[-q_B, +q_B]$, as shown in Fig 3.11. The above discussion shows the equivalence between the semiclassical Bloch oscillations and the motion of interference peak in the momentum space. This twofold description allows us to exploit the macroscopic Bloch oscillations as an interferometric scheme to measure force, as we will discuss in the next section.

We just mention now that also Zener tunneling can be studied in term of Wannier-Stark functions with some extra specifications. Since Zener tunneling is an interband transition effect, we have to consider the full band spectrum and the Wannier-Stark function are no more eigenfunctions of the tilted lattice. Indeed, out from a single-band approximation, these functions are metastable states, also known as resonances. One can explicitly the depletion of the first band by adding an imaginary term on the

Wannier-Stark ladders Eq. (2.43))

$$E_{n,j}(k) = \varepsilon_n(k) + jFd - i\frac{\Gamma_n}{2}, \quad (3.6)$$

where n is the band index, Γ_n the decay rate and $j \in \mathbb{N}$. The decay rate Γ_n defines the lifetime of the Wannier-Stark states, and exhibits a rather nontrivial dependence on the static force [107]. For a given force and lattice height, we have shown in Sec. 2.4.2 that the first band is depleted exponentially with time.

3.6 Atom interferometry with trapped Fermi gas

In this section we will focus on an interferometric scheme exploiting the long-lived Bloch oscillation observed with a trapped Fermi gas. Fermi gases have never been used as an atomic source in such kind of high-precision measurements. In our setup, we measure the force of gravity acting on the atoms along the lattice from the period of the Bloch oscillations. Our choice of the atomic source goes in the direction to take advantage from the non-interacting nature of this system: collisions are indeed suppressed in a sample of identical fermions. It is important to stress that the same Pauli principle that forbids collisions also limits the phase-space density of fermions to unity. These two effects arising from the Pauli principle affect in opposite way the sensitivity of our interferometer. We will therefore discuss whether this constitutes an obstacle to precise measurements.

In the last decade, atom optics and interferometry blend together giving rise to a new exciting field of investigation: *atom interferometry* which is mostly based on manipulation of neutral atoms with laser beams. The development of atom interferometry keeps up with the improvement of cooling techniques because of the dependence of the sensitivity from the atomic source used. During the years, interferometric measurement has been performed using a thermal source of atoms, a fountain of laser cooled atoms and finally a *well-collimated* source of condensed atoms. In particular, the advent of BECs was expected to produce in atom interferometry the same dramatic progress faced by photon interferometry after the invention of laser. A BEC is the brightest atom source with all the particles in the same quantum state, hence leading to an increase of the contrast of the interference signal [62, 42, 108, 109, 110]. However, despite to the largest brightness, condensed bosons interact each other and, how we have already discussed in Sec. 3.4.1. This also could affect dramatically interferometric measurements, giving rise to a shift or decay of the signal. This limitation can be somehow avoided performing measurements with samples in free fall

where interactions are weaker [109]. Nevertheless, this leads to a shorter observation times with respect to the one attainable with trapped samples. A alternative route is to adopt an atomic system free from interaction as a Fermi gas or a condensate with $a_B = 0$.

We will now start to describe a general scheme of interferometer and to compare it with our scheme using a fermionic source.

3.6.1 Scheme for an atom interferometer

The most fruitful applications of interferometric techniques with ultracold bosonic gases concern high-precision measurements of fundamental constants [109, 111, 113] and the detection of rotational properties [112]. Atom interferometers fall basically in two different classes: those exploiting different atomic *internal* states [114] and those in which the interference occurs between different paths of the atomic center-of-mass (i.e. *external* momentum states) [115]. We will focus mainly on the latter case where atom-light interaction change the momentum of the atoms without altering their internal state. Different schemes of interferometer have been proposed. Typical examples are the atomic analog of an optical Mach-Zender interferometer [116, 114] or a Young's double-slit [117] or a contrast interferometer [109]. Nevertheless, in the working of an atom interferometer, we can always distinguish 3 fundamental step:

- Step 1: Coherent creation of distinguishable atomic states (so-called *path*) from a single atomic source.
- Step 2: Evolution over some time of these different states.
- Step 3: Recombination and detection of the interference pattern of the atoms.

While in step 1 and 3 we have to manipulate the atomic source to get the desired states, step 2 is the one of physical interest because, in this phase, the atomic states are subjected to the forces that we would like to measure as the gravitational or electric-dipole force. From an experimental point of view, most of the work to produce a meaningful interferometer usually comes from trying to cancel, during step 2, any kind of force different from the one of interest. Note that the use of a single internal state, instead of multiple states, can reduce several interaction which perturbs the system. For instance, ac-Stark shift will not result in the type of systematic errors that occur when interference is measured between different internal atomic states.

Another important point is related to the choice of a proper way to manipulate the momentum of our "one-level" system. Optical standing waves can be used to modify

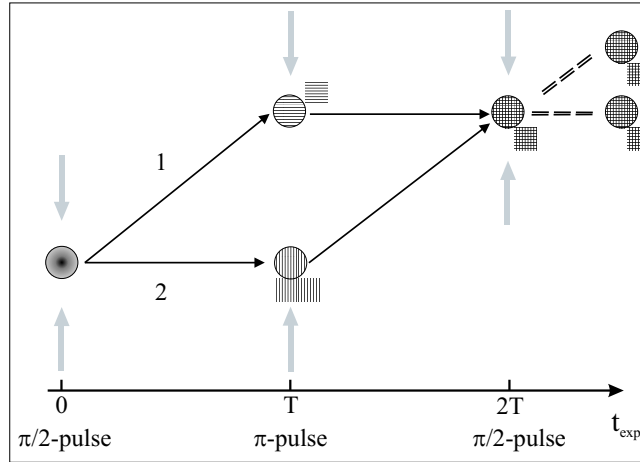


Figure 3.12: Scheme of a Mach-Zender interferometer. Three Bragg pulses are sent to a free-expanding BEC. Paths 1 and 2 are in states $|0\hbar k\rangle$ and $|2\hbar k\rangle$ for equal lengths of time T .

momentum states in a very controlled manner and allows to create arbitrary interferometer geometries (paths). Indeed, when an atom scatters a photon, it recoils due to the momentum exchanged with it. This mechanism also set the fundamental energy scale of the process: the recoil energy E_R . The manipulation is thus efficient if the thermal energy $k_B T$ of atoms is smaller with respect to E_R . As already discussed in Sec. ?? for Bragg scattering, an optical standing waves (also known as optical grating) is created from a counter-propagating laser beam which constrains an atom to change its momentum in multiples of $2\hbar k$, where k is the wavevector associated to a single photon.

As an example, we now briefly discuss a simple scheme of interferometer based on Bragg process which is known as Mach-Zender configuration. This procedure has been already used with a thermal beams [118] of atoms and with a BEC [119]. A BEC is initially prepared in a magnetic trap and then released from it. The subsequent experimental phases are reported in Fig. 3.12:

- Step 1: Beginning with atoms at rest, we apply a first $\pi/2$ -Bragg-pulse which acts as a beamsplitter. The atomic cloud is thus 50-50 divided into two different momentum states: $|0\hbar k\rangle$ (at rest, path 2) and $|2\hbar k\rangle$ (in motion, path 1).
- Step 2: We let the atoms in different arms to evolve during a time T with a relative velocity of 2 photon recoils.

- Step 3: After a time T , a π -pulse is applied and atoms in $|0\hbar k\rangle$ -state are transferred into the other momentum-state. The third pulse is needed for the detection of the contrast signal projecting the phase of the atomic interference pattern onto the fractional population of the two momentum state.

Any interaction placed differentially on one arm of the interferometer would be picked up by the phase difference between the two paths which gives rise to the interference signal. Thus Mach-Zender interferometer can be used to measure rotational phases, gravitational phases, electric polarizability, or index of refraction of gases [120].

While Mach-Zender interferometer uses atoms in free-expansion, in our interferometer scheme fermions are trapped in a optical lattice and, in principle, one can follow the evolution (step 2) for a time comparable to the lifetime of the sample increasing the sensitivity of our measurement. The basic idea of our scheme is to derive the acceleration of gravity g by measuring the period T_B of the periodic motion performed by the atoms into the lattice. Let now to identify the 3 steps necessary to produce an interferometer:

- Step 1: Starting with a magnetically trapped Fermi gas, we adiabatically load the atoms in the tilted lattice². Now each atom is in a coherent superposition of Wannier-Stark states. The interference between such states gives rise to narrow peaks in the momentum space.
- Step 2: We let the interference peaks to evolve under the force of gravity for variable holding times.
- Step 3: We switch off adiabatically the lattice to map the momentum distribution of atoms into a quasi-momentum distribution which extends over the first Brillouin zone. After 8 ms of expansion, we probe the cloud by absorption imaging.

Repeating the measurement for different holding time in the lattice, we observe a vertical motion of the peak of the distribution i.e. the Bloch oscillation driven by the gravity (see Fig. 3.8). As we will discuss in the next section, this scheme allows us to extract a value of g .

²We remind to the reader that the optical potential is tilted due to the presence of the gravity.

3.6.2 Measurement of g

We have already shown the vertical motion of the interference peaks. From the period of the Bloch oscillations we measure the force of gravity acting on the atoms along the lattice³ as

$$g = \frac{2h}{T_B m \lambda}. \quad (3.7)$$

We fit the experimental data of Fig. 3.8 with a sawtooth function and we find a Bloch period $T_B = 2.32789(22)$ ms. If we assume that the only uniform force acting on the atomic sample is gravity, we immediately determine a local gravitational acceleration as $g = 9.7372(9)$ m/s². Note that, at this level of sensitivity, the relative uncertainty on g is just the same as on T_B , since both h and m are known with a high accuracy and also λ can be accurately determined [121]. The evolution of the interference peaks develops on a micrometrical scale and thus our interferometer based on trapped atoms opens the possibility of probing forces with a high spatial resolution.

We note that the vertical size of the sample in the present experiment is substantially determined by the initial size in the magnetic trap, which in principle can be reduced by increasing the vertical confinement. The minimum possible size is instead set by the extension of a single Wannier-Stark state, which also corresponds to the amplitude of the Bloch oscillations in real space. At $U = 2E_R$ this amounts to about $4\mu\text{m}$, and decreases further for increasing depths as $2\delta/F$, where 2δ is the width in energy of the first Bloch band of the lattice.

As already pointed out, the usefulness of an interferometer is strictly connected to the possibility to cancel any kind of undesired additional forces acting to the sample. Clearly, the use of a tight optical lattice to trap the sample might affect the accuracy of a measurement of forces. In particular, any axial gradient in the intensity of the lattice beams will result in an additional force on the sample. In the experiment we have checked the absence of a dipole force at the level of our present sensitivity, by repeating the experiment with a 50% larger intensity of the lattice beams. This did not produce a noticeable change of the Bloch period.

Another possible source of systematic error is connected to the presence of spurious magnetic fields. Indeed, since the fermions have a magnetic moment, the Bloch period is sensitive also to magnetic forces

$$F = mg + g_F m_F \mu_B B, \quad (3.8)$$

³In general one can measure any kind of force applied on the system during step 2. Thus the force is $F = 2h/T_B \lambda$.

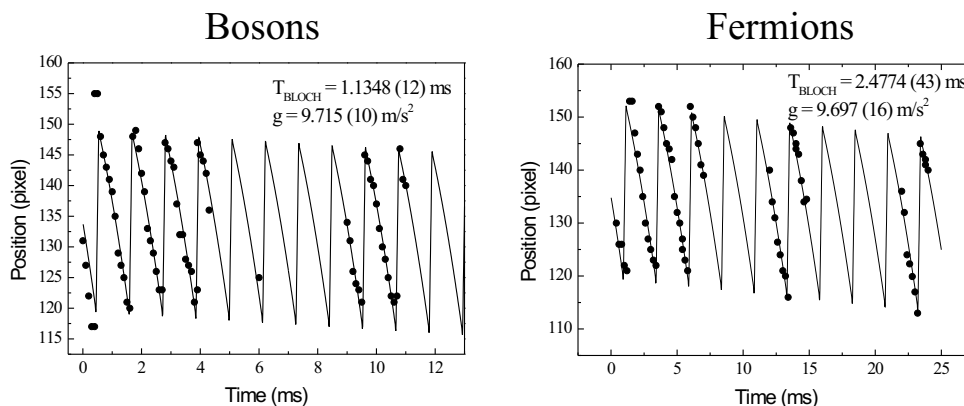


Figure 3.13: Comparison between Bloch oscillation driven by gravity performed by a cloud of condensed Rubidium atoms with respect to the one observed for a Fermi gas of Potassium atoms. The two measured g are compatible within an accuracy of 10^{-3} .

where g_F is the Landé factor, m_F labels the hyperfine level and μ_B is the Bohr magneton. On the one hand Eq. (3.8) indicates that our interferometric scheme can be used to estimate magnetic force acting on the atoms during step2, while, on the other hand, it shows that undesired field B affects the measurement of g . Furthermore, inhomogeneities in the magnetic field can also produce residual forces. In general, one can control this effect by repeating the measurement with two atomic states with different magnetic moment. Thanks to our experimental apparatus, we can study Bloch oscillation using different atomic species which have a different mass and magnetic moment. We repeat the measurement of Fig. 3.8 with both potassium and rubidium atoms. As shown in Fig. 3.13, the values of g measured in the two case for same conditions are compatible. This result demonstrates the absence of extra magnetic forces at the level of 10^{-3} . This accuracy is limited by the short measurement time achievable for bosons (see Sec. 3.4.1). Note that during the measurement reported Fig. 3.8, we kept a small and known homogeneous magnetic field (about 1 G) to avoid spin-flips, which would produce distinguishable particles which could collide each other. Data of Fig. 3.13 are instead free from this additional magnetic field.

The sensitivity reached with our apparatus is limited to 10^{-4} mainly by the 250-ms time interval available for the measurement. Fig. 3.14 together with Fig. 3.9 a clearly demonstrate the degradation of our interference measurement at long time. In Fig. 3.14 we plot the relative height of the two peaks $A_{1,2}$ as a function of time which decreases with time. Since the atom number is constant during the measurement, this behavior corresponds to a broadening of the atomic distribution. The timescale of this

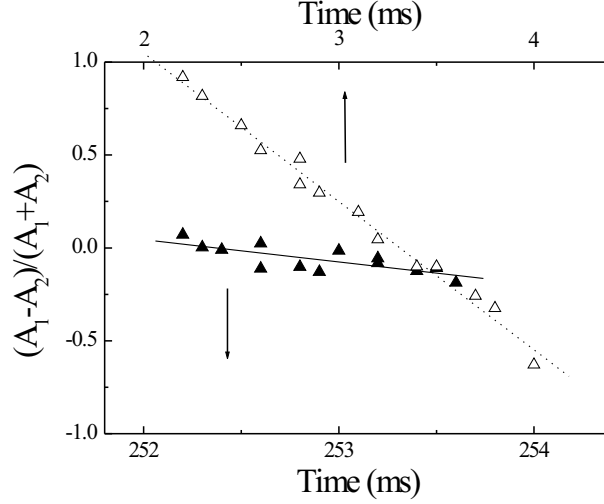


Figure 3.14: Relative height of the two interference peaks at short (empty triangles) and long time (filled triangles). Since the atom number remains nearly constant, the data clearly show a broadening of the peaks which reduces the contrast of the atomic signal.

broadening is much shorter than the characteristic time for p -wave collisions [122] which exceeds 100 s for our experimental conditions. Thus we can not ascribe this effect to a collisional mechanism. The main sources of the broadening are presumably intensity and phase noise in the lattice beams. Also ergodic mixing of the radial and axial motions, a finite axial curvature of the lattice intensity and a residual scattering of the lattice photons could contribute to the observed broadening. All these effects could be reduced by using active stabilization of the lattice, a proper beam geometry and a larger detuning. This improvement should allow to extend the observation time to several seconds, with a corresponding increase of the sensitivity. The sensitivity can be increased also by using a larger atom number and/or a longer wavelength for the lattice. Both operations tend to broaden the momentum distribution with respect to q_B : on the one hand in a Fermi gas the momentum spread increases with the atom number N according to $\delta q \propto N^{1/6}$, and on the other the Brillouin zone shrinks for increasing wavelengths as $q_B \propto 1/\lambda$. One could however compensate for both these effects by using a looser radial confinement of the atoms, which would reduce the momentum spread without affecting the axial size of the cloud.

Possible applications of our interferometric scheme can be the study of forces close to surfaces and at the sub-millimeter scale, recently motivated by the possibility of

new physics related to gravity [123].

Chapter 4

Localization in a combined periodic and harmonic potential

Oscilla o non oscilla ?

A me oscilla ...

F. F. e L. P.

As discussed in Chap.3, a Fermi gas in a pure optical lattice exhibits a Bloch oscillation as soon as a linear potential ($U = Fx$) is applied. The observation of such phenomena establishes a tight connection with usual system of solid-state physics, such as electrons in a crystal when an uniform static electric field is applied [87]. Note that one can strictly speak about Bloch oscillations only if the applied external force turn out to be constant both in space and time. In general, as soon as the translational invariance of the system is destroyed or modified, localization effects take place depending on the perturbation applied. One can change the translational properties both adding an external force or by introducing some imperfections to the lattice. For instance, in presence of a constant force F , delocalized Bloch particles are mapped into Wannier-Stark states (Sec. 2.4.3) which extend over a spatial interval δ/F . Another kind of localization observed in metal is the Anderson localization¹ which is observed when a ion crystal exhibits a disorder, for instance when the spacing between the atoms is slightly irregular with small, random perturbations. In the field of atomic gases, a localization due to the presence of an extra potential is easier achievable since one can manipulate the gases by applying magnetic fields. Since atomic gases are usually harmonically trapped (see Sec. 1.2-1.3.2), the first natural extension with respect to the linear case is to study a gas subjected to a combined

¹Phil Anderson won the Nobel prize in 1977 for his investigations into this issue.

periodic and parabolic potential.

In this Chapter, we report on the behavior of both a Fermi and Bose gas in a combined periodic and harmonic potential which we have observed in our experiment. We summarize below the major results of this investigation.

4.1 Outline

In this Chapter, we move from a quantum gas trapped in a pure optical lattice (Chap. 3) to a gas loaded in a combined parabolic and periodic potential. We find that the quadratic external potential introduces a localization in the system which affects both the density of states and the transport properties of our unperturbed system. In particular, we observe that localized particles are nailed on the sides of the parabolic potential, and can not reach the minimum of the potential. We study this effect using both a theoretical and experimental approach. For sake of clarity, we report first on the theoretical description of our system which provides the single-particle energy spectrum of the combined parabolic and periodic potential (Sec. 4.2). This spectrum admits two classes of solutions, corresponding to particles delocalized along the lattice and to particles localized on the sides of the potential. We are able to address experimentally atoms in localized states by using a novel method based on a rf-spectroscopy (Sec. 4.3). This technique is selective in energy and, thanks to the fact that delocalized particles occupy the bottom of the energy spectrum, we can remove only atoms in this class of states. In this way, we can thus study just localized atoms which reveal highly non-classical features both in their energy distribution and in their expansion dynamics. We then study the dynamical response of localized fermions to a dipolar excitation. The center-of-mass motion reveals that localized fermions act as an *insulator* under a driven potential. On the contrary, the transport properties of delocalized atoms indicate the conducting nature of such states (Sec. 4.5). We can directly study the motion of delocalized states by using a Bose-Einstein condensate. Due to their narrow energy distribution, condensed bosons can indeed occupy only low-energetic delocalized states (Sec. 4.5).

The reader can find most of the results presented here in our recent publications listed below:

- *Radio Frequency Selective Addressing of Localized Particles in a Periodic Potential*, H. Ott, E. de Mirandes, F. Ferlaino, G. Roati, V. Türeċk, G. Modugno, and M. Inguscio, cond-mat/0404201 (2004).

- *Insulating Behavior of a Trapped Ideal Fermi Gas* , L. Pezzé, L. Pitaevskii, A. Smerzi, S. Stringari, G. Modugno, E. de Mirandes, F. Ferlaino, H. Ott, G. Roati, and M. Inguscio, accepted in Phys. Rev. Lett. , cond-mat/0401643 (2004).
- *Production of a Fermi gas of atoms in an optical lattice* , G. Modugno, F. Ferlaino, R. Heidemann, G. Roati, and M. Inguscio, Phys. Rev. A **68**, 011601(R) (2003).
- *Collective Excitations of a Trapped Bose-Einstein Condensate in the Presence of a 1D Optical Lattice*, C. Fort, F. S. Cataliotti, L. Fallani, F. Ferlaino, P. Maddaloni, and M. Inguscio, Phys. Rev. Lett. **90**, 140405 (2003).

4.2 Periodic plus harmonic potential: A new problem

In our experiment, bosons and/or fermions are trapped in a 3-D harmonic potential with a cylindrical symmetry. The 1D optical lattice is superimposed along the weak axis of the parabolic potential (the axial direction is x). The total Hamiltonian is thus

$$H = \left(\frac{p_x^2}{2m} + \frac{1}{2}m\omega_a^2 x^2 + \frac{s}{2}E_r(1 - \cos 4\pi x/\lambda) \right) + \left(\frac{p_z^2 + p_y^2}{2m} + \frac{1}{2}m\omega_r^2(z^2 + y^2) \right). \quad (4.1)$$

Note that the 3-D problem turns out to be decoupled along the three directions and can thus be separated in three one-dimensional problems. We focus only on the stationary single-particle Schrödinger equation along the lattice direction:

$$\left[-\frac{\hbar^2}{2m} \frac{\partial^2}{\partial x^2} + \frac{1}{2}m\omega_a^2 x^2 + \frac{s}{2}E_r(1 - \cos 4\pi x/\lambda) \right] \psi = E_n \psi. \quad (4.2)$$

We remind to the reader that s denotes the depth of the optical potential in units of the recoil energy $E_r = \hbar^2 k^2 / 2m$.

Although many experimental studies have been performed in this combined potential during the last years, the solution of Eq. (4.2) is attracting big attention just in the last months [124, 125, 126]. This missed attention to Eq. (4.2) is mainly due to the properties of the atomic sample usually used in such kind of problem. Indeed most of the experiments with optical lattice are made on a trapped Bose-Einstein condensate, which exhibits a very narrow distribution both in the coordinate and momentum space. Since condensed bosons occupy just a narrow region at the bottom of the first energy band, one can still describe the system by introducing an effective

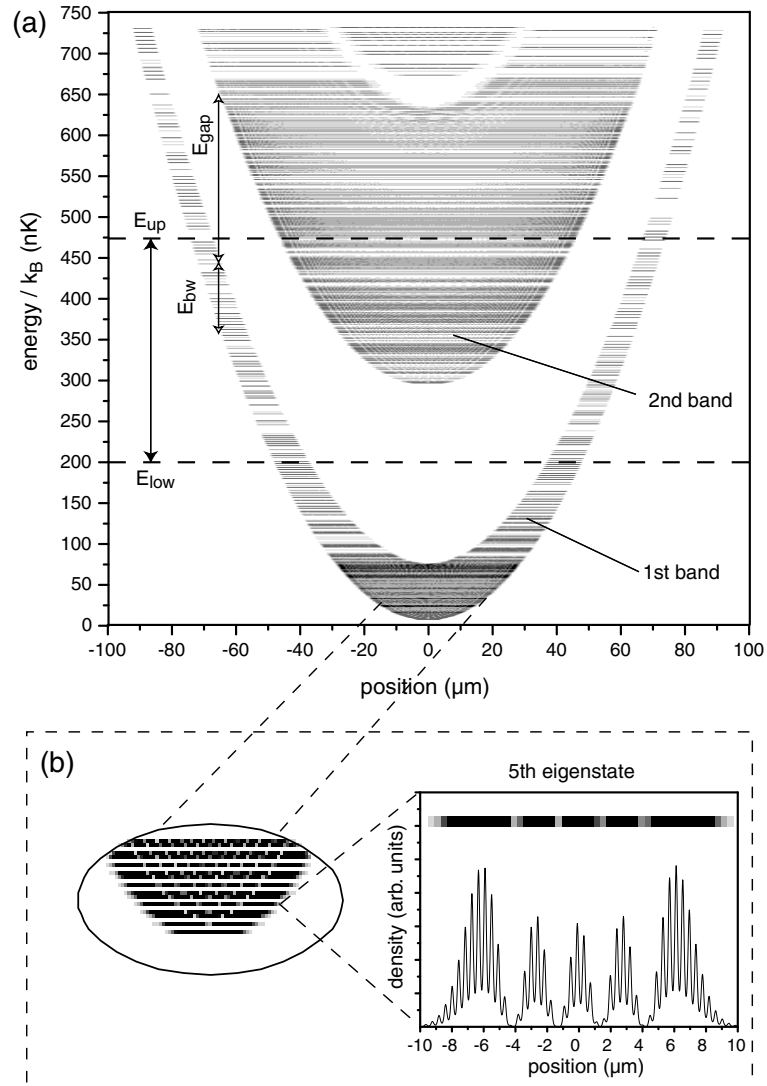


Figure 4.1: (a) Spectrum of the Hamiltonian: representation of the 1D spectrum of the single particle Schrödinger equation for a combined periodic and parabolic potential. Each line represents one eigenstate of the system, which is plotted as density profile in grayscale (see (b)). The vertical position of the profile corresponds to the energy of the eigenstate. The potential parameters were chosen to be $\omega = 2\pi \times 16$ Hz, $\lambda = 830$ nm and $s = 3$ and the mass is that of ^{87}Rb .

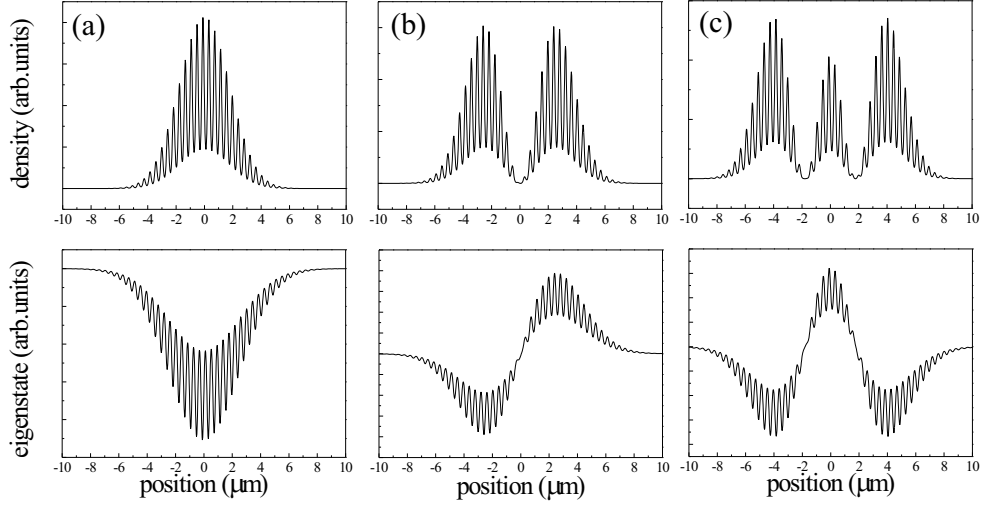


Figure 4.2: Delocalized functions together with their density distribution $|\psi|^2$ for $s=3$. The eigenfunctions calculated from Eq. 4.2 are relative to the first (a), second (b) and third (c) energy level of the combined potential. Note that the shape of the wave-functions is due to the harmonic confinement while the fast modulation is due to the optical potential.

mass m^* which takes fully into account the different inertia of the condensate², due to the lattice [40, 128, 129]. The scenario changes completely when we deal with a gas of particles occupying several excited states of the system. In this condition, one has to take into account also the harmonic trap which brings new features to the already interested pure-periodic potential. This is the case of a cloud of thermal atoms and of a Fermi gas which exhibit a broad energy distribution. For instance, in the latter system, the Pauli principle enforces indeed fermions to occupy one by one the energy levels and higher energetic state are reached.

4.2.1 Localized vs delocalized states

An atomic gas in the combined potential loses its translational invariance due to the quadratically trapping potential necessary to confine the gas. As discussed in Chap. 2-3, a change in the translation property of the system is always accompanied to the appearance of localized states. For instance, a particle in a lattice is described by localized Wannier-Stark states as soon as a linear driven potential is applied. It turns out natural to expect localization phenomena also in presence of a parabolic

²This model is appropriated to study the dynamics of a condensate only in the limit of small external perturbation, as discussed in our work [40, 127]

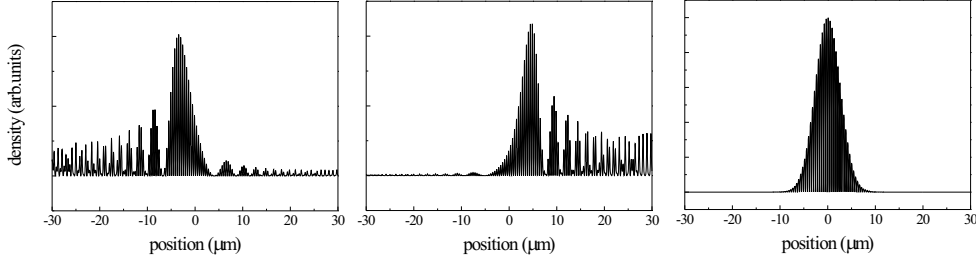


Figure 4.3: Density distribution $|\psi|^2$ for $s = 3$ of the 121th (a), 122th (b) localized states and (c) first delocalized state in the second band.

potential. To test this expectation one has to solve Eq. (4.2). Without any approximation, Eq. (4.2) can not be solved analytically and a numerical approach is needed. The Hamiltonian (4.2) has been recently studied in tight binding approximation in [124, 125]. In particular, these works lie in a single-band approximation while in our system also higher band can be occupied.

We solve numerically the eigenvalue problem (4.2) for our typical experimental parameters. Starting from Eq. (4.2), the numerical procedure is based on a discretization of the Hamiltonian along the x -axis (~ 1000 spatial-step). The second derivative in the kinetic term can thus be replaced by the differential increment. At this point we diagonalize the discrete Hamiltonian to find the eigenvalues of the problem, which are used to get the eigenfunctions directly from the eigenvalue problem. The full energy spectrum found is reported in Fig. 4.1a which shows a density plot of the first 1000 eigenfunctions. Each line in Fig. 4.1a corresponds to a density plot of the wave function in coordinate space, as sketched in Fig. 4.1b. This spectrum is clearly different from the one obtained with a pure harmonic trap or with a pure optical lattice.

The shape of the single-particle energy spectrum reveals the existence of two distinct class of solutions. For low energies we find delocalized states that spread symmetrically around the potential minimum. These states are the analogous of Bloch states, introduced in Sec. 2.3. Typical delocalized functions are shown in Fig. 4.2 together with their density distribution $|\psi|^2$. Note that the shape of the wave-functions is similar to the corresponding eigenstates of a pure harmonic oscillator while the fast modulation is due to the optical potential. Above a threshold energy, the second class of solution appears. These eigenstates go to zero around the trap minimum resulting in a localization over just few lattice sites. Typical localized states are drawn in Fig. 4.3(a)-(b). These eigenstates are no more symmetric with respect to the center of the trap and become localized on both sides of the potential. Particles have indeed

maximum probability to be in the left (Fig. 4.3(a)) or in the right (Fig. 4.3(b)) of the potential. These localized states are the analogous of the Wannier-Stark states found in presence of a linear force (see Sec. 2.4.3).

If we look at even higher energies, a second group of eigenfunctions appears, centered again around the trap minimum. These states correspond to particles delocalized on the bottom of the second band where they experience again an harmonic-like potential (see Fig. 4.3(c)). By further increasing the energy, we will again find localized states but now related to the second band. The spectrum of Fig. 4.1 exhibits clearly a shell-like structure and from the first to the last energy level we can recognize a sequence of delocalized and localized state. It is straightforward to identify this spectrum with the well known band picture for a pure periodic potential³, as comes out from the energy spectrum reported in Fig. 4.1. Despite of the analogy with the band structure, our *bent-tube* spectrum exhibits new important features. For a given position, not all the energy are allowed because a spatially varying gap opens in presence of a parabolic confinement. The accessible energy values stay in an interval E_{bw} with an extension equal to the bandwidth 2δ calculated for a pure sinusoidal potential. We also found a one-to-one correspondence between the forbidden energy interval and the usual band gap E_{gap} . As a consequence, in presence of a harmonic potential, we can no more speak about an absolute energy gap but we have to refer to a spatial energy gap. The behavior of our new energy spectrum suggests the possibility to investigate, in a selective way, localized states which are never been observed so far.

4.2.2 Experimental setup

We start to describe our experimental procedure to produce an ultracold atomic gas in a combined parabolic and periodic potential [48].

As reported in Chap. 1, our apparatus allows to prepare either a fermionic sample of ^{40}K atoms, either a bosonic one of ^{87}Rb atoms. After the laser cooling phase (pre-cooling stage), the atomic sample is initially loaded into a harmonic trap with cylindrical symmetry along the z -axis (axial direction). We perform on trapped Rb atoms a selective evaporative cooling using radio-frequency radiation. K atoms are instead sympathetically cooled through elastic interspecies collisions. Both species are trapped in their doubly polarized spin states, $|F = 9/2, m_F = 9/2\rangle$ for K and $|2, 2\rangle$ for Rb. In these states, the two samples experience the same trapping potential, with axial and radial harmonic frequencies $\omega_a = 2\pi \times 24 \text{ s}^{-1}$ and $\omega_r = 2\pi \times 317 \text{ s}^{-1}$

³Note that, the band spectrum is usually referred to the quasi-momentum space while our energy spectrum is obtained in the real x -space.

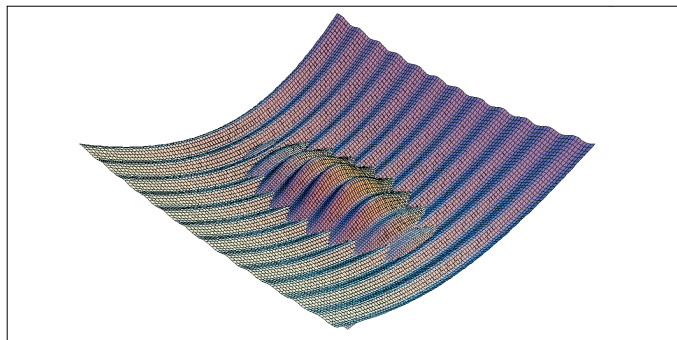


Figure 4.4: Sketch of the 1D harmonic plus periodic potential experienced by the atoms. The harmonic magnetic potential is produced by means of two coils in quadrupole-Ioffe configuration and one pinch coil. The periodic potential is instead optically produced by two counter-propagating laser beams in standing wave configuration.

for K, while those for Rb are a factor $(M_{Rb}/M_K)^{1/2} \approx 1.47$ smaller. Typically we can produce 5×10^4 fermions at about $0.3 T_F$ ($T_F=430$ nK) and a condensate of Rb with a similar atom number at $T < T_c=150$ nK. In general, we stop the evaporation when the desired temperature is reached. When the evaporation is mostly finished we superimpose along a 1D optical lattice the axial direction. To optimize the loading, the lattice power is raised adiabatically in about 500 ms reaches its final value at the end of the evaporative cooling stage. The total potential experienced by the atoms is drawn in Fig. 4.4. The lattice is produced by a far-detuned, retroreflected laser beam with a typical beam waist of $500 \mu\text{m}$. The wavelength of our laser beam is chosen to be far detuned with respect to all the optical transitions of K and Rb atoms to avoid heating mechanism of the sample. For instance, if the laser light is blue-detuned, the lattice potential is repulsive with maxima at the antinodes of the standing wave (for red-detuned is the viceversa). The potential height of the optical standing wave can be adjusted between $0 < s < 10$, where s is the lattice height in unit of the recoil energy $E_R = \hbar^2 k^2 / 2m$ with $k = 2\pi\lambda$ and m is the atomic mass.

4.3 rf-Spectroscopy of localized states

As shown in Fig. 4.1, particles with energy lower than the bandwidth $E_{bw} = 2\delta$ ($2\delta \simeq 0-80$ nK for $s=3$) are delocalized in the bottom of the first band. To study localization, we need to load in such combined potential an ultracold atomic gas with energies up to 2δ . Good candidates to address particles in such localized states are a

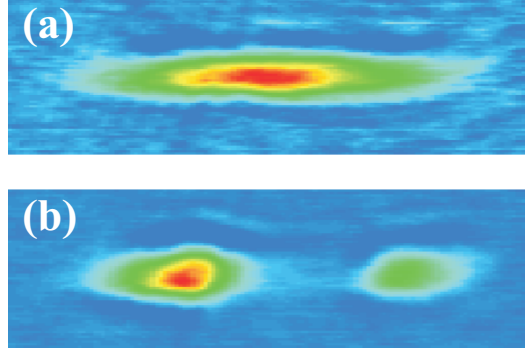


Figure 4.5: Observation of localized states. (a) Cloud of bosons without rf field and (b) with rf field after 1.5 ms time of flight.

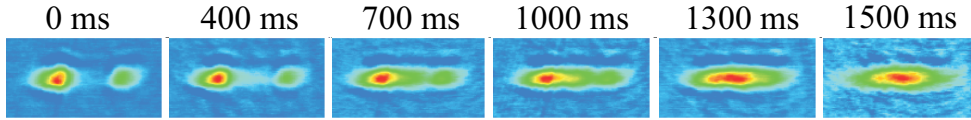


Figure 4.6: Decay of localization due to interatomic collisions. Absorption images of bosons left in the combined trap for different holding time. Localized bosons slowly move toward the center of the magnetic trap on a time scale of the order of 1 s. The measurements are taken with an optical depth of $s = 6$.

thermal cloud of bosons or a degenerate Fermi gas, because of their broad momentum distribution. For definiteness, we concentrate our effort on a bosonic thermal cloud, although the spectral features are equally valid for fermions.

4.3.1 Experimental technique

To fulfill the requirement of $E > 2\delta$, we stop the evaporation of Rb atoms when the sample reaches a temperature which ranges from 500 to 600 nK . Note that this temperature is well above the critical temperature for Bose-Einstein condensation. The optical lattice used for these set of measurements has a wavelength $\lambda = 830$ nm. We choose an optical height s which leads to a bandwidth 2δ much smaller than the average energy of the atoms, thus providing a high population in localized states. Since the periodic potential affects only axially the system, the particles occupy pure harmonic oscillator states in the two radial directions.

To study localized states we use a spectroscopic technique based on the selective removal of delocalized bosons from the trap. After the end of the evaporation and the

adiabatic switch on of the optical potential, we apply a radio frequency (rf) field in order to induce spin flip transitions between trapped and untrapped states. Because of the magnetic radial confinement this removes all atoms whose wavefunction has a spatial overlap with the magnetic field shell where the resonance condition

$$h\nu = \mu_B B(\mathbf{r})/2 \quad (4.3)$$

is fulfilled. In a pure quantum mechanical description the resonance condition for the involved Zeeman transitions is given by $h\nu_{m_{\mathbb{F}=2} \rightarrow m_{\mathbb{F}=1}} = E_{m_{\mathbb{F}=2}} - E_{m_{\mathbb{F}=1}}$, and $h\nu_{m_{\mathbb{F}=1} \rightarrow m_{\mathbb{F}=0}} = E_{m_{\mathbb{F}=1}}$, where $E_{m_{\mathbb{F}=2,1}}$ are the energies of the single particle states in the $|F = 2, m_{\mathbb{F}=2,1}\rangle$ state (we have set the energy of the $|F = 2, m_{\mathbb{F}=0}\rangle$ state to zero). The radio frequency is periodically modulated (1 kHz) within an interval $\Delta\nu = \nu_{\text{up}} - \nu_{\text{low}}$ (see again Fig. 4.1) to address a spatial region in which the atoms are removed from the potential. After 100 ms of rf field we image the atoms which are left in the potential.

In Fig. 4.5 we show an absorption image of the atomic cloud after 1.5 ms of expansion without and with rf field. In the latter case we remain with two clouds, located at the edges of the original cloud. Looking at the energy spectrum, this nearly corresponds to a removal of atoms with energy lower than 2δ . We are thus able, using this spectroscopic method, to transfer just delocalized atoms in untrapped Zeeman levels ! Figure 4.5(b) shows the new equilibrium distribution of our system composed now only by localized bosons. Note that even if we leave on the rf field for one second we still end with two separated clouds. After switching off the rf field, we hold bosons in the combined potential for a variable time to check the timescale of localization process. For high lattice height ($s > 3$), we have observed long-lived localization with the peculiar two peaks pinned on the sides of the combined potential. On the contrary, if we perform the same measurement with atoms in a pure harmonic potential, we observe a complete removal from the trap due to the applied rf-field. This removal takes place on a timescale comparable to the re-thermalization time (some ten of ms). In presence of a tight lattice, the two peaks remain instead on the two sides of the potential for a very long time. In Fig. 4.6, we show absorption images of bosons at $s = 6$ for different holding times. Bosons decay toward the trap center on a time scale of 1 s. This decay is due to collisions between bosons which allow a hopping between different states, as will be discussed in detail in Chap. 5. However, if we repeat the measurement using a shallow lattice we observe a substantial decrease of the two-peak lifetime. Note that if we repeat the same experiment using a cloud of spin-polarized fermions this effect is obviously absent.

The usefulness of our spectroscopic method is connected to our ability to remove

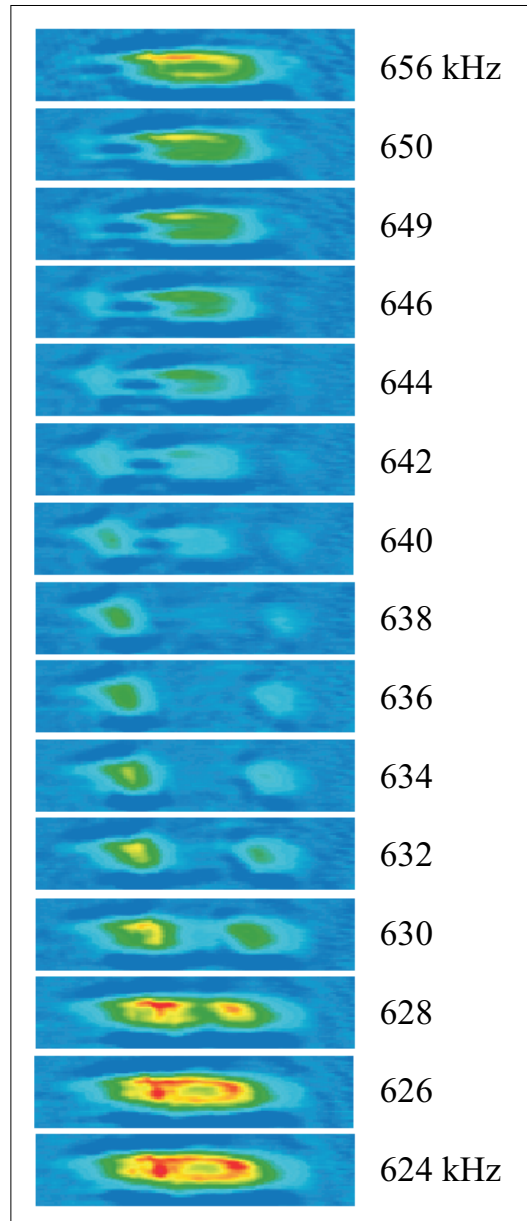


Figure 4.7: Energy distribution of localized states. Scan of the rf field through the cloud of thermal bosons. The indicated frequencies are the upper frequency ν_{up} of the rf field, the bandwidth of the field is 3 kHz. The images are taken after 1,5 ms time of flight.

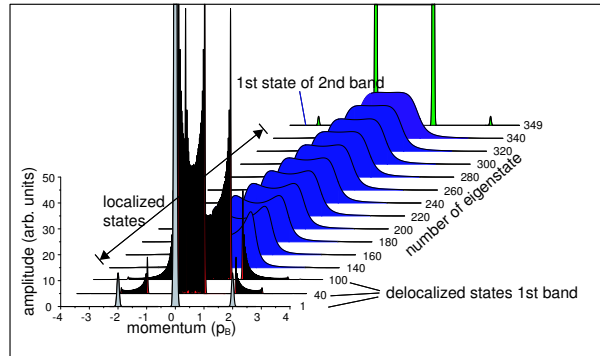


Figure 4.8: Momentum distribution of the localized states. Fourier transform of the eigenstates of Fig. 4.1. The red states lie within the first band, the green state is the lowest state of the first excited band. The blue curves describe localized states.

selectively the undesired states with the rf-knife. In Fig. 4.7 we report a series of absorption images where we have scanned the rf field fixing the frequency interval $\Delta\nu = 3$ kHz. Increasing the rf frequency we start to remove atoms from the center of the trap. The hole in the spatial distribution deepens, until the lower frequency bound is higher than the resonance frequency at the trap bottom: atoms in the center are no longer removed from the potential and we observe three clouds. The central cloud corresponds to delocalized atoms in the bottom of the first band while the lateral cloud are due to particles localized in the higher energy state. By further increasing the frequencies, the displaced peaks disappear and the cloud is again unaffected by the rf-knife.

These measurements clearly prove that the atoms in the two clouds are trapped in localized states and that the rf field addresses the atoms in a defined spatial region. As we will discuss in next sections, we are also able to detect the localization of the atoms by looking at the center of mass of the whole cloud [50, 51, 48].

So far we have investigated the spatial distribution of atoms. Equation 4.2 gives also the possibility to study the momentum distribution of the localized states which provide useful information on the system. For a potential depth of $s = 3$ we have calculated the Fourier transform of the eigenstates $\psi(x)$. Our findings are summarized in Fig. 4.8 which shows the momentum distribution for selected eigenstates within the first and second band. The lowest eigenstate shows the well known peak distribution at multiples of twice the Bragg momentum. As shown in Fig. 4.9, this momentum distribution can be directly observed using an expanding Bose-Einstein condensate⁴.

⁴After a long expansion time, the imaged profile corresponds to the momentum distribution of the cloud in trap.

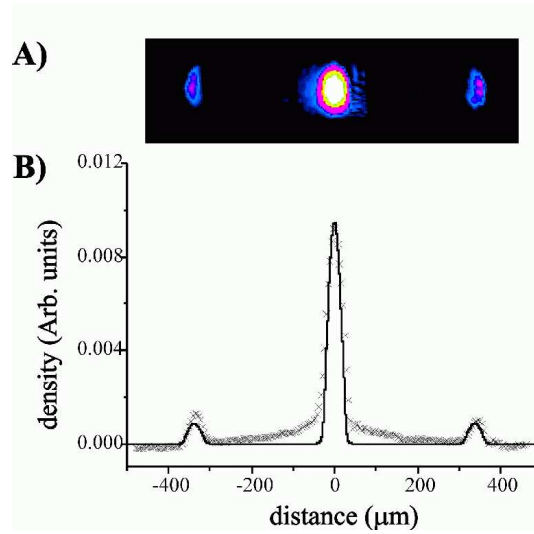


Figure 4.9: Interferogram of a Bose-Einstein condensate loaded in the combined potential with a lattice height $s = 5$. A) Absorption image of the cloud after 29.5 ms of expansion. B) Experimental momentum distribution (crosses) obtained from the absorption image. The wings of the central peak result from a small thermal component. The continuous line corresponds to the calculated density profile for the expanded condensate for the experimental parameters [130].

Indeed condensed particles fulfill the requirement of macroscopic occupation of the lowest energy state which is clearly delocalized. The width of each peak is larger with respect to the one expected from Fig. 4.8 because of the boson-boson mean field interaction which spread the distribution in momentum space.

Coming back to Fig. 4.8, as soon as atoms occupy upper energy levels, these peaks broaden and develop a substructure. For even higher eigenvalues, we found again localized states, whose distribution in momentum space spreads over the first Brillouin zone ($\pm p_B$). All localized states arrange themselves in a similar way, regardless the energy of the state. Eigenfunction at the bottom of the second band are again delocalized and their Fourier transform exhibits narrow peaks in the momentum space shifted by the Bragg momentum with respect to the ones found for the ground state (349 eigenstate in Fig. 4.8).

The optical lattice provides to the system an extra confining energy only in the axial direction while in the radial direction the cloud has a pure harmonic momentum distribution. Consequently, localized clouds are expected to exhibit an anisotropic expansion. In Fig. 4.8 (b) we show an absorption image of a localized cloud after

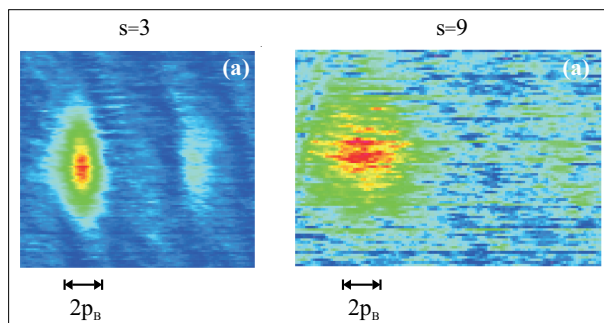


Figure 4.10: Absorption image of a cloud of atoms which was prepared with our rf technique after 10 ms time of flight (a) for $s = 3$ (b) for $s = 9$.

10 ms time of flight for $s = 3$ and $s = 9$. For $s = 3$, we measure a radial-to-axial aspect ratio of 2.5 which is notably different from the one found for a harmonically trapped cloud ($R_r/R_a \simeq 1$). This value confirms the high anisotropy of the system in presence of an optical lattice and indicates the nonclassical momentum distribution of the localized states. For $s = 9$ the cloud expands much faster in the direction along the lattice (horizontal direction) revealing the larger ground state energy. Indeed we calculate a 2 times larger momentum distribution for $s = 9$ with respect to $s = 3$ which leads to a nearly isotropic expansion.

4.3.2 Localization and addressability

The degree of localization of particles is a crucial point for the possible applications of our spectroscopic method. This kind of information can be extracted by looking directly at the extension of such localized states. In general, the extension depends both on the local gradient provided by the parabolic confinement and on the lattice height. Since our theoretical model gives the possibility to scan a large interval of lattice height s , we can investigate the behavior of bosons/fermions starting from a weak binding regime up to a Mott insulator one. In Fig. 4.11a, we plot the behavior of such extension as a function of the lattice height for three different energies which correspond to three different potential gradients. For low lattice, our states are localized in space over several lattice sites (the size of a lattice site is about $\lambda/2 \simeq 0.4 \mu\text{m}$). Increasing s , the number of sites involved decreases until just one site is occupied. Fig. 4.11 (a) also shows that localization is enhanced at high temperature. This result is somehow counterintuitive if one misses the knowledge of the energy spectrum.

Note that interband transitions reduce the degree of localization of our states. In particular, tunneling process between bands are strongly enhanced in shallow lattice.

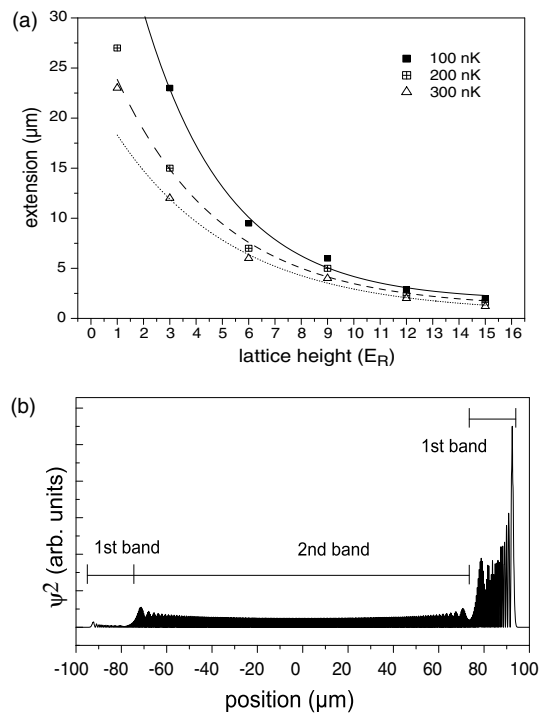


Figure 4.11: (a) Extension of the localized states in the first band in dependence on the lattice height for three energies ($k_B \times 100$ nK, $k_B \times 200$ nK, and $k_B \times 300$ nK). (b) Tunneling between the bands: density distribution of the 594th eigenstate for a potential with $s = 0.3$.

As an example, we report in Fig. 4.11 (b) the density distribution of an excited state for $s = 0.3$. It turns out that a particle in such a state exhibits substantial contributions from both the first and the second band. On the one hand indeed this particle has a finite probability to be localized on the right side of the first band while on the other hand it also has a probability to be delocalized in the bottom of the second band. The latter effect yields to an increase in the extension of our states. States like the one reported in Fig. 4.11 (b) can no longer be identified with those of the two classes reported above, and one should return to the concept of resonances (see Sec. 2.4.3). These results provide a tight link with Wannier-Stark resonances which are completely localized until the probability of transition to a higher band can be neglected and stretch themselves for high interband tunneling rate (low s). Note that for even weaker lattices, the eigenstates become those of a pure harmonic oscillator.

Increasing the depth of the optical lattice, the extension of the localized state shrinks (Fig. 4.11a) and the smallest possible extension is given by the ground state in each lattice site. For our parameters we find that for $s = 30$ the eigenstates are mainly located within a single lattice site. This result is of particular interest because it shows that a localization of the particles within one lattice site is possible without a repulsive interaction which was needed in the Mott insulator experiment [45]. Indeed, if an atomic Fermi gas is loaded in this combined potential an occupancy with exactly one atom per lattice site can be achieved due to the localization imposed by the harmonic potential [53].

Another intriguing consequence of the localization is the addressability of single lattice sites. The gradient of the parabolic potential leads to different resonance conditions for an atomic transition in dependence of the lattice site considered. In our setup the magnetic potential leads to a spatially varying Zeeman splitting within the $|F = 2\rangle$ -manifold and thus a very weak radio frequency should allow — in principle — for the manipulation of the atoms within one lattice site. To get a reasonable discrimination and a sufficiently high Rabi frequency, the resonance condition between adjacent lattice sites should be shifted by something about 10 kHz which would require a gradient of 300 G/cm⁵. Thereby a linear potential is more favorable than a parabolic one where the frequency shift is changing along the lattice. For well defined experimental conditions it would be also desirable to have an optical confinement in the radial direction because otherwise particles with lower axial but higher radial energy might also be resonant with the radio frequency.

⁵For this gradient, the required lattice height for a localization within one lattice site and a simultaneous suppression of Zener tunnelling is $s > 10$.

4.4 Insulating behavior of fermionic localized state

So far we have investigated both experimentally and theoretically the stationary states of an atomic gas trapped in a combined parabolic and periodic potential. In this section, we will instead study the response of such a system to an external perturbation. In particular, we look at the center-of-mass oscillation of a Fermi gas when subjected to a sudden displacement of the harmonic trap. To describe the time-evolution of our delocalized/localized states, we adopt a semiclassical approach which provides a more physical insight on the problem. All the measurements reported below are referred to a spin-polarized Fermi gas, well below T_F . Whereas the statistical nature of our atomic sample would not introduce modification on the single-particle energy spectrum, the dynamical properties are strongly affected by possible inter-species collisions acting as a dissipative channel which could carry the system out of localization, as we will show in Chap.5.

For sake of clarity, we will introduce at first the semiclassical model used to describe the system and then our experimental procedure and finding.

4.4.1 Semiclassical model

As already stressed, a spin-polarized Fermi gas is a completely non-interacting system. The many-body Hamiltonian can be thus simply written as a sum of single-particle Hamiltonians (see Sec.4.2). As usual, we restrict ourself to the 1D axial problem to study the dynamics along the lattice. In a semiclassical approach ⁶, the effects of the periodic potential can be taken into account just by a renormalization of the atomic mass ($m \rightarrow m^*$ and thus $\frac{p_x^2}{2m} \rightarrow \varepsilon(p_x)$) while the harmonic confinement generates a driving field. Using this one-dimensional semiclassical model, Eq. (4.1) becomes

$$H_0 = \varepsilon(p_x) + \frac{1}{2}m\omega_a^2 x^2. \quad (4.4)$$

Starting from Eq. (4.4), we are interested on the response of a Fermi gas to a sudden displacement x_d of the harmonic trap center. The new Hamiltonian with the displaced harmonic trap is thus

$$H = \varepsilon(p_x) + \frac{1}{2}m\omega_a^2 (x - x_d)^2. \quad (4.5)$$

⁶This approach can be used provided that the harmonic oscillator length is much larger than the lattice spacing $d = \lambda/2$

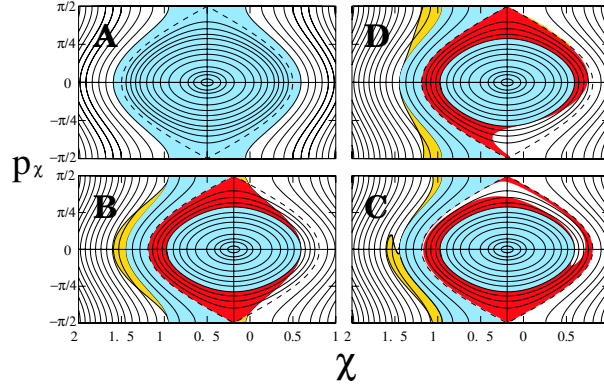


Figure 4.12: Phase trajectories for a trapped 1-D Fermi gas in a lattice at $T = 0$, just before and after the displacement of the trap (figs. A and B, respectively), and their dynamical evolution (figs. C and D). The ordinate and abscissa are in units of $p_\chi \equiv P_x d / 2\hbar$ and $\chi \equiv \sqrt{m\omega_x^2 x^2 / 4\delta}$.

If the displacement x_d is small compared to the size of the atomic cloud, we can neglect the quadratic term in x_d . In the linear regime of perturbation

$$\frac{1}{2}m\omega_a^2(x - x_d)^2 \simeq \frac{1}{2}m\omega_a^2x^2 - m\omega_a^2xx_d, \quad (4.6)$$

and the total Hamiltonian can be written as a sum of the unperturbed and perturbed Hamiltonian:

$$H(x, p_x, t) = H_0(x, p_x) + H_{pert}(x, t). \quad (4.7)$$

Since we suddenly switch on the perturbation at $t = 0$, the perturbed Hamiltonian $H_{pert}(x, t)$ corresponding to this excitation is:

$$H_{pert}(x, t) = m\omega_a^2\Theta(t)xx_d, \quad (4.8)$$

where $\Theta(t)$ is the unit step function. As soon as the parabolic trap is displaced, the center-of-mass $\langle \hat{x}(t) \rangle$ of our gas starts to oscillate in the combined potential. The equation of motion for $\langle \hat{x}(t) \rangle$ can be derived by applying a first order perturbation theory (i.e. linear perturbation) to the well-known Liouville equation

$$\frac{\partial f}{\partial t} + \{H, f\} = 0, \quad (4.9)$$

where $f \equiv f(x, p_x, t)$ is the distribution function of our Fermi gas.

If we consider the unperturbed system, Eq. (4.9) leads to an equilibrium distribution function $f_0(x, p_x)$. In the linear regime of perturbation, we can consider solution of the type:

$$f(x, p_x, t) = f_0(x, p_x) + g(x, p_x, t), \quad (4.10)$$

where $g(x, p_x, t)$ is a small time-dependent correction to the equilibrium distribution f_0 . By introducing the ansatz (4.10) in the Liouville equation (4.9) and expanding the Poisson bracket, one finally finds [131]

$$\frac{\partial g(x, p_x, t)}{\partial t} + \frac{\partial \varepsilon(p_x)}{\partial p_x} \frac{\partial g(x, p_x, t)}{\partial x} + m\omega_a^2 x \frac{\partial g(x, p_x, t)}{\partial p_x} - m\omega_a^2 \Theta(t) x_d \frac{\partial f_0(x, p_x)}{\partial p_x} = 0. \quad (4.11)$$

The Liouville equation becomes thus a differential equation whose solution provides the perturbed density distribution g . Once $f(x, p_x, t)$ is found, one can study the center-of-mass motion of the gas according to the equation

$$\langle \hat{x}(t) \rangle = \int_{-\infty}^{+\infty} dx \int_{-\infty}^{+\infty} dp_x \frac{1}{2\pi\hbar} x f(x, p_x, t). \quad (4.12)$$

The problem is clearly simplified if we deal with a single-band system in tight binding approximation. In this limit, the energy dispersion for a pure periodic potential takes the simple expression

$$\varepsilon(p_x) = 2\delta \sin^2\left(\frac{p_x d}{2\hbar}\right), \quad (4.13)$$

where $d = \lambda/2$ and 2δ is, as usual, the bandwidth. If one introduces Eq. 4.13 in the Liouville equation, it is possible to find $f(x, p_x, t)$ and thus the evolution of the center-of-mass. However, one can also extract several useful information by looking at the energy E of the system. In particular, one can get the isoenergetic trajectory diagram in phase space. In presence of the parabolic potential, the energy

$$E = 2\delta \sin^2\left(\frac{p_x d}{2\hbar}\right) + \frac{1}{2} m\omega_a^2 x^2 \quad (4.14)$$

is a constant of motion, i.e. no dissipative mechanism is present in our non-interacting system. One can thus draw the isoenergetic orbits in the (x, p_x) plane. Such a single particle orbits are reported in Fig. 4.12, for our experimental parameters. We can distinguish two different kinds of trajectories corresponding to the two classes of states found by solving numerically the full-Hamiltonian (4.2). These two kinds of orbits are separated by the dashed orbit with energy $E = 2\delta$. A particle with energy within the first band ($E < 2\delta$) occupies a *closed* orbit in the phase space. A fermion, moving in such a trajectory, starts to oscillate in x -space around the trap minimum as soon as the harmonic trap is shifted. Indeed, in closed orbits, the kinetic energy can be fully converted in potential energy and viceversa. In the full many-body approach (see Sec. 4.2.1), a particle in a closed orbit corresponds to the delocalized particle, described above. On the contrary, if $E < 2\delta$ a localization take place and particles move in phase space along *open* orbits which are the semiclassical analogous of localized states. Particles in these open orbits can just oscillate on one side of

the potential without passing through $x = 0$. The kinetic energy can never be completely converted in potential energy. Localized oscillations are equivalent to Bloch oscillations observed when a linear driven potential is applied, as we have shown in Chap. 3.

Note that, in general the oscillation frequency of both kinds of orbits shows a strong dispersion with energy.

As shown in Fig. 4.12A, the Fermi gas at $T = 0$ uniformly fills the phase space region with energy below E_F . A sudden displacement of the center of the harmonic potential corresponds to a shift of the center of the phase space (see Fig. 4.12B). The blue region contains particles that are still in equilibrium in the new configuration of the trapping field. The red and yellow regions, containing particles moving on close and open orbits respectively, are instead out of equilibrium and give rise to a collective dipole motion. The phase space region opens and melts during the dynamics as a consequence of the energy dependence of the single particle oscillation frequency (see figs. 4.12 C, D), yet leaving constant the phase space volume (because of the Liouville theorem) and therefore preserving the Pauli principle.

As we will discuss in next section, the center-of-mass motion of the Fermi gas is damped due to dephasing between atoms. In particular, red orbits dephase on a longer time scale with respect to the yellow ones. Therefore, the relaxation and the frequency of the oscillation mode are dominated by the particles moving around the center of the phase space, in the red region. Note that yellow orbits remain open during all the system evolution. This leads to a trapping the center of mass of the system on one side of the harmonic potential.

In the one-dimensional semiclassical model, the damping of the oscillation disappears in the linear limit (small initial displacement) at $T=0$. To describe the dynamics of the Fermi gas produced in our experiment, we need a three dimensional model [50]. The step described above to derive the center-of-mass motion can be extended to the 3D case. A full description can be found in [131].

4.4.2 Center-of-mass dipolar oscillation

We now report on the observed behavior of a Fermi gas when the harmonic trap minimum is shifted in the direction of the lattice. We also compare our finding with the 3D semiclassical model developed by S. Stringari and coworker [131, 50].

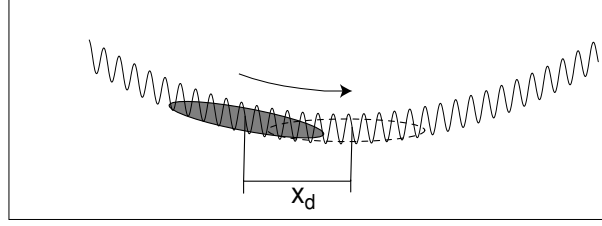


Figure 4.13: Sketch of the experimental procedure to induce a dipolar oscillation in the combined periodic and harmonic potential.

Experimental procedure

All the measurements reported below are performed with a Fermi gas in the combined harmonic and periodic potential. Our sample is composed typically by 2.5×10^4 atoms of ^{40}K at a temperature that can be varied between $0.2 T_F$ and T_F , where the Fermi temperature is $T_F \approx 300$ nK. The lattice has here a wavelength of 863 nm. The lattice height can be adjusted in the range $U = 0.1 - 8E_R$, where $E_R/k_B = 317$ nK. To excite a dipolar mode, we displace the harmonic trap minimum along the axial direction [132], as illustrated in Fig. 4.13. The cloud is thus out of equilibrium and start to oscillate. The typical displacement is $x_d = 15 \mu\text{m}$ which is much smaller than the $1/e^2$ radius of the cloud ($110 \mu\text{m}$). After a variable evolution time in the trap the atoms are released from the combined potential. We detect the position of the center of mass of the cloud by absorption imaging after a ballistic expansion of 8 ms.

The figure (4.14) shows the dipolar oscillation of the Fermi gas both in presence of a lattice with $s=3$ (solid circles) and with a pure harmonic trap (open circles). Together with our experimental data, we also report the theoretical prediction of the semiclassical theory (solid line) which well describes our finding. The comparison between these two set of measurements reveals the strongly modified behavior of the system when an optical lattice is switched on. In presence of the lattice, an offset appears in the oscillations. According to the above discussion on the phase space, we ascribe this offset to the significant fraction of particles moving along open orbits. For the given parameters the Fermi energy is indeed larger than the bandwidth $2\delta \approx 0.4E_F$. This localized fraction of fermions behaves macroscopically as an insulator, because its center of mass does not move under the harmonic force but stays trapped on one side. The fraction of the gas occupying closed orbits can instead oscillate in the harmonic potential, and has therefore a conducting nature. A damping appears as expected because of the dephasing between different orbits. Also, the oscillation frequency is reduced because of the larger effective mass of the atoms in

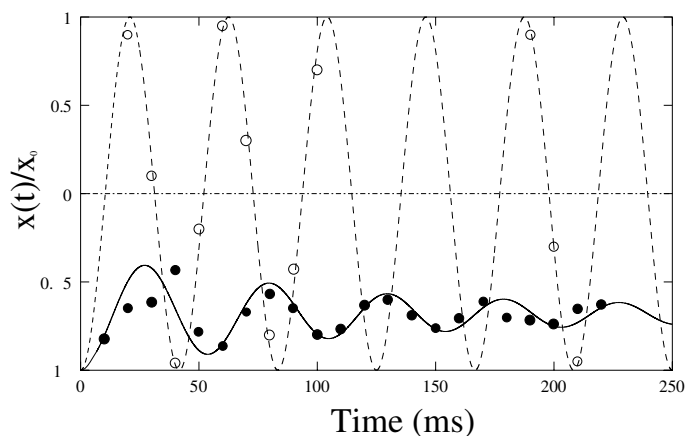


Figure 4.14: Dipole oscillations of the Fermi gas of ^{40}K atoms at $T = 0.3T_F$ in presence (filled circles and full line) and in absence (empty circles and dotted line) of a lattice with height $s = 3$. The lines are the theoretical predictions, the circles are the experimental results. The horizontal dot-dashed line represents the trap minimum.

the lattice. As discussed in Sec. 4.4.1, a fermion can oscillate or stays trapped in one side of the potential whether its energy is smaller or larger than 2δ . Experimentally we can adjust 2δ by changing the height of the optical potential. In this way the Fermi energy moves within the energy gap between the first and second band of the lattice. We have therefore performed a series of measurements by keeping the atom number and temperature of the Fermi gas constant, and varying just the lattice height. In Figs. 4.15-4.16 we plot the measured dependencies of the offset, damping rate and oscillation frequency from the lattice height s . In particular, Fig. 4.15 shows the crossover from a conducting behavior in low lattices (most of the fermions has an energy $E < 2\delta E$) to an almost completely insulating behavior in higher lattices ($E > 2\delta E$). The relative oscillation offset defined as x_{osc}/x_0 , where x_{osc} is the center of oscillation of the system in the lattice, increases by increasing the lattice height. Note how the relative offset, which represents the insulating fraction of the Fermi gas, stays small as long as $2\delta < E_F$, and then raises quite rapidly towards unity. Since in the present experiment $E_F \approx E_R$, an insulating fraction appears already with low lattices; the theory however shows that the threshold for the insulation moves to higher lattices in case of smaller Fermi energies (dashed line in Fig. 4.15). The disagreement between experiment and theory at low lattice heights, $s < 3$, can arise from the population of higher bands due to the finite temperature and/or Landau-Zener tunnelling. Indeed, the semiclassical model is built up in single-band approximation. Increasing s , the energy gap between bands increases, and the single band calculations become

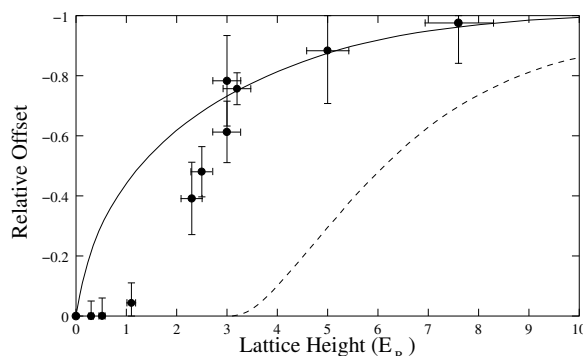


Figure 4.15: Relative offset of the oscillations of a Fermi gas in the lattice (normalized to the initial displacement) as a function of the lattice height. The circles are the experimental data and the continuous line is the theoretical prediction for 3×10^4 atoms at $T = 100$ nK. The dashed line is the prediction for a Fermi gas of 2.5×10^3 atoms at $T=0$.

more realistic. In Fig. 4.16 we instead show the observed features of the conducting fraction of the gas. The damping rate of the oscillation (Fig. 4.16a) also increases with the lattice height, because of an increased dispersion of the oscillation frequencies of atoms in closed orbits⁷. In Fig. 4.16b, we report the oscillation frequency of this oscillating which is close to that expected for a particle moving at the bottom of the band with a renormalized mass.

As a consequence of the Pauli principle, which keeps the energy distribution broad, a spin-polarized Fermi gas exhibits an insulating behavior even at $T=0$. Note that the phenomenology observed with a Fermi gas only weakly depend on the gas temperature, at least in the region $0.2-1 T_F$ that we have explored so far in both experiment and theory, and in general we observe an increase of both offset and damping for increasing temperatures, as expected because of the broader energy distribution. As we will see in Chap. 5, this behavior is somehow opposite to the one exhibited by thermal bosons in which interparticle collisions enhance the conduction into the system.

4.5 Delocalized states: Bose-Einstein condensate

The Pauli principle keeps the energy distribution of spin-polarized fermions broads in the combined potential even at zero temperature. As a consequence, in tight bind-

⁷fermions are in several closed orbits corresponding to different oscillation frequencies which contribute to the dipole motion in different way

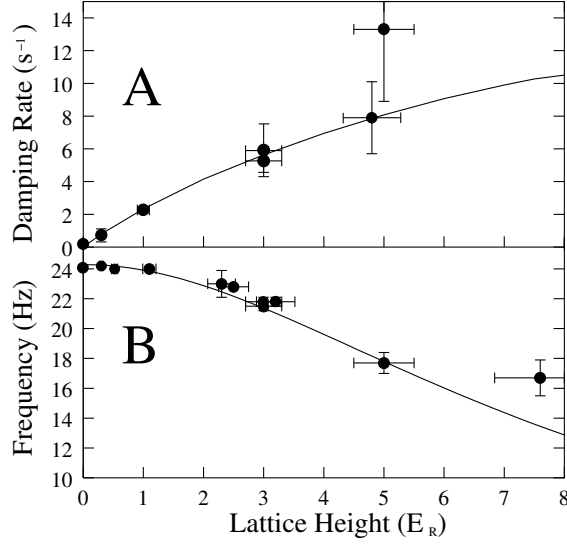


Figure 4.16: A) Comparison between theory (line) and experiments (circles) for the damping rate of the dipole oscillations of the Fermi gas as a function of the lattice height. B) Oscillation frequency of the Fermi gas as a function of the lattice height. The line is the expectation for a particle oscillating at the band bottom.

ing regime, a fraction of fermions will always occupy localized states while the other fraction will remain in delocalized ones. The dynamics of the whole system is thus affected by both components which behave differently, as discussed in the previous section. To investigate the transport properties of just delocalized state, i.e. to probe the renormalization-mass theory, a good approach is to use a Bose-Einstein condensate as atomic sample. Indeed, due to its narrow distribution in both momentum and coordinate space, condensed bosons occupy only energy levels with $E < 2\delta$ (delocalized states) experiencing a harmonic potential with a frequency modified by the presence of the lattice [128, 129].

To confirm this expectation we have studied the modification of the low-lying collective modes of a harmonically trapped BEC due to the presence of a 1D periodic potential. In particular, we examine the axial dipole and quadrupole mode. In the unperturbed system, these excitations correspond respectively to the eigenfrequencies $\omega_D = \omega_a$ and $\omega_Q = \sqrt{\frac{5}{2}}\omega_a$ [14], as comes out from the hydrodynamics equation of a superfluid [133]. Stringari and coworkers have shown that the hydrodynamics equation can be still applied also in presence of an optical lattice. This extension is possible by substituting the atomic mass m with an effective mass m^* which ac-

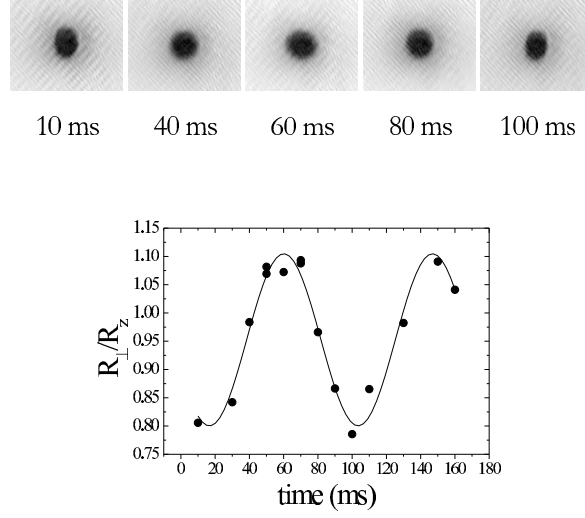


Figure 4.17: In the upper part we show absorption images taken after exciting the quadrupole mode of a condensate in the combined trap with $V_{opt} = 3.4 E_r$ and waiting different evolution times (10,40,60,80 and 100 ms) before switching off the trap and letting the cloud expand for 29 ms. In the lower part we show the evolution of the Aspect Ratio (R_{\perp}/R_z) of the condensate obtained from the absorption images together with a sinusoidal fit to extract the frequency of the mode.

counts for the modified inertia of the gas due to the lattice. In the linear regime of small amplitude oscillations, the new frequencies in presence of an optical lattice are simply obtained by replacing the axial magnetic trap frequency ω_a with $\omega_a \sqrt{m/m^*}$:

$$\begin{aligned}\omega_D &= \sqrt{\frac{m}{m^*}} \omega_a \\ \omega_Q &= \sqrt{\frac{m}{m^*}} \sqrt{\frac{5}{2}} \omega_a.\end{aligned}\tag{4.15}$$

Note that, modes occurring in the direction perpendicular to the one of the optical lattice are clearly unaffected by the lattice. In our experiment, we can directly test this theory by measuring the frequency of the dipole and quadrupole mode as a function of the optical potential depth s .

Dipole and quadrupole mode

To perform measurements on these low-lying excitations, we employ a Bose-Einstein condensate of ^{87}Rb atoms in $F = 1, m_F = -1$. The axial and radial frequencies of the harmonic trap are now $\omega_a = 2\pi \times 8.70$ Hz and $\omega_r = 2\pi \times 85.7$ Hz, respectively.

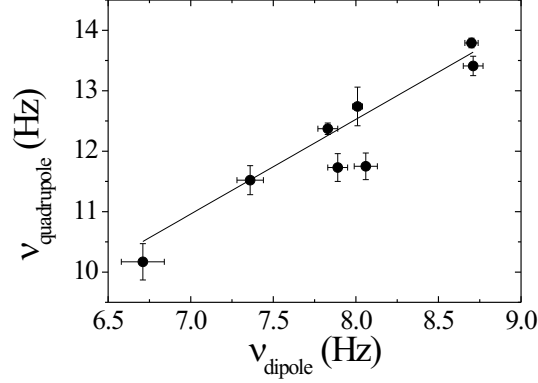


Figure 4.18: Frequency of the quadrupole mode of a condensate trapped in the combined potential (harmonic magnetic trap + 1D optical lattice) as a function of the dipole mode frequency measured for different values of the optical lattice depth from $0 E_r$ to $4.1 E_r$. The frequencies of both the modes, characterized by a dynamics along the optical lattice, show a marked dependence from the optical potential depth. The line represent a linear fit with a slope of 1.57 ± 0.01 .

The wavelength of the optical lattice is chosen to be far detuned with respect to all the atomic transition ($\lambda = 757 \text{ nm}$).

We induce a dipolar oscillation, by suddenly displacing the position of the trap minimum along x and observing the center-of-mass motion as a function of time [39]. Typical initial displacement used is $\sim 30 \mu\text{m}$. The quadrupole mode is instead excited by perturbing the magnetic bias field [134]. This is done by applying five cycles of resonant sinusoidal modulation at a frequency close to $\sqrt{5/2}\nu_D$. The quadrupole mode is a zero angular momentum mode corresponding to an in-phase oscillation of the width along the radial direction and an out-of-phase one along x . Typical quadrupole oscillation is represented in Fig. 4.17 where, in the upper part, we show images of the expanded condensate taken at different times after the excitation procedure and in the lower part we report the measured aspect ratio together with the sinusoidal fit. Since ν_D and ν_Q are expected to scale in the same way with the optical potential depth (see Eqs. (4.15)), we report in Fig. 4.18 the quadrupole mode frequency as a function of the dipole mode frequency varying the lattice heights. From a linear fit of the data we obtain a slope of 1.57 ± 0.01 in very good agreement with the theoretical prediction of $\sqrt{5/2} = 1.58$. These measurements demonstrate that the transport properties of a trapped BEC in the presence of a periodic potential can

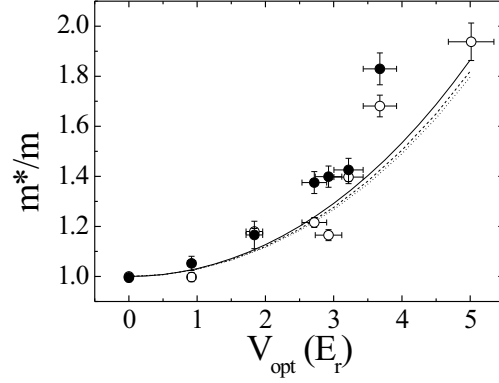


Figure 4.19: Effective mass values extracted from the dipole mode frequency (open circle) and from the quadrupole mode frequency (closed circle) as a function of the optical lattice height. The continuous line represent the theoretical curve from [128] obtained neglecting the role of the mean field interactions, while dashed and dotted lines corresponds to the values obtained in [135] numerically solving the Gross-Pitaevskii equation and evaluating the effective mass from the quadrupole and the dipole mode frequencies.

be described generalizing the hydrodynamic equations of superfluids.

Following Eqs. (4.15), from our data we can also extract the value of the effective mass m^* as a function of V_{opt} . The results obtained from both the dipole mode and the quadrupole mode frequencies are reported in Fig. 4.19, together with the theoretical predictions reported in [128] (continuous line). Even if this theoretical curves have been obtained neglecting the mean field interaction and the magnetic confinement, the agreement with our data is very good. In fact, in the regime of V_{opt} explored in our experiment, the effect of interactions is negligible as also confirmed by the direct solution of the Gross-Pitaevskii equation (dashed and dotted line in Fig. 4.19) [135]. For "large" amplitude oscillation, the system shown an instability resulting from the interplay between dispersion and nonlinearity [127, 136, 137].

Chapter 5

Conduction of a Fermi gas in the combined potential

Analogy denotes a resemblance not between things but between the relation of things.

W. S. Javons

In the previous Chapter, we have investigated the features of a non-interacting atomic Fermi gas in a combined periodic and harmonic potential. In particular, we have demonstrated both experimentally and theoretically that such combined potential admits two different classes of solutions, named delocalized and localized states. Under an external driven force, fermions in localized states act as an insulator system. This result provides a straightforward link with the well-known theory of conduction in metals. Indeed, electrons subjected to a linear potential occupy localized Wannier-Stark states (see Chap.2) and this localization yields again to an insulating behavior. In the absence of interactions, electrons in Wannier-Stark state cannot change their quantum state and the whole system behaves like an insulator for DC currents. However, this scenario is far from the real physical situation encountered in metals in which electrons strongly interact with lattice phonons and impurities. Indeed, the localization is somehow "destroyed" by collisional mechanism and a macroscopic current is established. In particular, at the onset of interactions, an increasing collisional rate is expected to favor a current through the lattice whereas at high collisional rate the current is hindered by collisions. The latter regime is the usual one for solids where the conductivity decreases linearly with increasing collisional rates while the limit of low collisional rate, where the role of collisions is reversed, is experimentally not accessible in solids. Nevertheless, this regime can be achieved by employing

semiconductor superlattices which exhibits the spectacular phenomena of negative electric conductivity [138, 139, 140, 141].

The aim of our experimental work reported here is to study the transport of a Fermi gas subjected to an external force when collisional channel is present (i.e. bosons). This investigation allows us on the one hand to go further in the comparison of our atomic system with a solid state one and on the other hand gives the possibility to reach low-collisional regime not accessible in the physics of solids. For sake of clarity, we summarize below our main results while a detailed discussion can be found in the sections.

5.1 Outline

In this Chapter, we move from an ideal Fermi gas, already described in Chap. 4, to a cloud of fermions interacting with a Bose gas (Sec. 5.2.1). We observe that the behavior of our Fermi gas changes dramatically in presence of the dissipative channel provided by collisions with bosons. In particular we will show that, under an external driven force, a dc fermionic current can be established only in presence of interactions (Sec. 5.2.2). Furthermore, the dependence of the transport velocity on the collisional rate gives evidence of the two regimes of negative and positive conductivity already expected but never observed in metals. Finally, we also report the comparison of our findings with a model first introduced for electrons in superlattices which reveals the importance of dissipative mechanism on the transport (Sec. 5.2.3).

The main results reported here can be found in our publication:

- "*Collisionally Induced Transport in Periodic Potentials*", H. Ott, E. de Mirandes, F. Ferlaino, G. Roati, G. Modugno, and M. Inguscio, Phys. Rev. Lett. **92**, 160601 (2004).

5.2 Transport of localized states assisted by collisions

5.2.1 Experimental procedure

The experimental procedure to produce a mixture of ultra cold fermionic ^{40}K and bosonic ^{87}Rb atoms in a combined periodic and harmonic potential has been already described in Sec. 1.3.1 and 4.2.2.

All the measurement reported below are carried out with mixture of fermions and bosons at temperatures between 300 and 400 nK. The number fermions can be varied

between 2×10^4 and 10^5 which corresponds to a Fermi temperature of 300 – 400 nK. Since we want to add interspecies collisions in a controllable way, we need to adjust the number of bosons in the mixture by changing the final ramp of the radio frequency evaporation. We can also remove bosons using a sweep below the trap bottom. Note that the temperature of the mixture is always above the critical temperature for Bose-Einstein condensation. We use a laser light to produce the lattice with a wavelength $\lambda = 830$ nm, corresponding to a recoil energy $E_r = \hbar^2 k^2 / 2m \simeq 160$ nK, in unit of k_B . Since we want to study the evolution of localized states in presence of a collisional mechanism, the temperature of the samples is chosen to be comparable to the recoil energy which yields a significant occupation of the localized states. The typical $1/e^2$ -radius of the cloud in the direction of the lattice is $100 \mu\text{m}$ corresponding to roughly 250 lattice sites. We remind that, in the two radial directions, the atoms occupy the radial harmonic oscillator states.

In order to study the transport of the particles along the lattice, we excite a dipolar mode in the Fermi gas. The magnetic trap is thus suddenly shifted in the direction of the lattice by a fraction of the extension of the cloud (displacement x_d). As already discussed in Sec. 4.4, the harmonic confinement acts like an quadratic driving potential (see Fig. 4.13). Finally, we monitor the dynamic of the Fermi gas by taken absorption images of the cloud for different holding times in the combined potential and we obtain the center-of mass (CM) position of the cloud by fitting the observed atomic distribution.

5.2.2 Center-of-mass dipole oscillations

The evolution of the CM for an initial displacement of $x_d = 35 \mu\text{m}$ is shown in Fig. 5.1b. The open circles show the motion of a pure fermionic sample. The filled squares show the evolution of the fermionic sample in the presence of 10^5 bosons. As showed in Sec. 4.4, non-interacting fermions in a combined potential behave as an insulator (open circles) and their evolution is characterized by the following features:

1. Offset: The offset is due to fermions in localized states (open orbits) which stay trapped in one side of the potential after the displacement. These fermions can not change their quantum state since any dissipative mechanism is absent.
2. Damping: The damping is due to fermions which still occupy delocalized states (closed orbits) and can thus oscillate until dephasing mechanism washes out the motion. The dephasing, which set the timescale of the damping, arise from the different frequencies of fermions in different orbits.

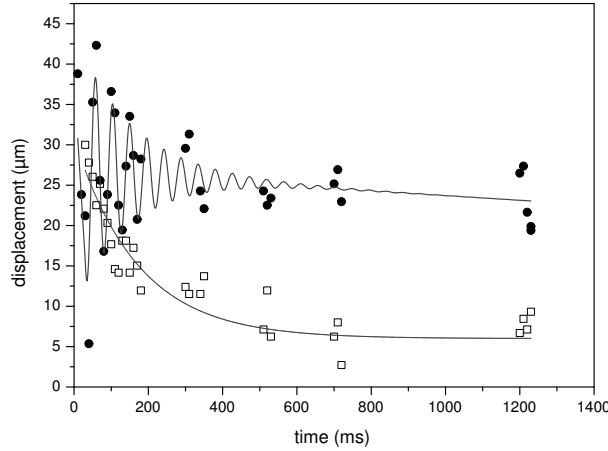


Figure 5.1: Evolution of the center of mass (CM) position of a cloud of fermions. A pure fermionic sample (circles) does not move to the trap center, whereas an identical sample with an admixture of bosons reveals a current through the potential (squares). The data are fitted with a sum of an exponential decay and an initial damped oscillation as described in the text (continuous lines). The expansion time of the cloud is 8 ms and the lattice height is $s = 3$. The temperature and the atom number of the fermions are $T = 300$ nK and $N = 5 \times 10^4$, the number of admixed bosons is $N_B = 1 \times 10^5$.

3. Frequency: The oscillation frequency of delocalized fermions is reduced with respect to the trap frequency due to the large effective mass experienced by atoms in the lattice.

Note that for such a non-interacting system, only Landau-Zener tunnelling would be able to modify the behavior of localized atoms. Nevertheless, for our experimental parameter, this effect is negligible. The offset cannot vanish and the system is insulating.

As soon as we introduce in the system a mechanism which allows fermions to change their quantum state, the dynamical behavior of the gas strays dramatically from the one just illustrated. We add to the system a cloud of bosons which interact attractively with the Fermi gas. Interspecies collisions allow the fermions to hop between different localized states. The fermions rapidly move towards the equilibrium position of the potential ¹. This macroscopic transport corresponds to a DC current. To quantify this current, we fit an exponential decay to the long time tail of the data. For fermions in the mixture we find a decay time of $\tau = 260 \pm 30$ ms, whereas for the

¹Due to a heating of the radial degrees of freedom the axial extension of the cloud in the mixed system increases. Because an existing anharmonicity of the trapping potential shifts the center of mass for increasing temperatures, the cloud remains slightly above the equilibrium position.

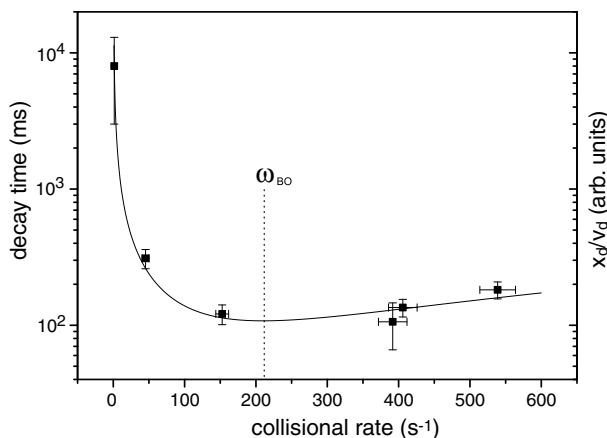


Figure 5.2: Decay time τ of a cloud of fermions in a mixture with bosons in dependence on the collisional rate (dots). The number of fermions is $N = 50\,000$ with a temperature of 350 nK . The number of bosons was changed over more than one order of magnitude. The lattice height for the two species was $s_K = 3$ and $s_{Rb} = 9$, the initial displacement was $x_d = 35\ \mu\text{m}$. The solid line is a drift time, calculated from Eq. (5.1) for a linear potential with Bloch oscillation frequency $\omega_B = 2\pi \times 35\text{ s}^{-1}$ (see text). For comparison, the theoretical curve is multiplied with a factor of three.

pure fermionic sample the decay time is longer than 5 s which is comparable to the lifetime of the atoms in the optical potential. This experiment proves that in a perfect lattice interactions between the particles are needed to establish a macroscopic current under an external force.

5.2.3 The Esaki and Tsu theory works here ?

Fig. 5.1 clearly shows that collisions with bosons drive the Fermi gas toward a local equilibrium into the minimum of the potential. To investigate this mechanism in more detail, we can repeat the same experiment for different number of bosons in the mixture which also yields to a change in the collisional rate. In Fig. 5.2 we report the decay time of the offset of the fermionic cloud as a function of the collisional rate. The number of bosons is changed from 2.5×10^4 to 3×10^5 corresponding to a change in the interspecies collisional rate between 40 s^{-1} and 550 s^{-1} . The average collisional rate is calculated taking into account the spatial overlap of both clouds in the combined potential. Increasing collisional rate, we observe a faster decay of the offset which corresponds to a decrease of the decay time. This is what one expects if the collisions assist the hopping between different localized states. For high collisional rates, the experimental data show a slight increase of the decay time with

increasing collisional rate. In this regime the number of bosons is much higher than the number of fermions and the bosons can be regarded as a thermal bath for the fermions. The fermions exhibit a drift motion and the collisions with the bosons impede the current through the potential like in a electric conductor.

A similar behavior has been observed in semiconductor superlattices [138, 139]. Differently from usual metals, the period of a superlattice turn out to be smaller than the electron mean field path. One may expect to observe in these systems strong energy dispersion effects which are hidden by collisional mechanisms in common metals. In semiconductor superlattices, the current through the potential decreases when the applied voltage is increased and the system exhibits a negative differential conductivity (NDC). This is due to the tighter localization of the electron wave function which reduces the transition probability of a hopping event between the localized states [142, 143]. In our experiment, we do not change the transition probability between quantum states but the rate of transition inducing collisions. Despite the different physical mechanism, the drift velocity depends only the product of the Bloch frequency ω_B , i.e. the transition probability, and the collisional rate determines the final hopping rate. This formal identity allows us to compare our experimental data with the theoretical model that was introduced by Esaki and Tsu [138] to describe NDC. The authors calculate the drift velocity of electrons in a periodic potential under a constant external force. They introduce a phenomenological scattering rate γ (relaxation-time approximation) and show that the drift velocity depends on the ratio of the Bloch oscillation frequency in the linear potential ω_B and the scattering rate γ :

$$v_d = v_0/4 \frac{\omega_B/\gamma}{1 + (\omega_B/\gamma)^2}, \quad (5.1)$$

with $v_0 = \lambda\Delta E/\hbar$ being the tunnelling speed through the potential and ΔE being the width of the first band. A direct adaptation of the above equation to our dynamics is rather complicated because we have a spatially varying Bloch oscillation frequency $\omega_B(x)$ and an inhomogeneous system. Note that the spatial dependence of the Bloch frequency arises from the driven force applied which is linear in space rather than constant ($F = m\omega_a^2 z$ and $\omega_B(x) = F(x)d/\hbar$). However, we can compare the initial velocity v_i of the center of mass observed in the experiment with the drift velocity calculated from Eq. (5.1) for a uniform system in a linear potential. To determine the Bloch oscillation frequency in this potential, we take the force that initially acts on the center of mass after the displacement and we identify the scattering rate γ with the average collisional rate between the fermions and the bosons. Because the initial velocity of the center of mass is connected to the decay time of the offset by

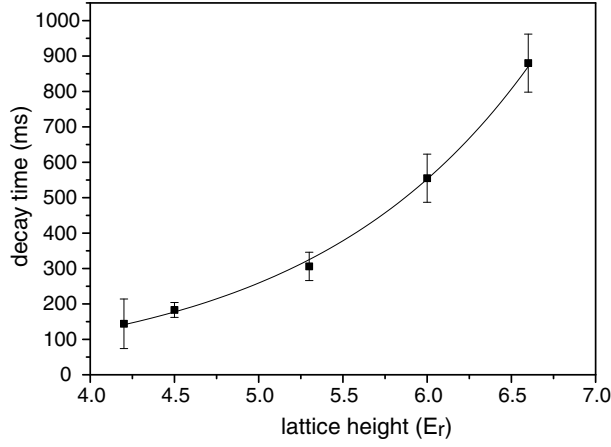


Figure 5.3: Decay time of a cloud of bosons for different lattice heights. The initial displacement was $x_d = 10 \mu m$. The continuous line is an exponential fit to the data. The exponent is given by $e^{-s/1.6}$.

$\tau = x_d/v_i$ we can also compare the decay time τ with the inverse of the drift velocity v_d . The curve arising from Eq. 5.1 is shown in Fig. 5.2 (solid line).

The issue of the identification of our damping mechanism with the one considered in the Esaki and Tsu model deserves some discussion. In semiconductor superlattices, the phenomenological scattering rate γ describes dissipative scattering processes, where the electrons can arbitrarily exchange energy and momentum with an external thermal bath, such as a bath of lattice phonons. In our system, the only scattering process present is due to collisions between fermions and bosons. Indeed no energy exchange with the lattice is possible because our optical lattice is free of impurities or excitations and momentum can only be transferred to the lattice in multiples of the Bragg momentum via umklapp scattering processes. Nevertheless, in the limit $N_B > N_F$, bosons can be regarded as a thermal bath providing a dissipative scattering channel. For small numbers of admixed bosons and for pure bosonic samples, where the assumption of having a thermal bath is questionable, we find however the same phenomenology predicted by the NDC model. This indicates that also in this case a dissipative mechanism is still present, possibly related to the coupling to the two radial degrees of freedom. We can conclude that, in spite of the simplifications and differences, the Esaki-Tsu model for semiconductor superlattices reproduces well our experimental finding for an atomic Fermi gas interacting with a Bose gas in a combined periodic and parabolic potential.

5.2.4 Decay and localization

From the above discussion comes out that the transport properties of our Fermi gas are determined by the competition between localization and collisions. In Sec.4.3.2, we have shown that the degree of localization increase with the lattice height s (see Fig. 4.11). We now demonstrate that, for a given sample of bosons, the transport of fermions into the combined potential, is slowed down by increasing s . At this purpose, we have measured the dependence of the decay time on the lattice height s . Our findings are reported in Fig. 5.3. The data show a rapid increase of the decay time with increasing lattice height. This can be explained with a reduction of the tunnelling probability between neighboring lattice sites with increasing lattice height. In expression (5.1) the tunnelling speed appears as a scaling factor for the drift velocity. Even if one takes into account a spatially varying Bloch oscillation frequency $\omega_B(x)$ and an inhomogeneous scattering rate $\gamma(x)$, the role of v_0 does not change. Thus, we can write for each single particle a differential equation of the form $\dot{x}/v_0 = f(\omega_B(x), \gamma(x))$, whose solution scales in the time domain with v_0 . Consequently, also the behavior of the center of mass scales with v_0 and the decay time must be proportional to the inverse of the bandwidth. For a sinusoidal potential, the bandwidth can be expressed in terms of Mathieu functions and we find that for $s < 10$ the bandwidth is well described (the maximum error is smaller than 10 percent) with an exponential drop of the form $\Delta E = E_T e^{-s/3.8}$. One therefore expects an exponential increase of the decay time with increasing lattice height. The exponential fit in Fig. 5.3 demonstrates well that this dependence is accomplished. We find a numerical value for the factor in the exponent of the fit of 1.6. For other experimental data sets with different temperatures and initial displacements we derive values ranging from 1.5 to 4.5.

All the results reported in this Chapter allow us to conclude that two crucial processes are needed for the macroscopic transport through a periodic potential in the presence of an external force. The first one is the tunnelling from one lattice site to the next one. However, the coherent nature of the tunnelling process leads to a localization of the particle. Therefore an additional dissipative process is needed to destroy the localization of the particle wave function. If one of these two mechanisms is missing, the system is insulating, as we observe it for non-interacting fermions and in the limit of deep lattices.

Conclusions

In this thesis, we concentrate our attention on the behavior of a non-interacting atomic Fermi gas in presence of an one-dimensional optical lattice. A Fermi gas is already interesting in its own right, including an optical lattice makes the system even richer. Our domain of investigation ranges indeed from single-particle coherence effects such as Bloch oscillations to localization effects, and transport phenomena triggered by collisional mechanisms.

Two sets of experimental studies have been reported in the thesis. The first concerns the development of a new atomic interferometer scheme which exploits the absence of interactions in a spin-polarized Fermi gas. The second involves the study of localization effects arising when the periodicity of the lattice is modified by superimposing a parabolic confinement, and the destruction of such localization when the Fermi gas is coupled with a collisional channel.

We have demonstrated an atom interferometer using identical fermions confined by a one-dimensional optical lattice aligned along the gravity. We have shown that the evolution of the interference pattern is the analogous of the semiclassical Bloch oscillation. The forces applied on the atomic sample can be directly determined by the frequency ω_B of such oscillation. The novelty of our scheme consists in employing a non-interacting Fermi gas. The absence of interactions allows to follow the time-evolution of the interference for a long time (more than 100 periods), whereas in a condensate the interference is very rapidly washed out by the interactions. As an example, we have determined the local gravitational acceleration g using both a Fermi gas and a Bose-Einstein condensate. The comparison between these two values reveals at list a one order of magnitude higher precision using a fermionic sample, which could be however improved in future experiment. Our measurements demonstrate an interferometric scheme based on trapped fermions which provides a high-precision accessible just with Bose-Einstein condensate in free-expansion. As a consequence, our method gives the unique possibility to achieve a sensitive determination of forces with high spatial resolution. Possible applications are the study

of forces close to surfaces and at the sub-millimeter scale where a modification of newtonian gravity could be present [123].

In the second part of the thesis, we have investigated both the ground state and the transport properties of our Fermi gas in presence of a combined periodic and parabolic potential. We have observed that an inhomogeneous periodic potential exhibits a qualitatively different phenomenology compared to a homogeneous system. As soon as the translational invariance is destroyed by adding the parabolic potential, the atoms can stay localized out of the minimum of the combined potential. In particular, we have shown that two different classes of states exist: delocalized and localized states. We have developed a technique based on a radio frequency field which induces spatially resolved transitions to remove selectively delocalized particle. This technique allowed us on the one hand to get an evidence of a new localization mechanism which is independent from the interaction, and on the other hand to demonstrate a scheme to spatially address particles. Going further with our investigation, we have induced a center-of-mass dipolar motion on the system by displacing the parabolic potential. We have observed a dramatic difference between the dynamical response of delocalized and localized atoms which behave as a conductor and as an insulator, respectively. The conducting-delocalized fermions perform dipolar oscillations around the trap minima, while the insulating-localized ones stay trapped on one side of the combined potential. Indeed, localized fermions can move into the combined potential just by changing their energy level. In absence of interactions, fermions can not hop between different states due to the conservation of energy and the center-of-mass of the cloud remains pinned out of the equilibrium position. As soon as an interaction is introduced in the system, we have observed a DC atomic current of localized fermions mediated by collisions. In particular, we have observed that fermions rapidly move towards the equilibrium position of the potential. We have investigated the dependence of the transport velocity on the collisional rate and on the lattice height. A comparison with the semiclassical Esaki and Tsu model [138] introduced for electrons in superlattices reveals a good qualitative agreement although the microscopic dissipative mechanism is different.

Our experimental investigation represents the first study on a Fermi gas in a combined parabolic and periodic potential. Our results could open different perspectives for future investigations and applications. First of all, recent theoretical studies predict the existence of an *exotic* quantum phases diagram which involve interacting fermions in a three-dimensional lattice [144, 145]. A Mott insulator scheme has also been recently proposed by using such a interacting system [45]. Furthermore, the

existence of a localization in a non-interacting Fermi gas suggests the possibility to create a single lattice occupancy which has important implications in the field of quantum computing for the implementation of a qubit register [53]. Our spectroscopic technique to address selectively localized particles could also be extended to manipulate particles in single lattice sites which would constitute a major progress in "quantum engineering" with ultra cold atoms. Moreover our studies on the transport of a non-interacting Fermi gas constitutes above all the foundations for further investigations on interacting Fermi gas in an optical lattice. Using fermions in two different spin states and Feshbach resonances to tune their interaction, one could indeed reach both normal and superfluid phase. The achievement of this latter regime is exactly our main goal for future experiments !. In the superfluid phase, one indeed expects a clear modification on the transport along the lattice in analogy with superfluid Josephson-like oscillations already observed with a Bose-Einstein condensate [39]. The optical lattice could thus play the important role of probe for the superfluidity [146, 147].

Appendix A

Calibration of the optical lattice

From an experimental point of view, the calibration of the lattice constitutes an important and ticklish question since most of the measurable quantities depend on the lattice depth. A precise tool to measure the effective optical potential is provided by Bragg diffraction of atoms from a grating of laser light. Usually, Bragg scattering is referred to the diffraction of an electromagnetic wave interacting with a crystal of ions. The underlying physical mechanism of Bragg diffraction embed in a quantize transfer of the momentum between a photon and a ion of the crystal. A photon can indeed transfer to the crystal just a momentum which satisfies the following relation:

$$n\lambda = 2d\sin(\theta), \quad (\text{A.1})$$

where d is the distance between different plane of the crystal and n is the order of the diffraction.

In our case the roles are somehow reversed: we study the momentum transferred between a matter wave (for instance a BEC or a Fermi gas) and a grating of light. Due to its optical nature, Bragg diffraction can be also viewed in term of a two-photons transition from a initial ground state to a final ground state with opposite momentum ¹. This provides a close connection with a Raman transition where an atom oscillates between this two momentum states with an effective Rabi frequency

$$\Omega_{Rabi} = \frac{\Omega_1\Omega_2}{2\delta}, \quad (\text{A.2})$$

where $\Omega_1 \simeq \Omega_2$ are the frequencies of the two transitions and δ the detuning with respect to the atomic resonance. It is possible to show that from Eq. (A.2) one can

¹A n -order Bragg diffraction corresponds to a $2n$ photons transition.

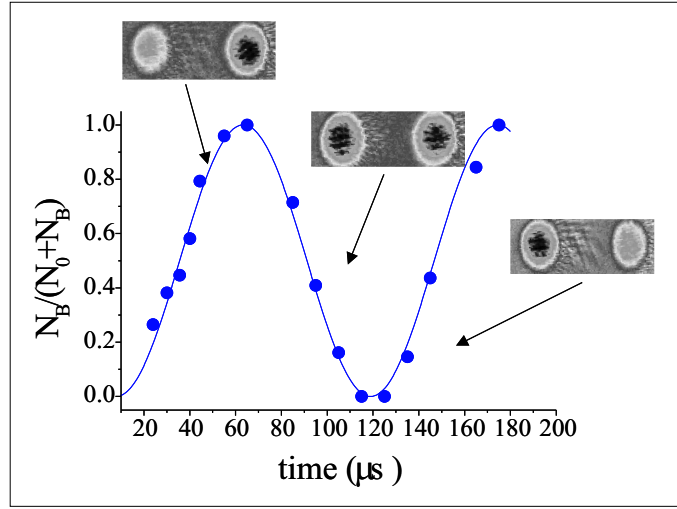


Figure A.1: Calibration procedure of the optical potential based on induced Bragg transition between a state of momentum $\hbar k_B$ and one with $-\hbar k_B$. The relative population of the diffracted peak is plotted as a function of the Bragg pulse duration. The effective Rabi frequency is extracted by fitting the experimental points.

experimentally determine the lattice height

$$\Omega_{Rabi} = \frac{|U_{dip}|}{2\hbar}. \quad (\text{A.3})$$

In unit of the recoil energy ($U_0 = sE_R$), the lattice depth s can be expressed as

$$s = \frac{2\hbar\Omega_{Rabi}}{E_R}. \quad (\text{A.4})$$

Experimentally we measure the Rabi frequency using the following procedure. After producing a condensate in the center of the magnetic trap, we suddenly displace the trap along the x -direction by a distance $\Delta x = h/(m\lambda\omega_x)$ which provide a maximum momentum to the atoms resonant with the Bragg momentum $\hbar k_B$ A.1. At this point, we switch off the magnetic confinement and we turn on the optical standing wave for a time τ . We then image the atoms after a fixed expansion time. As shown in Fig. A.1, the relative population $N_B/(N_0 + N_B)$ is then recorded as a function of the pulse duration τ , where N_B is the number of atoms which have absorbed the Bragg momentum $2\hbar k_B$. By fitting the experimental data, we extract the Rabi frequency and then the depth of the optical lattice, accordingly with Eq. (A.4).

As an example, we also report a typical image of a 2D-Bragg diffraction in Fig. A.2. Here we turn on two Bragg pulses both in the x - and z -directions.

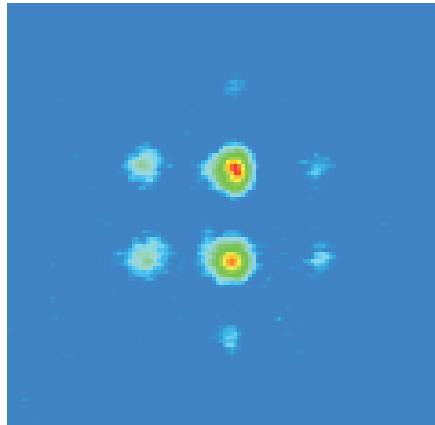


Figure A.2: Absorption image of a two-dimensional Bragg diffraction process. The Bragg pulse is sent simultaneously along the x - and z -directions.

Rigraziamenti

Eccoci arrivati finalmente ai ringraziamenti !

Ripenso ai primi giorni a Firenze, all'accoglienza al LENS, a tutti gli insegnamenti belli e meno belli avuti, ricordo il primo maldestro passo nel laboratorio ad Arcetri , ricordo i 2 traslochi, il tavolo ottico penzoloni da un camion. Ricordo tanti momenti vissuti dentro e fuori il LENS, ed ogni ricordo ha un volto, una espressione o uno sguardo. Mi giro indietro, tre anni fa, e la prima persona che sento di ringraziare è Massimo Inguscio. Un pó perché senza di lui io non sarei qui ora, un pó per la sua disponibilità ed interesse, ma soprattutto perché mi ha mostrato cosa vuole dire la dedizione al proprio lavoro. Poi ringrazio Chiara Fort (anche se mi sa che a lei i ringraziamenti non piacciono molto) e Francesco Cataliotti. Grazie perché tra un condensato ed una risata mi avete davvero fatto sentire presa per mano e guidata. Ringrazio Giovanni Modugno per molte ragioni difficili da sintetizzare in una sola frase. Grazie per la fisica che mi stai facendo conoscere e grazie perché "l'amore" che metti in laboratorio lo trasmetti un pó anche a me. Ringrazio Michele Modugno per la sua grande disponibilità e per avermi riportato ogni tanto alle mie lontane origini teoriche. Ringrazio Pasquale che quando era a Firenze mi faceva sentire un pó a Napoli, Leonardo per la sua pazienza e le sue risate contagiose, Iacopo per il suo modo tutto particolare di sdrammatizzare le cose e per le nostre chiacchierate . Grazie Estefania per le tuoi sorrisi a cuore aperto che mi tirano su nei momenti di basso numero di atomi. Ringrazio Ticijana per la sua amicizia e per avermi fatto scoprire che anche se parliamo lingue diverse (e il croato è molto diverso) è possibile capirsi subito comunque. Grazie Herwig per tutto l'aiuto che mi hai dato durante la scrittura di questa tesi e per avermi regalato espressioni italgerman davvero indimenticabili. Un ringraziamento speciale va a Giacomo. Mi hai fatto capire che la strada della conoscenza alle volte è dura e in salita ma che ne vale davvero la pena².

Un altro ringraziamento speciale va al Ribo e a Marghe che sono stati i primi a farmi conoscere e amare Firenze e a Marco de Pas per la sua disponibilità dimostrata

²Dimenticavo ... Giacomino grazie per i tuoi favolosi Muffin iperenergetici e di grande conforto.

sia con un saldatore che con una macchina fotografica in mano. Grazie Costi per come hai saputo ascoltarmi ed aiutarmi e per la tua curiosità verso la vita. E poi ci sono tutte quelle persone così speciali per me che mi hanno davvero fatto sentire a casa. Ed ecco qui Stefi, donna dai mille cappelli, che con la sua voce sa sempre tranquillizzarmi, Elenina fragile e forte allo stesso tempo e le sue dolcissime uscite degne del manuale "Dalla spontaneità alle gaffes in un sol passo". E poi ringrazio tanto Antonia, ironica e paziente, per il nostro memorabile viaggio in Andalusia, i nostri scatti e le lunghe chiacchierate in macchina. Ringrazio il Normi e le sue fantastiche pause che creano sempre una grande attesa in tutti, il Lampo ed il suo sorprendente senso per l'armonia, il Gori e la sua stupefacente conoscenza a 360° gradi e Andre che è senza dubbio la persona con meno pregiudizi che io conosca (grazie Andre!). Come dimenticare i miei amichetti di mensa e altro Iacopo, Fede e Cicchi per essermi stati così vicini in questi ultimi mesi. Ragá mi avete regalato degli sketches di una comicità e surrealità davvero unica !. Poi ringrazio "i ragazzi di Via Maggio": Daniele, Claudio, Marti, Filippo, Andrea, Monia, Piero, Sara, il Nosi e Miki. E' bello conoscervi !. Come special guests ringrazio Danilo e Patrizia che mi hanno accolto lì al Caffè Notte facendomi conoscere un pó dell'Oltrarno.

Da Firenze a Napoli, per ringraziare una persona molto importante per me: Antonio Barone. Grazie per i tuoi insegnamenti di fisica e di vita, grazie perché mi hanno fatto crescere accompagnandomi durante questi anni di dottorato. Ringrazio Pietro per tutto, per i momenti speciali passati insieme e per tutti i ricordi che ho dentro. Ti ringrazio per avermi accompagnato in questi anni. Alla fine questo dottorato mi sa che è diventato anche un pó tuo!

Dedico questa tesi alla mia Mamma. Mai come in quest'anno mi hai insegnato la forza, la voglia di vivere e la tenacia. Grazie per esserci sempre stata, grazie per tutti i tuoi consigli, per il tuo modo di partecipare accompagnandomi, grazie per la tua pazienza, grazie per avermi protetto tante volte, grazie per Nizza e per Lisbona e grazie per Libera e Bella.

Grazie Mamma !

Francesca
Tra Firenze e Napoli,
Aprile 2004

Bibliography

- [1] M. H. Anderson, J. R. Ensher, M. R. Matthews, C. E. Weiman, and E. A. Cornell, "*Observation of Bose-Einstein condensation in a dilute atomic vapor*", Science **269**, 198 (1995).
- [2] C. C. Bradley, C. A. Sackett, J. J. Tollett, and R. G. Hulet, "*Evidence of Bose-Einstein Condensation in an Atomic Gas with Attractive Interactions* ", Phys. Rev. Lett. **75**, 1687 (1995).
- [3] K. B. Davis, M. -O. Mewes, M. R. Andrews, N. J. van Druten, D. S. Durfee, D. M. Kurn, and W. Ketterle, "*Bose-Einstein Condensation in a Gas of Sodium Atoms* ", Phys. Rev. Lett. **75**, 3969 (1995).
- [4] D. G. Fried, T. C. Killian, L. Willmann, D. Landhuis, S. C. Moss, D. Kleppner, and T. J. Greytak, "*Bose-Einstein Condensation of Atomic Hydrogen* ", Phys. Rev. Lett. **81**, 3811 (1998).
- [5] S. L. Cornish, N. R. Claussen, J. L. Roberts, E. A. Cornell, and C. E. Wieman "*Stable ⁸⁵Rb Bose-Einstein Condensates with Widely Tunable Interactions*", Phys. Rev. Lett. **85**, 1795 (2000).
- [6] A. Robert, O. Sirjean, A. Browaeys, J. Poupard, S. Nowak, D. Boiron, C. I. Westbrook, and A. Aspect, "*A Bose-Einstein Condensate of Metastable Atoms*", Science **292**, 461 (2001).
- [7] F. Pereira Dos Santos, J. Léonard, J. Wang, C. J. Barrelet, F. Perales, E. Rasel, C. S. Unnikrishnan, M. Leduc, and C. Cohen-Tannoudji, "*Bose-Einstein Condensation of Metastable Helium*", Phys. Rev. Lett. **86**, 3459 (2001).
- [8] G. Modugno, G. Ferrari, G. Roati, R. J. Brecha, A. Simoni, and M. Inguscio, "*Bose-Einstein Condensation of Potassium Atoms by Sympathetic Cooling*" Science **294**, 1320 (2001).

- [9] T. Weber, J. Herbig, M. Mark, H. C. Nägerl, and R. Grimm, "*Bose-Einstein Condensation of Cesium*", *Science* **299**, 232 (2003).
- [10] Y. Takasu, K. Maki, K. Komori, T. Takano, K. Honda, M. Kumakura, T. Yabuzaki, and Y. Takahashi, "*Spin-Singlet Bose-Einstein Condensation of Two-Electron Atoms*", *Phys. Rev. Lett.* **91**, 040404 (2003).
- [11] H. C. W. Beijerinck, E. J. D. Vredenburg, R. J. W. Stas, M. R. Doery, and J. G. C. Tempelaars, "*Prospects for Bose-Einstein Condensation of Metastable Neon Atoms*", *Phys. Rev. A* **61**, 023607 (2000).
- [12] T. Ido, Y. Isoya, and H. Katori, "*Optical-Dipole Trapping of Sr Atoms at a High Phase-Space Density*", *Phys. Rev. A* **61**, 061403 (2000).
- [13] J. D. Weinstein, R. deCarvalho, C. I. Hancox, and J. M. Doyle, "*Evaporative Cooling of Atomic Chromium*", *Phys. Rev. A* **65**, 021604(2002).
- [14] F. Dalfovo, S. Giorgini, S. Stringari, and L. P. Pitaevskii, "*Theory of Bose-Einstein condensation in trapped gases*", *Rev. Mod. Phys.* **71**,463 (1999).
- [15] L. Pitaevskii and S. Stringari, "*Bose-Einstein Condensation*", Oxford Science Publications Int. Series of Monographs on Physics (2003).
- [16] D. S. Hall, "*Resource Letter BEC-1: Bose-Einstein Condensates in Trapped Dilute Gases*", cond-mat/0302518 (2003).
- [17] B. De Marco, and D. S. Jin "*Onset of Fermi degeneracy in a trapped atomic gas*", *Science* **285**, 1703 (1999).
- [18] G. Truscott, K. E. Strecker, W. I. McAlexander, G. B. Partridge, and R. G. Hulet, "*Observation of Fermi Pressure in a Gas of Trapped Atoms*", *Science* **291**, 2570 (2001).
- [19] S. Jochim, M. Bartenstein, G. Hendl, J. Hecker Denschlag, R. Grimm, A. Mosk, M. Weidemüller, "*Magnetic field control of elastic scattering in a cold gas of fermionic lithium atoms*", *Phys. Rev. Lett.* **89**, 273202 (2002).
- [20] F. Schreck, L. Khaykovich, K. L. Corwin, G. Ferrari, T. Bourdel, J. Cubizolles, and C. Salomon, "*Quasipure Bose-Einstein Condensate Immersed in a Fermi Sea*", *Phys. Rev. Lett.* **87**, 080403 (2001).
- [21] S. R. Granade, M. E. Gehm, K. M. O'Hara, and J. E. Thomas, "*All-Optical Production of a Degenerate Fermi Gas*", *Phys. Rev. Lett.* **88**, 120405 (2002).

-
- [22] Z. Hadzibabic, C. A. Stan, K. Dieckmann, S. Gupta, M. W. Zwierlein, A. Görlitz, and W. Ketterle, "*Two-Species Mixture of Quantum Degenerate Bose and Fermi Gases*", Phys. Rev. Lett. **88**, 160401 (2002).
- [23] G. Roati, F. Riboli, G. Modugno, and M. Inguscio, "*Fermi-Bose Quantum Degenerate ^{40}K - ^{87}Rb Mixture with Attractive Interaction*", Phys. Rev. Lett **89**, 150403 (2002).
- [24] P. O. Fedichev, Yu. Kagan, G. V. Shlyapnikov, and J. T. M. Walraven, "*Influence of Nearly Resonant Light on the Scattering Length in Low-Temperature Atomic Gases*", Phys. Rev. Lett. **77**, 2913 (1996).
- [25] S. Jochim, M. Bartenstein, A. Altmeyer, G. Hendl, S. Riedl, C. Chin, J. Hecker Denschlag, and R. Grimm "*Bose-Einstein condensation of molecules*", Science **302**, 2101 (2003).
- [26] M. Greiner, C. A. Regal, and D. S. Jin, "*Emergence of a Molecular Bose-Einstein Condensate from a Fermi Gas*", Nature **426**, 537 (2003).
- [27] J. Cubizolles, T. Bourdel, S. J. J. M. F. Kokkelmans, G. V. Shlyapnikov, and C. Salomon, "*Production of Long-Lived Ultracold Li_2 Molecules from a Fermi Gas*", Phys. Rev. Lett. **91**, 240401 (2003).
- [28] M. W. Zwierlein, C. A. Stan, C. H. Schunck, S. M. F. Raupach, S. Gupta, Z. Hadzibabic, and W. Ketterle, "*Observation of Bose-Einstein Condensation of Molecules*", Phys. Rev. Lett. **91**, 250401 (2003).
- [29] A. Regal, M. Greiner, D. S. Jin "*Observation of Resonance Condensation of Fermionic Atom Pairs*", Phys. Rev. Lett. **92**, 040403 (2004).
- [30] M. W. Zwierlein, C. A. Stan, C. H. Schunck, S. M. F. Raupach, A. J. Kerman, and W. Ketterle, "*Condensation of Pairs of Fermionic Atoms near a Feshbach Resonance*", Phys. Rev. Lett. **92**, 120403 (2004).
- [31] S. Jochim, M. Bartenstein, A. Altmeyer, S. Riedl, C. Chin, J. Hecker Denschlag, and R. Grimm "*Crossover from a molecular Bose-Einstein condensate to a degenerate Fermi gas*", Phys. Rev. Lett. **92**, 120401 (2004).
- [32] K. M. O'Hara, S. L. Hemmer, M. E. Gehm, S. R. Granade, and J. E. Thomas, "*Observation of a Strongly Interacting Degenerate Fermi Gas of Atoms*", Science **298**, 2179 (2002).

- [33] T. Bourdel, L. Khaykovich, J. Cubizolles, J. Zhang, F. Chevy, M. Teichmann, L. Tarruell, S.J.J.M.F. Kokkelmans, C. Salomon, "*Experimental Study of the BEC-BCS Crossover Region in Lithium 6*", cond-mat/0403091 (2004).
- [34] J. Kinast, S. L. Hemmer, M. E. Gehm, A. Turlapov, J. E. Thomas "*Evidence for Superfluidity in a Strongly Attractive Fermi Gas*", cond-mat/0403540 (2004).
- [35] M. Bartenstein, A. Altmeyer, S. Riedl, S. Jochim, C. Chin, J. Hecker Denschlag, and R. Grimm, "*Collective excitations of a degenerate gas at the BEC-BCS crossover*", cond-mat/0403716 (2004).
- [36] L. Viverit, "*Boson-induced s-wave pairing in dilute boson-fermion mixtures* ", Phys. Rev. A **66**, 023605 (2002).
- [37] A. Simoni, F. Ferlaino, G. Roati, G. Modugno, and M. Inguscio, "*Magnetic Control of the Interaction in Ultracold K-Rb Mixtures*", Phys. Rev. Lett. **90**, 163202 (2003).
- [38] W. K. Hensinger, H. Haffner, A. Browaeys, N. R. Heckenberg, K. Helmerson, C. McKenzie, G. J. Milburn, W. D. Phillips, S. L. Rolston, H. Rubinsztein-Dunlop, and B. Upcroft, "*Dynamical Tunnelling of Ultracold Atoms*", Nature **412**, 52 (2001).
- [39] F. S. Cataliotti, S. Burger, C. Fort, P. Maddaloni, F. Minardi, A. Trombettoni, A. Smerzi, and M. Inguscio, "*Josephson Junction arrays with Bose-Einstein Condensates*", Science **293**, 843 (2001).
- [40] C. Fort, F. S. Cataliotti, L. Fallani, F. Ferlaino, P. Maddaloni, and M. Inguscio, "*Collective Excitations of a Trapped Bose-Einstein Condensate in the Presence of a 1D Optical Lattice*", Phys. Rev. Lett. **90**, 140405 (2003).
- [41] F. Ferlaino, P. Maddaloni, S. Burger, F. S. Cataliotti, C. Fort, M. Modugno, and M. Inguscio, "*Dynamics of a Bose-Einstein condensate at finite temperature in an atom-optical coherence filter*", Phys. Rev. A **66**, 011604 (2002).
- [42] B. P. Anderson and M. A. Kasevich, "*Macroscopic Quantum Interference from Atomic Tunnel Arrays*", Science **282**, 1686 (1998).
- [43] O. Morsch, J. H. Müller, M. Cristiani, D. Ciampini, and E. Arimondo, "*Bloch Oscillations and Mean-Field Effects of Bose-Einstein Condensates in 1D Optical Lattices*", Phys. Rev. Lett. **87**, 140402/1–4 (2001).

-
- [44] J. H. Denschlag, J. E. Simsarian, H. Häffner, C. McKenzie, A. Browaeys, D. Cho, K. Helmerson, S. L. Rolston, and W. D. Phillips, "*A Bose-Einstein condensate in an optical lattice*", 2002 J. Phys. B At. Mol. Opt. Phys. **35**, 3095.
- [45] M. Greiner, O. Mandel, T. Esslinger, T.W. Hänsch, and I. Bloch, "*Quantum Phase Transition from a Superfluid to a Mott Insulator in a Gas of Ultracold Atoms*", Nature **415**, 39 (2002).
- [46] M. Greiner, I. Bloch, O. Mandel, T. W. Hänsch, and T. Esslinger, "*Exploring Phase Coherence in a 2D Lattice of Bose-Einstein Condensates*", Phys. Rev. Lett. **87**, 160405 (2001).
- [47] S. Burger, F. S. Cataliotti, C. Fort, P. Maddaloni, F. Minardi, M. Inguscio, "*Quasi 2D Bose-Einstein condensation in an optical lattice*", Europhys. Lett. **57**, 1 (2002).
- [48] G. Modugno, F. Ferlaino, R. Heidemann, G. Roati, and M. Inguscio, "*Production of a Fermi gas of atoms in an optical lattice*", Phys. Rev. A **68**, 011601(R) (2003).
- [49] G. Roati, E. de Mirandes, F. Ferlaino, H. Ott, G. Modugno, M. Inguscio, "*Atom interferometry with trapped Fermi gases*", cond-mat 0402328 (2004).
- [50] L. Pezzé, L. Pitaevskii, A. Smerzi, S. Stringari, G. Modugno, E. DeMirandes, F. Ferlaino, H. Ott, G. Roati, and M. Inguscio, "*Insulating Behavior of a Trapped Ideal Fermi Gas*", cond-mat/0401643 (2004).
- [51] H. Ott, E. de Mirandes, F. Ferlaino, G. Raoti, G. Modugno, and M. Inguscio, "*Collisionally Induced Transport in Periodic Potentials*", cond-mat/0311261, to be published on Phys. Rev. Lett. (2003).
- [52] H. Ott, E. de Mirandes, F. Ferlaino, G. Roati, V. Türck, G. Modugno, M. Inguscio, "*Radio Frequency Selective Addressing of Localized Particles in a Periodic Potential*" (2004).
- [53] L. Viverit, C. Menotti, T. Calarco, and A. Smerzi, "*Efficient and robust initialization of a qubit register with fermionic atoms*", cond-mat/0403178 (2004).
- [54] Alexander Albus, Fabrizio Illuminati, Jens Eisert, "*Mixtures of Bosonic and Fermionic Atoms in Optical Lattices*", Phys. Rev. A **68**, 023606 (2003).
- [55] H. P. Büchler and G. Blatter, Phys. Rev. Lett. **91**, 130404 (2003).

- [56] M. Lewenstein, L. Santos, M. A. Baranov, H. Fehrmann, Phys. Rev. Lett. **92** 050401 (2004).
- [57] M. Wouters, J. Tempere, and J.T. Devreese, "*Path integral formulation of the tunneling dynamics of a superfluid Fermi gas in an optical potential*", cond-mat/0312154 (2003).
- [58] D. A. Butts and D. S. Rokhsar, "*Trapped Fermi gases*", Phys. Rev. A **55**, 4346 (1997).
- [59] Phd Thesis of G. Roati, University of Trento (2002).
- [60] C. J. Pethick, and H. Smith, "*Bose-Einstein condensation in dilute Gases*", Cambridge University Press (2001).
- [61] B. DeMarco, J. L. Bohn, J. P. Burke, Jr., M. Holland, and D. S. Jin, "*Measurement of p-Wave Threshold Law Using Evaporatively Cooled Fermionic Atoms*", Phys. Rev. Lett. **82**, 4208 (1999).
- [62] M. R. Andrews, C. G. Townsend, H.-J. Miesner, D. S. Durfee, D. M. Kurn, and W. Ketterle, "*Observation of Interference Between Two Bose Condensates*", Science **275**, 637 (1997).
- [63] S. L. Cornish, N. R. Claussen, J. L. Roberts, E. A. Cornell, and C. E. Wieman, "*Stable ^{85}Rb Bose-Einstein Condensates with Widely Tunable Interactions*", Phys. Rev. Lett. **85**, 1795, (2000).
- [64] J. L. Roberts, N. R. Claussen, S. L. Cornish, E. A. Donley, E. A. Cornell, and C. E. Wieman, "*Controlled Collapse of a Bose-Einstein Condensate*", Phys. Rev. Lett. **86**, 4211, (2001).
- [65] E. G. M. van Kempen, S. J. J. M. F. Kokkelmans, D. J. Heinzen, and B. J. Verhaar, "*Interisotope Determination of Ultracold Rubidium Interactions from Three High-Precision Experiments*", Phys. Rev. Lett. **88**, 093201 (2002).
- [66] F. Ferlaino, R. Brecha, P. Hannaford, F. Riboli, G. Roati, G. Modugno, and M. Inguscio, "*Dipolar oscillations in a quantum degenerate Fermi-Bose atomic mixture*", J. Opt. B: Quantum Semiclass. Opt. **5**, S3 (2003).
- [67] P. Maddaloni, M. Modugno, C. Fort, F. Minardi, and M. Inguscio, "*Collective Oscillations of Two Colliding Bose-Einstein Condensates*", Phys. Rev. Lett. **85**, 2413 (2000).

-
- [68] S. D. Gensemer and D. S. Jin, "Transition from collisionless to hydrodynamic behavior in an ultracold Fermi gas" *Phys. Rev. Lett.* **87**, 173201 (2001).
- [69] G. Ferrari, M. Inguscio, W. Jastrzebski, G. Modugno, G. Roati, A. Simoni, "Collisional Properties of Ultracold K-Rb Mixtures", *Phys. Rev. Lett.* **89**, 053202 (2002).
- [70] G. Modugno, G. Roati, F. Riboli, F. Ferlaino, R. J. Brecha, M. Inguscio, "Collapse of a Degenerate Fermi Gas", *Science* **297** 2240 (2002).
- [71] K. Molmer, "Bose Condensates and Fermi Gases at Zero Temperature ", *Phys. Rev. Lett.* **80**, 1804 (1998).
- [72] R. Roth, "Structure and stability of trapped atomic boson-fermion mixtures", *Phys. Rev. A* **66**, 013614 (2002).
- [73] M. Modugno, F. Ferlaino, F. Riboli, G. Roati, G. Modugno, and M. Inguscio, "Mean-field analysis of the stability of a K-Rb Fermi-Bose mixture ", *Phys. Rev. A* **68**, 043626 (2003).
- [74] F. Riboli, and M. Modugno, "Topology of the ground state of two interacting Bose-Einstein condensates " *Phys. Rev. A* **65**, 063614 (2002).
- [75] T. Miyakawa, T. Suzuki, and H. Yabu, "Sum-rule approach to collective oscillations of a boson-fermion mixed condensate of alkali-metal atoms " *Phys. Rev. A* **62**, 063613 (2000).
- [76] H. Hu, X.-J. Liu, and M. Modugno, "Expansion of a quantum degenerate boson-fermion mixture " *Phys. Rev. A* **67**, 063614 (2003).
- [77] X.-J. Liu and H. Hu, "Sum-rule approach to collective oscillations of a boson-fermion mixed condensate of alkali-metal atoms" *Phys. Rev. A* **67**, 063613 (2003).
- [78] F. Ferlaino, E. de Mirandes, G. Roati, G. Modugno, and M. Inguscio, "Expansion of a Fermi gas interacting with a Bose-Einstein condensate ", *Phys. Rev. Lett.* **92**, 140405 (2004).
- [79] K. M. O'Hara, S. L. Hemmer, M. E. Gehm, S. R. Granade, and J. E. Thomas, "Observation of a Strongly Interacting Degenerate Fermi Gas of Atoms", *Science* **298**, 2179 (2002).

- [80] C. A. Regal, and D. S. Jin, "*Measurement of Positive and Negative Scattering Lengths in a Fermi Gas of Atoms*", Phys. Rev. Lett. **90**, 230404 (2003).
- [81] T. Bourdel, J. Cubizolles, L. Khaykovich, K. M. F. Magalhaes, S. J. J. M. F. Kokkelmans, G. V. Shlyapnikov, and C. Salomon, "*Measurement of the Interaction Energy near a Feshbach Resonance in a ^6Li Fermi Gas*", Phys. Rev. Lett. **91**, 020402 (2003).
- [82] C. Menotti, P. Pedri, and S. Stringari, "*Expansion of an Interacting Fermi Gas*", Phys. Rev. Lett. **89**, 250402 (2002).
- [83] P. Pedri, D. Guéry-Odelin, and S. Stringari, "*Dynamics of a classical gas including dissipative and mean-field effects*" Phys. Rev. A **68**, 043608 (2003).
- [84] R. Roth and H. Feldmeier, "*Mean-field instability of trapped dilute boson-fermion mixtures*", Phys. Rev. A **65**, 021603(R) (2002).
- [85] For a review see G. V. Shlyapnikov in Proceedings of XVIII International Conference on Atomic Physics ICAP2002 (Editors: H. R. Sadeghpour (ITAMP), D. E. Pritchard (CUA), and E. J. Heller (CUA)).
- [86] M. Holland, S. J. J. M. F. Kokkelmans, M. L. Chiofalo, and R. Walser, "*Resonance Superfluidity in a Quantum Degenerate Fermi Gas*" Phys. Rev. Lett. **87**, 120406 (2001).
- [87] N. W. Ashcroft and N. D. Mermin, *Solid State Physics* (Saunders College Publishing, Philadelphia, 1976).
- [88] S. R. Wilkinson, C. F. Bharucha, K. W. Madison, Q. Niu, and M. G. Raizen, "*Observation of Atomic Wannier-Stark Ladders in an Accelerating Optical Potential*" Phys. Rev. Lett. **76**, 4512 (1996).
- [89] M. Ben Dahan, E. Peik, J. Reichel, Y. Castin C. Salomon, "*Bloch Oscillations of Atoms in an Optical Potential*" Phys. Rev. Lett. **76**, 4508 (1996).
- [90] Q. Niu and, M. G. Raizen, "*Observation of the Wannier-Stark fan and the fractional ladder in an accelerating optical lattice*" Phys. Rev. A **60**, R1767 (1999).
- [91] M. C. Fischer, K. W. Madison, Q. Niu, and M. G. Raizen, Phys. Rev. A **58**, R2648 (1998).
- [92] R. Grimm, M. Weidemüller, and Yu.B. Ovchinnikov, "*Optical dipole traps for neutral atoms*", Adv. At. Mol. Opt. Phys. **42**, 95 (2000).

-
- [93] J.C. Slater, "*The Electronic Structure of Metals*", Rev. Mod. Phys. **6**, 209 (1934).
- [94] G. Wannier, "*The Structure of Electronic Excitation Levels in Insulating Crystals*", Phys. Rev. **52**, 191 (1937).
- [95] W. Kohn, "*Analytic Properties of Bloch Waves and Wannier Functions*", Phys. Rev. **115**, 809 (1959).
- [96] J.C. Slater, "*A Soluble Problem in Energy Bands*", Phys. Rev. **87**, 807 (1952).
- [97] *Tables relating to Mathieu Function*, U.S. National Bureau of Standards, Columbian University Press, New York (1951).
- [98] C. Waschke, H. G. Roskos, R. Schwedler, K. Leo, and H. Kurz, and K. Kohler, "*Coherent submillimeter-wave emission from Bloch oscillations in a semiconductor superlattice*", Phys. Rev. Lett. **70**, 3319 (1993).
- [99] M. Ben Dahan, E. Peik, J. Reichel, Y. Castin, and C. Salomon, "*Bloch Oscillations of Atoms in an Optical Potential*", Phys. Rev. Lett. **76**, 4508 (1996).
- [100] T. Pertsch, P. Dannberg, W. Elflein, A. Brauer, and F. Lederer, "*Optical Bloch Oscillations in Temperature Tuned Waveguide Arrays*", Phys. Rev. Lett. **83**, 4752 (1999); R. Morandotti, U. Peschel, J. S. Aitchison, H. S. Eisenberg, and Y. Silberberg, "*Experimental Observation of Linear and Nonlinear Optical Bloch Oscillations*", Phys. Rev. Lett. **83**, 4756 (1999).
- [101] M. Holthaus, "*Bloch oscillations and Zener breakdown in an optical lattice*", J. Opt. B: Quantum Semiclass.
- [102] G. Wannier, "*Wave Functions and Effective Hamiltonian for Bloch Electrons in an Electric Field*", Phys. Rev. **117**, 432 (1960). Opt **2**, 589 (2000).
- [103] G. Nenciu, "*Dynamics of band electrons in electric and magnetic fields: rigorous justification of the effective Hamiltonians*", Rev. Mod. Phys. **63**, 91 (1991)
- [104] J. Zak, "*Stark Ladder in Solids?*", Phys. Rev. Lett. **20**, 1477 (1968); J. Zak, Phys. Rev. Lett. **181**, 1366 (1969); J. Zak, Solid State Phys. **27**, 1 (1972).
- [105] T. Hartmann, F. Keck, H. J. Korsch, and S. Mossmann, "*Dynamics of Bloch oscillations*", New Jour. Phys. **6**, 2 (2004).
- [106] B. P. Anderson and M. A. Kasevich, in Proceedings of the International School of Physics "Enrico Fermi", M. Inguscio, S. Stringari, C. E. Wieman, eds. (IOS Press, Amsterdam, 1999).

- [107] M. Glück, A. R. Kolovsky, and H. J. Korsch, "*Wannier-Stark resonances in optical and semiconductor superlattices*", Phys. Rep. 366 (2002) 103-182.
- [108] J. E. Simsarian, J. Denschlag, M. Edwards, C. W. Clark, L. Deng, E. W. Hagley, K. Helmerson, S. L. Rolston, and W. D. Phillips, "*Imaging the Phase of an Evolving Bose-Einstein Condensate Wave Function* ", Phys. Rev. Lett. **85**, 2040 (2000).
- [109] S. Gupta, K. Dieckmann, Z. Hadzibabic, and D. E. Pritchard, "*Contrast Interferometry using Bose-Einstein Condensates to Measure h/m and α* ", Phys. Rev. Lett. **89**, 140401 (2002).
- [110] Y. Shin, M. Saba, T. A. Pasquini, W. Ketterle, D. E. Pritchard, and A. E. Leanhardt, "*Atom Interferometry with Bose-Einstein Condensates in a Double-Well Potential* ", Phys. Rev. Lett. **92**, 050405 (2004).
- [111] A. Peters, K. Y. Chung and S. Chu, "*A Measurement of Gravitational Acceleration by Dropping Atoms*", Nature **400**, 849 (1999).
- [112] F. Riehle, Th. Kisters, A. Witte, S. Helmcke, and Ch. Bordé, "*Optical Ramsey spectroscopy in a rotating frame: Sagnac effect in a matter-wave interferometer* ", Phys. Rev. Lett. **67**, 177 (1991).
- [113] J. M. McGuirk, G. T. Foster, J. B. Fixler, M. J. Snadden, and M. A. Kasevich, "*Sensitive absolute-gravity gradiometry using atom interferometry* ", Phys. Rev. A **65**, 033608 (2002).
- [114] M. Kasevich, and S. Chu, "*Atomic interferometry using stimulated Raman transitions* ", Phys. Rev. Lett. **67**, 181 (1991).
- [115] S. B. Cahn, A. Kumarakrishnan, U. Shim, and T. Sleator, "*Time-Domain de Broglie Wave Interferometry*", Phys. Rev. Lett. **79**, 784 (1997).
- [116] Ch. Bordé, "*Atomic interferometry with internal state labelling* ", Phys. Lett. A **140**, 10 (1989).
- [117] O. Carnal, and J. Mlynek, "*Young's double-slit experiment with atoms: A simple atom interferometer*", Phys. Rev. Lett. **66**, 2689 (1991).
- [118] D. W. Keith, C. R. Ekstrom, Q. A. Turchette, and D. E. Pritchard, "*An interferometer for atoms*" ,Phys. Rev. Lett. **66**, 2693 (1991)

-
- [119] Y. Torii, Y. Suzuki, M. Kozuma, T. Sugiura, T. Kuga, L. Deng and E. W. Hagley, "*Mach-Zehnder Bragg interferometer for a Bose-Einstein condensate*", Phys. Rev. A **61**, 041602 (2000).
- [120] *Atom Interferometry*, edited by P. Berman (academic Press, New York, 1997).
- [121] Th. Udem, J. Reichert, R. Holzwarth, and T. W. Hänsch, "*Absolute Optical Frequency Measurement of the Cesium D1 Line with a Mode-Locked Laser*", Phys. Rev. Lett. **82**, 3568 (1999).
- [122] B. DeMarco, J. L. Bohn, J. P. Burke, M. Holland, and D. S. Jin, "*Measurement of p-Wave Threshold Law Using Evaporatively Cooled Fermionic Atoms*", Phys. Rev. Lett. **82**, 4208 (1999).
- [123] S. Dimopoulos and A. A. Geraci, "*Probing submicron forces by interferometry of Bose-Einstein condensed atoms*", Phys. Rev. D **68**, 124021 (2003).
- [124] M. Rigol and A. Muramatsu, "*Confinement control by optical lattices*", cond-mat/0311444 (2003).
- [125] C. Hooley and J. Quintanilla, "*Single-atom density of states of an optical lattice*", cond-mat/0312079 (2003).
- [126] V. Ruuska, P. Torma, "*Quantum transport of non-interacting Fermi gas in an optical lattice combined with harmonic trapping*", cond-mat/0403429 (2004).
- [127] F. S. Cataliotti, L. Fallani, F. Ferlaino, C. Fort, P. Maddaloni, and M. Inguscio, "*Superfluid current disruption in a chain of weakly coupled Bose-Einstein condensates*", New Jour. Phys. **5**, 71 (2003).
- [128] M. Krämer, L. Pitaevskii, and S. Stringari, "*Macroscopic Dynamics of a Trapped Bose-Einstein Condensate in the Presence of 1D and 2D Optical Lattices*", Phys. Rev. Lett. **88** 180404 (2002).
- [129] M. Krämer, C. Menotti, L. Pitaevskii, and S. Stringari, "*Bose-Einstein condensates in 1D optical lattices: compressibility, Bloch bands and elementary excitations*", Eur. Phys. J. D **27**, 247 (2003).
- [130] P. Pedri, L. Pitaevskii, S. Stringari, C. Fort, S. Burger, F. S. Cataliotti, P. Maddaloni, F. Minardi, M. Inguscio, "*Expansion of a Coherent Array of Bose-Einstein Condensates*", Phys. Rev. Lett. **87**, 220401 (2001).

- [131] Thesis of L. Pezzé, University of Trento (2003).
- [132] S. Burger, F. S. Cataliotti, C. Fort, F. Minardi, M. Inguscio, M. L. Chiofalo, and M. P. Tosi, *Phys. Rev. Lett.* **86**, 4447 (2001).
- [133] S. Stringari, "*Collective Excitations of a Trapped Bose-Condensed Gas*", *Phys. Rev. Lett.* **77**, 2360 (1996).
- [134] C. Fort, M. Prevedelli, F. Minardi, F. S. Cataliotti, L. Ricci, G. M. Tino, and M. Inguscio, "*Collective excitations of a ^{87}Rb Bose condensate in the Thomas-Fermi regime*", *Europhys. Lett.* **49**, 8 (2000).
- [135] P. Massignan, and M. Modugno, "*One-dimensional model for the dynamics and expansion of elongated Bose-Einstein condensates*", *Phys. Rev. A* **67**, 023614 (2003).
- [136] A. Smerzi, A. Trombettoni, P. G. Kevrekidis, and A. R. Bishop, "*Dynamical Superfluid-Insulator Transition in a Chain of Weakly Coupled Bose-Einstein Condensates*", *Phys. Rev. Lett.* **89**, 170402 (2002).
- [137] L. Fallani, L. De Sarlo, J. E. Lye, M. Modugno, R. Saers, C. Fort, M. Inguscio, "*Observation of dynamical instability for a Bose-Einstein condensate in a moving 1D optical lattice*", *cond-mat/0404045* (2004).
- [138] L. Esaki and R. Tsu, *IBM J. Res. Develop.* **14**, 61 (1970).
- [139] L. Esaki and L. L. Chang, "*New Transport Phenomenon in a Semiconductor 'Superlattice'*", *Phys. Rev. Lett.* **33**, 495 (1974).
- [140] C. Rauch, G. Strasser, K. Unterrainer, W. Boxleitner, and E. Gornik, and A. Wacker, "*Transition Between Coherent and Incoherent Electron Transport in GaAs/GaAlAs Superlattices*", *Phys. Rev. Lett.* **81**, 3495 (1998).
- [141] S. Agan, O. A. Mironov, E. H. C. Parker, T. E. Whall, C. P. Parry, V. Yu. Kashirin, Yu. F. Komnik, V. B. Krasovitsky, and C. J. Emeleus, "*Low-temperature electron transport in Si with an MBE-grown Sb δ layer*", *Phys. Rev. B* **63**, 075402 (2001).
- [142] R. Tsu and G. Döhler, "*Hopping conduction in a 'superlattice'*", *Phys. Rev. B* **12**, 680 (1975).

- [143] S. Rott, P. Binder, N. Linder, and G. H. Döhler, "*Combined description for semiclassical and quantum transport in superlattices*", Phys. Rev. B **59**, 7334 (1999).
- [144] H. P. Büchler and G. Blatter, "*Supersolid versus Phase Separation in Atomic Bose-Fermi Mixtures* ", Phys. Rev. Lett. **91**, 130404 (2003).
- [145] M. Lewenstein, L. Santos, M. A. Baranov, H. Fehrmann, "*Atomic Bose-Fermi Mixtures in an Optical Lattice*", Phys. Rev. Lett. **92** 050401 (2004).
- [146] M. Wouters, J. Tempere, J.T. Devreese, "*Path integral formulation of the tunneling dynamics of a superfluid Fermi gas in an optical potential*", cond-mat/0312154 (2003).
- [147] M. Rodríguez and P. Törmä, "*Bloch oscillations in Fermi gases*", Phys. Rev. A **69**, 041602 (2004).